

Spring 2003

## Coherent Backscattering of Light From an Ultra Cold Gas of Rubidium-85 Atoms

Pasad B. Kulatunga  
*Old Dominion University*

Follow this and additional works at: [https://digitalcommons.odu.edu/physics\\_etds](https://digitalcommons.odu.edu/physics_etds)



Part of the [Atomic, Molecular and Optical Physics Commons](#)

---

### Recommended Citation

Kulatunga, Pasad B.. "Coherent Backscattering of Light From an Ultra Cold Gas of Rubidium-85 Atoms" (2003). Doctor of Philosophy (PhD), Dissertation, Physics, Old Dominion University, DOI: 10.25777/nvhm-m443  
[https://digitalcommons.odu.edu/physics\\_etds/55](https://digitalcommons.odu.edu/physics_etds/55)

This Dissertation is brought to you for free and open access by the Physics at ODU Digital Commons. It has been accepted for inclusion in Physics Theses & Dissertations by an authorized administrator of ODU Digital Commons. For more information, please contact [digitalcommons@odu.edu](mailto:digitalcommons@odu.edu).

# COHERENT BACKSCATTERING OF LIGHT FROM AN ULTRA COLD GAS OF $^{85}\text{Rb}$ ATOMS

by

Pasad B. Kulatunga

B.S. May 1992, University of Wisconsin

M.S. August 1994, Central Michigan University

M.S. August 1996, Old Dominion University

A Dissertation Submitted to the Faculty of  
Old Dominion University in Partial Fulfillment of the  
Requirement for the Degree of

DOCTOR OF PHILOSOPHY

PHYSICS

OLD DOMINION UNIVERSITY

May 2003

Approved by:

---

Mark D. Havey (Director)

---

Desmond Cook (Member)

---

Gilbert Hoy (Member)

---

Rocco Schiavilla (Member)

---

Andrzej Sieradzan (Member)

---

Charles Sukenik (Member)

## ABSTRACT

# COHERENT BACKSCATTERING OF LIGHT FROM AN ULTRA COLD GAS OF $^{85}\text{Rb}$ ATOMS

Pasad B. Kulatunga

Old Dominion University, 2003

Director: Dr. Mark D. Havey

This thesis reports on the experimental study of coherent radiative transport in an ultracold gas of  $^{85}\text{Rb}$  atoms confined in a magneto-optic trap. Measurements are made of the polarization dependence of the spatial and spectral profile of light backscattered from the sample. The results shows an interferometric enhancement sensitive to coherent multiple scattering in the atomic gas, and strong variations with the polarization of the incident and detected light. Effects due to coherent enhancement of weak non-resonant transitions are also observed. Comparison of the measurements with realistic quantum Monte Carlo simulations of Kupriyanov, et al [1] yield very good agreement.

## ACKNOWLEDGMENTS

I like to express my deepest gratitude to Dr. Mark Havey for giving me the opportunity to work with him. I also thank him for sharing his expertise, deep insight and guidance during and through every step of this research. I thank him for his friendship and advice. I like to express my sincere thanks to Dr. Charles Sukenik for always being there, to answer questions, to help and to encourage. Without Dr. Sukenik's knowledge and experience in atom cooling and trapping, this work would not have been possible. I like to thank the dissertation committee members, Dr. Desmond Cook, Dr. Gilbert Hoy, Dr. Rocco Schiavilla, and Dr. Andrzej Sieradzan for their reading of this dissertation and their helpful remarks. I would also like to thank Mr. Tobias Oed for the many helpful discussions, and his effort and time in data analysis. I also would like to thank Mr. Salim Balik for his help in data acquisition. I commend him for his efforts at continuing this work. I will always be grateful to my wife Sara for her support and her patience during the course of this work, without which this would have not been possible.

# TABLE OF CONTENTS

	Page
List of Tables . . . . .	vi
List of Figures . . . . .	ix
CHAPTERS	
1 Introduction . . . . .	1
1.1 History . . . . .	1
1.2 Speckle and Coherent Backscattering (CBS) . . . . .	2
1.3 Localization of Light . . . . .	2
1.4 Ultracold Atoms . . . . .	3
1.5 Outline of this thesis . . . . .	4
2 Theory . . . . .	5
2.1 Interference in Backscattering Direction . . . . .	6
2.1.1 Pairwise Averaging . . . . .	8
2.1.2 Profile of the Backscattering Cone . . . . .	12
2.2 Wave Scattering in Dilute Atomic Gases . . . . .	14
2.2.1 Single Scattering from a Two Level Atom . . . . .	16
2.2.2 Single scattering intensity and its angular dependence on polarization . . . . .	20
2.3 Multiple scattering and Polarization . . . . .	22
3 Experiment . . . . .	31
3.1 Experiment Overview . . . . .	31
3.2 Description of the Experimental Setup . . . . .	34
3.2.1 Probe Laser . . . . .	34
3.2.2 Polarization . . . . .	38
3.2.3 Signal Detection . . . . .	39
3.2.4 Background Noise . . . . .	43
3.2.5 Instrument Resolution . . . . .	46
3.3 Samples . . . . .	47
3.3.1 Suspensions and Solids . . . . .	47
3.3.2 Ultracold $^{85}\text{Rb}$ . . . . .	52
4 Results and Analysis . . . . .	59
4.1 Coherent Backscattering Enhancement . . . . .	59
4.2 Spectral dependence of the enhancement . . . . .	72
5 Conclusions . . . . .	80
APPENDIX A The angular integration of the array . . . . .	83
A.1 integration.c . . . . .	83
A.2 array.c . . . . .	85

A.3 readfile.c . . . . .	90
BIBLIOGRAPHY . . . . .	93
VITA . . . . .	97

## LIST OF TABLES

		Page
I	The detection polarization channels defined relative to the incident polarization. . . . .	34
II	The analyzing power of the polarimeter is defined by the extinction ratio, $I_{\uparrow}/I_{\rightarrow}$ , measured by retro-reflecting the probe from a mirror at sample position . . . . .	38
III	The intensity of speckle formed by light scattered from optical elements in the four polarization channels, shown with the relative orientations of the analyzer with respect to the incident polarization direction. . . . .	45
IV	The full width at half maximum (FWHM) and the enhancement values measured for some solids and suspensions. . . . .	53
V	The measured full width at half maximum and the enhancement on resonance in the four polarization channels . . . . .	61

## LIST OF FIGURES

	Page
1 Scattering paths of two interfering rays $A_{out}$ and $B_{out}$ . Path B(A) is the exact reverse path of A(B) and both rays have the same incident and exit wave vectors $k_{in}$ and $k_{out}$ . Ray $A_{in}$ follows the path $r = r_1, r_2 \dots r_n = r'$ and $B_{out}$ follows the exact reverse path of, $r' = r_n, r_2 \dots r_1 = r$ . The angle between the incident and exit wave vectors is $\theta$ . The interface is at an angle $\alpha$ to the vertical. . . . .	7
2 Horizontal cross section through an intensity profile observed from 780 nm, collimated laser beam incident on a sample of fine grain sand. (a) the rapidly varying speckle pattern (b) the same cross section but with configuration averaging . . . . .	10
3 The excitation frame with the quantization axis defined by z and the detection frame with the $z'$ axis along the direction of detection. . . .	21
4 Angular distribution of linearly polarized light due to single scattering.	23
5 Angular distribution of circularly polarized light, intensity in the backwards direction is minimum in the helicity preserving channel. . . . .	24
6 A degenerate atomic dipole transition which allows Rayleigh and elastic (degenerate) Raman transitions. The Rayleigh and elastic Raman transitions are indicated by the solid lines; the dashed line indicates a Raman transition. . . . .	26
7 Violation of maximal contrast criterion due to the atom's internal structure. The two atoms are located in the plane of the paper and the light is incident into the paper. The atoms are in two different Zeeman sublevels. The incident polarization is $\sigma^+$ . In the $h  h$ channel, the $\sigma^-$ polarization will be detected. The direct scattering path, and the reverse path are shown in the left and the right sequence respectively [24]. . . . .	27
8 Diagrams showing direct and reciprocal paths for (a) Rayleigh-type, and for (b) Raman-type coherent backscattering for two atoms located along the propagation direction of the incident light [1]. . . . .	29
9 Diagrams showing the transitions open for Rayleigh-type and Raman-type, (a) and (b) respectively for coherent backscattering in the geometry of Figure 8. The solid circles show the state-designation of atoms and the solid and dashed-dotted arrows indicate the transitions open for direct and for reciprocal scattering paths respectively [1]. . . . .	30
10 The level diagram of the $^{85}\text{Rb}$ hyperfine manifold. . . . .	32
11 Schematic of the experimental setup . . . . .	33
12 Schematic of the external cavity diode laser . . . . .	35
13 The oscilloscope scan of the saturated absorption spectrum of the hyperfine components of the $5s^2S_{1/2} \rightarrow 5p^2P_{3/2}$ transition of $^{85}\text{Rb}$ , used to lock the trapping laser and for offsetting the probe . . . . .	36



14	Block diagram showing the laser stabilization scheme used to lock the probe and trapping lasers . . . . .	37
15	Block diagram showing the synchronization of the detection phase with the on, off cycle of the trapping, hyperfine re-pumper (HFRP) lasers, and the coherent backscattering probe laser. When the chopper blade is closed the trap laser is ON, probe OFF, and when the blades are open the trap laser is turned OFF, the coherent backscattering laser is turned ON in the middle of the exposure. . . . .	41
16	The timing diagram showing the trap, probe and exposure (CCD open/closed). The trigger signal is derived from the phased locked synchronization signal generated by the chopper. . . . .	42
17	The attenuation of the probe beam as a function of detuning. The filled circles shows attenuation of linearly polarized light and the open circles the circularly polarized light. The measurement is taken sufficiently far from the trap to avoid collecting trap fluorescence. . . . .	44
18	The horizontal cross section through the center of the coherent backscattering signal signal from a sample of rutile $\text{TiO}_2$ consisting of particles on the average of $\sim 1.2\text{-}1.5\ \mu\text{m}$ suspended in water. (a) Volume fraction-High. (b)Volume fraction-Low. . . . .	48
19	Plot of full width half maximum (FWHM) of coherent backscattering signal cone profile of rutile $\text{TiO}_2$ suspended in water as a function of volume fraction. For clarity the curve is expanded to show the behavior at low concentrations in the inset. . . . .	49
20	coherent backscattering signal image of $1.0\ \mu\text{m}$ diameter polymer spheres suspended in water and the horizontal line scan through the intensity maxima, corresponding to $\theta = 0$ . The full width half maximum of this cone is approximately $0.5\ \text{mrad}$ . . . . .	51
21	The horizontal cross section through the center of the coherent backscattering profile of $\sim 2\ \text{mm}$ diameter styrofoam ball. The cone width is $1.3 \pm 0.2\ \text{mrad}$ . The speckle was averaged by slowly rotating the sample in the probe beam. . . . .	52
22	Schematic of the magneto-optical-trap. Six laser beams intersect at the center of the chamber where the sum of the magnetic fields produced by the two electromagnetic coils is zero. . . . .	54
23	Schematic of the master-slave configuration used for the trap laser . . . . .	55
24	Absorption profile with the probe scanned over the hyperfine manifold . . . . .	57
25	The charge couple device (CCD) camera images of the coherent backscattering cone in all four channels. Images are color enhanced for clarity . . . . .	60
26	The coherent backscattering profile at resonance in the $l  l$ , and $l\perp l$ channels, the solid line is a Lorentzian fit to the data. . . . .	62
27	The coherent backscattering profile at resonance in the $h  h$ , and $h\perp h$ channels, the solid line is a Lorentzian fit. . . . .	63

28	The on resonance, angular integrated coherent back scattering profile of the $h  h$ channel, and the $l  l$ channel. . . . .	64
29	The experimental coherent backscattering profiles in the helicity channels shown with the quantum Monte-Carlo simulation results. Graph (a) is the horizontal scan of the $h  h$ profile, and graph (b) is the horizontal scan of the $h\perp h$ profile [1]. . . . .	65
30	The experimental coherent backscattering profiles in the linear channels shown with the quantum Monte-Carlo simulation results. Graph (a) is the horizontal scan of the $l  l$ profile, and graph (b) is the horizontal scan of the $l\perp l$ profile [1]. . . . .	66
31	Dependence of the coherent backscattering enhancement on the scattering order calculated for the $F = 3 \rightarrow F' = 4$ hyperfine transition in $^{85}\text{Rb}$ for a Gaussian type atomic cloud of $r_0 = 1 \text{ mm}$ for tow densities, (a) $n_0 = 8 \cdot 10^9 \text{ cm}^{-3}$ , and (b) $n_0 = 16 \cdot 10^9 \text{ cm}^{-3}$ . Individual curves represent different polarizations channels [1]. . . . .	68
32	Dependence of the coherent backscattering enhancement on the sample size - theoretical prediction [1] . . . . .	69
33	Dependence of the full width half maximum of the cone profile on the sample size. The optical depth for these calculations were fixed at 5 [1].	70
34	The experimental coherent backscattering profiles in the linear channels shown with the quantum Monte-Carlo simulation results. Graph (a) is the vertical scan of the $l  l$ profile, graph (b) is the horizontal scan of the same linear profile, and (c) is the horizontal scan of the $l\perp l$ profile, and (d) is the vertical scan of the same. The solid line is the theoretically predicted value, the open circles represent the experimental values [1]. . . . .	71
35	Detuning dependence of the total backscattered intensity, theory and experiment. Theoretical curves are for two different optical depths, $b \approx 5$ and $b \approx 10$ [1]. . . . .	74
36	The spectral dependence of the coherent backscattering profile relative to incident light detuning in (a) the helicity preserving, $h  h$ channel and (b) the helicity non-preserving, $h\perp h$ channel. . . . .	75
37	The spectral dependence of the coherent backscattering profile relative to incident light detuning in (a)the linear parallel, $l  l$ and in (b) the linear perpendicular, $l\perp l$ channels. . . . .	76
38	The calculated spectral dependence of the enhancement factor in the circular channels for the $F = 3 \rightarrow F' = 4$ hyperfine transition, in $^{85}\text{Rb}$ . Gaussian type atomic cloud, (a) radius $r_0 = 1 \text{ mm}$ , density $n_0 = 8 \cdot 10^9 \text{ cm}^{-3}$ and (b) radius $r_0 = 1 \text{ mm}$ , density $n_0 = 16 \cdot 10^9 \text{ cm}^{-3}$ [1]. . . . .	78
39	The calculated spectral dependence of the enhancement factor in the linear channels for the $F = 3 \rightarrow F' = 4$ hyperfine transition, in $^{85}\text{Rb}$ . Gaussian type atomic cloud, (a) radius $r_0 = 1 \text{ mm}$ , density $n_0 = 8 \cdot 10^9 \text{ cm}^{-3}$ and (b) radius $r_0 = 1 \text{ mm}$ , density $n_0 = 16 \cdot 10^9 \text{ cm}^{-3}$ [1].	79

# CHAPTER 1

## INTRODUCTION

### 1.1 HISTORY

This thesis deals with the transport of radiation in a strongly scattering resonant medium. It is specifically concerned with those effects that are intrinsic to coherent transport of waves in such media, as opposed to the intensity transport customarily dealt with in classical study of radiation trapping . Radiation trapping in dilute vapors has been studied extensively, but most studies of radiation trapping do not take into consideration effects due to coherent multiple scattering of this radiation. Wave propagation in non-resonant, dielectric objects through multiple elastic scattering shows strong effects due to coherence in the multiply scattered wave fronts. Such effects are often not considered in the classical treatment of wave propagation in dilute gases. In the classical approach to scattering from a dense distribution of elastic scatterers, it is generally assumed that the phases of the scattered wave fronts are uncorrelated. This assumption leads to an intensity transport equation of the Boltzman type in length scales larger than an elastic mean free path. In length scales much larger than the elastic mean free path  $l$ , and in correspondingly large time scales  $\tau = l/c$ , this equation reduces to a diffusion equation with a diffusion constant  $D = lc/3$  [2]. However it was soon discovered that the diffusive nature of the wave intensity transport after multiple scattering is grossly insufficient to completely describe certain observed characteristics of scattering in random media. This was realized by the condensed matter community in working with electron scattering in impure metals and in optics with respect to electromagnetic wave propagation in a turbulent atmosphere [3, 4]. Recent independent observations of coherent backscattering (CBS) of light from dielectric microspheres,  $TiO_2$ , GaAs powder, and specially designed photonic crystals, for example has clearly demonstrated that interference plays a vital role in radiation transport in matter and needs to be accounted for to properly explain these observations [5, 6, 7].

---

This dissertation follows the style of *The Physical Review*

## 1.2 SPECKLE AND COHERENT BACKSCATTERING (CBS)

With the advent of the laser, manifestations of coherent optical effects were easily observed. When a strongly scattering medium is illuminated by a coherent laser and the total transmitted or the reflected light intensity is measured, the measured value and its dependence on sample properties should be well described by solutions to the diffusion equation with appropriate boundary conditions. What is observed instead is a seemingly random distribution of intensity with interlaced dark and bright spots, and not the smooth variation predicted by the diffusion approach to intensity transport of the incident radiation. These intensity variations are called speckle and arise from interference between phase correlated wave fronts in the absence of inelastic scattering. It should be noted that the diffusive character and the interference effect are not mutually exclusive in the absence of inelastic scattering. The effect of the speckle pattern at a point of observation is reflected in configuration averaging as an increase in the intensity fluctuation as compared to classical diffusion [8, 9]. A related phenomenon is the enhanced backscattering of light from random scatterers, an effect that arises from constructive interference of backscattered light with corresponding time reversed paths through the scattering medium. The intensity in the exact backscattering direction can be as much as a factor of two greater than the incoherent background predicted by the intensity diffusion equation. This coherent backscattering (CBS) effect is also known and referred to as the weak localization effect of light [10]. Although no real localization of radiation is taking place, enhanced backscattered intensity is indicative of coherent transport of radiation in the scattering medium. A similar effect in electrons had been widely studied in the condensed matter community well before the discovery of coherent backscattering of light.

## 1.3 LOCALIZATION OF LIGHT

Electrical conductivity in a crystalline solid is a manifestation of interference between various scattering trajectories of electrons in the solid. It is the wave nature of the electrons that gives rise to allowed energy bands and forbidden gaps in its motion in a crystalline solid. It was discovered by Phillip W. Anderson in 1958 that by introducing a certain critical degree of disorder in the crystal and for some energies, the electronic wave functions could be localized. This important phenomena is referred to as Anderson Localization [11]. It is firmly established that interference of the

electronic waves is critical to this process. A related effect due to wave interference is Universal Conductance Fluctuations (UCF), a precursor to Anderson Localization in disordered conductors cooled to low temperatures [12]. The fluctuations of the conductance are independent of sample, parameters such as the mean free path of the electrons, size of the sample and the conductance itself and hence the term Universal Conductance Fluctuations. This precursor effect to strong localization is called weak localization of electrons. This too is an interference effect in multiple scattering but not as pronounced as Anderson Localization. The direct optical analog of this effect is coherent backscattering, or enhanced backscattering of photons from disordered random scatterers. The discovery of coherent backscattering by Ad Lagendijk [6] and independently by George Maret [7, 10] in 1985 clearly indicated the close analogy between electron interference and photon interference in random medium. These discoveries, and theoretical work on strong localization of light in random media have led many researchers to search for Anderson Localization of photons [11, 13, 14]. There have been recent reports of photon localization in random media [16, 15]. Though Anderson Localization of photons in atomic gas has remained elusive to date, these studies have led to significant discoveries in light propagation in disordered materials and interference. It must be noted that the analogy between electron localization and photon localization spoken here is strictly with respect to the diffusion point of view, or wave transport in scattering medium. One should keep in mind that there are fundamental differences between electrons in impure conductors and photons in dielectrics.

#### 1.4 ULTRACOLD ATOMS

Most of the investigations in localization of light have been restricted to photons in macroscopic samples such as suspensions of colloids, semiconductor powders, polymer spheres (dielectric spheres) confined in a slab or cylindrical geometry. However the developments in recent years of laser cooling and trapping techniques applied to atomic gases have made accessible an entirely new system for the study of CBS- a high density mono-disperse sample of resonant point-dipole scatterers with large and widely alterable scattering cross section [17, 18, 19, 20, 21]. It has been recently suggested that such collection of scatterers may indeed hold the promise of achieving strong localization [22]. Coherent backscattering from an ultra cold sample of  $^{85}\text{Rb}$  in a magneto-optical trap (MOT) was first observed in 1999 by G. Labeyrie et al [23, 24],

and subsequently by our group in 2001 under different experimental conditions [25]. Subsequent studies have explored the finer details of coherent backscattering from ultracold atoms including the effects of an external static magnetic field, and the effect on the spatial profile of the CBS signal due to the trap geometry [1, 26]. In this thesis prior results are confirmed and new results obtained by exploring the effects of the laser field, such as detuning, laser polarization, and the internal quantum mechanical structure of the scatterers on coherent backscattering.

## 1.5 OUTLINE OF THIS THESIS

In Chapter 2 an introduction to the diffusion model of wave transport in a scattering medium is given. Distinction between the classical treatment of radiation trapping and coherent radiation transport will be discussed. The shape of the backscattered intensity profile and the maximum possible enhancement will be derived with appropriate boundary conditions in the diffusion model. Characteristics of the spatial profile of the backscattered intensity and its dependence on scattering order, and the scattering length will be considered. The conceptual ideas associated with polarization effects, and backscattered intensity dependence on quantum reciprocity loss will also be discussed. The basic ideas pertaining to light scattering from atoms with internal quantum structure, as opposed to scattering from point-like dipole scatters, will be analyzed. In Chapter 3 various aspects of the experiment such as the precision polarimeter, the optical detection system, the magneto-optical trap, and the experimental procedure are described in detail. The results and the analysis of the data will be presented in Chapter 4. Final discussion and conclusions are given in Chapter 5.

## CHAPTER 2

### THEORY

The propagation of light in a strongly scattering, non-absorbing media is a difficult problem to treat even in the simplest scalar form. In the limit that the scattering is weak, the propagation of photons can be viewed as a random walk in the medium with a mean free path  $l^*$  [8]. The mean free path,  $l^*$  depends on the density of the scatterers and the scattering cross section and typically is many times the wavelength. The transport velocity is dependent on the index of refraction and is typically close or equal to the speed of propagation of light in the medium when the scattering is non resonant [27]. This leads to an intensity transport equation of the Boltzman type which reduces to a diffusion equation with the diffusion constant  $D$  at length scales larger than  $l^*$ , the length scale over which the direction of incident light is well randomized through scattering. The diffusion constant  $D$  is given by  $D = l^*v/3$  where  $v$  is the transport velocity. The intensity scattered from a bounded, weakly scattering medium can be well described by the intensity diffusion model but it fails to account for either the intensity fluctuations due to speckle, or the observed enhancement of intensity in the backscattering direction [2]. Enhanced backscattering is due to interference of phase correlated multiply scattered partial waves that the diffusion model above discounts.

Consider a wave characterized by the wave vector  $\mathbf{k}$  incident on a disordered scattering medium. It will be scattered by the constituent scatterers into many different partial waves. All these partial waves are able to interfere with each other if the scattering is completely elastic. In the limit in which  $kl^* \gg 1$ , the average distance between scatterers is much larger than the wavelength and the waves are able to propagate freely. The mean free path  $l^*$  is determined by the number density  $n$  and the scattering cross section  $\sigma$  of the scatterers as  $l^* = 1/n\sigma$ . The multiply scattered wave amplitude at a space-time point  $(\vec{r}, t)$  can be constructed by a coherent superposition  $E = \sum_p A_p$  of the partial wave amplitudes  $A_p$ , where  $p$  represents a path connecting the scattering center [28]. Therefore, a particular configuration of the scatterers will determine the intensity at a point of observation outside the sample boundary, either in transmission or reflection. In fact it is the interference between these scattered partial wave fronts that gives rise to the speckle patterns observed in laser transmission through, and reflection from, disordered media. It

is valid to assume that such an interference pattern will average to some smooth background if an average over different configurations of the scatterers is carried out. Experimentally the speckle can be easily averaged out to such a configuration mean. However in a small angular region centered in the backscattering direction a distinct intensity peak above the background survives. This is due to interference between correlated fields as a result of multiple scattering. By contrast the well studied Bragg scattering arises due to the spatial correlation of the scatterers itself as opposed to correlations of the field due to multiple scattering.

In the following section a simplified model explaining the coherent backscattering is given. More rigorous scalar wave models can be found in [2],[29], [30], and [31].

## 2.1 INTERFERENCE IN BACKSCATTERING DIRECTION

The enhancement observed in the backscattering direction is due to constructive interference between rays that have propagated in exact, but momentum-reversed or time-reversed paths. Paths A and B shown in Figure 1 are two such partial waves where  $B_0$  is the conjugate of the partial wave  $A_0$ .

The degree of interference of these momentum reversed paths will depend on the relative phase or the path length difference between the two scattered wave fronts. This phase difference is given by

$$\Delta\phi = \frac{2\pi}{\lambda}(d_2 - d_1) \quad (1)$$

where  $\lambda$  is the wavelength and  $d_2 - d_1$  is the path length difference. The distance  $d_1$  is the projection of the vector  $\mathbf{r}_n - \mathbf{r}_1$  on to  $-\hat{\mathbf{k}}_i$ , the unit vector in the direction of the incident wave vector. Likewise the distance  $d_2$  is the projection of vector  $\mathbf{r}_n - \mathbf{r}_1$  on to  $\hat{\mathbf{k}}_{out}$ . Therefore the path lengths  $d_1$  and  $d_2$  can be written as,

$$\begin{aligned} d_1 &= -\hat{\mathbf{k}}_{in} \cdot (\mathbf{r}_n - \mathbf{r}_1) \\ d_2 &= \hat{\mathbf{k}}_{out} \cdot (\mathbf{r}_n - \mathbf{r}_1) \end{aligned} \quad (2)$$

allowing the phase difference to be written as,

$$\Delta\phi = \frac{2\pi}{\lambda}(\hat{\mathbf{k}}_{out} + \hat{\mathbf{k}}_{in}) \cdot (\mathbf{r}_n - \mathbf{r}_1). \quad (3)$$

This clearly shows that for a scattering path and for its exact time reversed path, i.e. for  $\hat{\mathbf{k}}_{in} + \hat{\mathbf{k}}_{out} = \mathbf{0}$  the phase difference is zero. These two paths will completely,



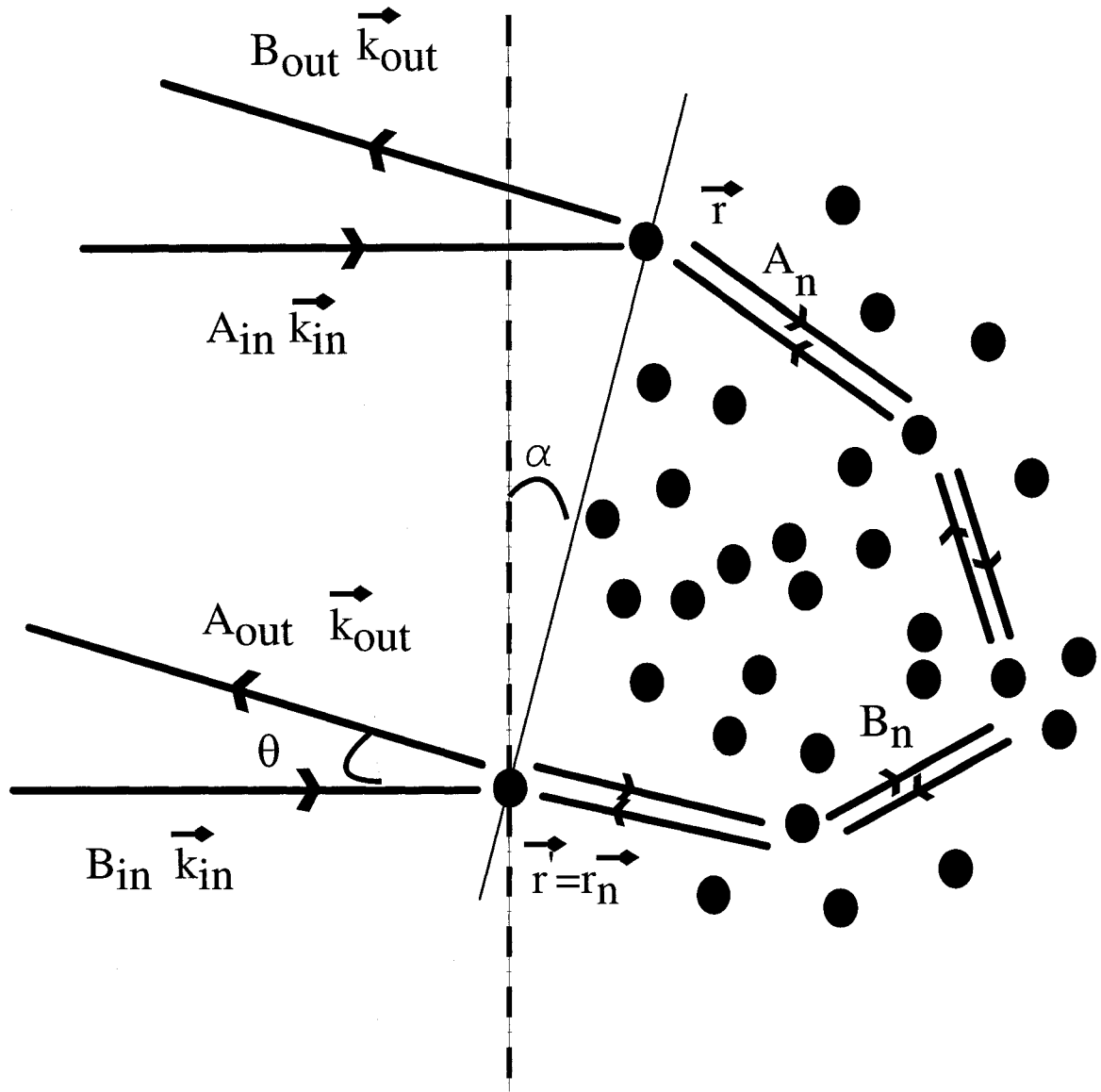


FIG. 1. Scattering paths of two interfering rays  $A_{out}$  and  $B_{out}$ . Path B(A) is the exact reverse path of A(B) and both rays have the same incident and exit wave vectors  $k_{in}$  and  $k_{out}$ . Ray  $A_{in}$  follows the path  $r = r_1, r_2 \dots r_n = r'$  and  $B_{out}$  follows the exact reverse path of,  $r' = r_n, r_2 \dots r_1 = r$ . The angle between the incident and exit wave vectors is  $\theta$ . The interface is at an angle  $\alpha$  to the vertical.

and constructively interfere. This somewhat heuristic argument shows the origin of the interference in the backscattering geometry in multiple scattering. The intensity diffusion model can be modified to incorporate the interference effect by assuming amplitude transport as opposed to intensity transport.

### 2.1.1 Pairwise Averaging

Shown in Figure 1 is a single scattering path, one out of many such paths. The path shown in Figure 1 corresponds to the position vectors  $\mathbf{r}_1 = \mathbf{r}$ ,  $\mathbf{r}_n = \mathbf{r}'$ , and the two wave vectors  $\mathbf{k}_{in}$ ,  $\mathbf{k}_{out}$ . The outgoing complex amplitude is  $E_A$  and  $E_B$  are given by the sum of all the many different scattering paths. The complex amplitude  $E_{A0}$  at some observation point  $r_0$  due to the single scattering path  $A$  (see Figure 1) is related to the incident wave  $A_{in}$  as [8],

$$E_{A0} = A_{in} G_A \exp[i\mathbf{k}_{in} \cdot (\mathbf{r}_1 - \mathbf{R}_0) + i\mathbf{k}_{1,2} \cdot (\mathbf{r}_2 - \mathbf{r}_1) + \dots + i\mathbf{k}_{n-1,n} \cdot (\mathbf{r}_n - \mathbf{r}_{n-1}) + i\mathbf{k}_{out} \cdot (\mathbf{r}_0 - \mathbf{r}_n)]. \quad (4)$$

Here  $k_{n-1,n}$  is the wave vector of ray propagation between scatterers  $n-1$  and  $n$ , and  $G_A$  is the amplitude propagator between the two scatterers, assumed to be the same for identical scatterers. Similarly  $E_{B0}$  can be related to  $B_{in}$  by reversing the wave vector with the wave vector to account for counter propagation along the path  $B$ . The electric field  $E_{B0}$  is,

$$E_{B0} = B_{in} G_B \exp[i\mathbf{k}_{in} \cdot (\mathbf{r}_n - \mathbf{R}_0) + i\mathbf{k}_{n,n-1} \cdot (\mathbf{r}_{n-1} - \mathbf{r}_n) + \dots + i\mathbf{k}_{2,1} \cdot (\mathbf{r}_1 - \mathbf{r}_2) + i\mathbf{k}_{out} \cdot (\mathbf{r}_0 - \mathbf{r}_n)]. \quad (5)$$

For identical scatterers  $G_A = G_B$ . And by definition  $A_{in} = B_{in}$ . The intermediate wave vectors,  $k_{n-1,n} = -k_{n,n-1}$ . Therefore in equations (4) and (5) the sum of the phases are the same except the phase difference due to extra path length for  $B_{out}$  at incidence and for  $A_{out}$  at exit. In the exact backscattering direction this path length difference is identically zero and there is no net phase difference. It can be shown by evaluating the ratio  $E_{A0}/E_{B0}$  that this phase difference is identical to that obtained in (3). The field detected at the observation point at  $r_0$  is the coherent sum of the scattered electric field amplitudes, where  $A_{out}$  and  $B_{out}$  are just two. Therefore the intensity at  $r_0$  due to the rays  $A$  and  $B$  is given by,

$$|E_{A0} + E_{B0}|^2 = |E_{A0}|^2 + |E_{B0}|^2 + E_{A0}E_{B0}^* + E_{B0}E_{A0}^*$$

$$\begin{aligned}
&= |E_{A0}|^2 + |1 + \exp[-i(\mathbf{k}_{\text{in}} + \mathbf{k}_{\text{out}}) \cdot (\mathbf{r} - \mathbf{r}')]|^2 \\
&= 2 \{1 + \cos[(\mathbf{k}_{\text{in}} + \mathbf{k}_{\text{out}}) \cdot (\mathbf{r} - \mathbf{r}')]\}.
\end{aligned} \tag{6}$$

There are two different types of terms in (6), those arising from incoherent scattering,  $|E_{A0}|^2 + |E_{B0}|^2$  and that of those due to coherent scattering and contributing to the interference term,  $E_{A0}E_{B0}^* + E_{B0}E_{A0}^*$  [8]. In the exact backscattering direction where  $\mathbf{k}_{\text{in}} = -\mathbf{k}_{\text{out}}$ , the enhancement is exactly a factor of two.

If the respective positions of the scatterers are fixed, the field amplitude observed at  $r_0$ , corresponding to some  $\theta$  will be the coherent sum of many partially scattered waves. Therefore the intensity will be a rapidly varying function of  $\theta$  and this is the familiar speckle pattern that one observes from a sample with a fixed random distribution of scatterers. An intensity cross section of a speckle pattern is shown in Figure 2a. The squared sum in equation (6) is the intensity due to a subset of partially scattered waves, namely from the points  $\mathbf{r}$  and  $\mathbf{r}'$ ; and a subset that allows the field amplitude to be correlated in the exact backscattering direction. This correlation is not due to a correlation of the position of the scatterers, which is the origin of Bragg scattering in crystals, but is due to the existence of exact reverse paths as shown before.

It is possible to expand the sum in equation (6) to incorporate scattering from three points,  $\mathbf{r}$ ,  $\mathbf{r}'$ , and  $\mathbf{r}''$ , such that the intensity is now given by [8, 24],

$$\begin{aligned}
|E_A + E_B + E_C + E_D + E_E + E_F|^2 &= |E_A + E_B|^2 + |E_C + E_D|^2 + |E_E + E_F|^2 \\
&\quad + (E_A + E_B)(E_C + E_D)^* + (E_A + E_B)^*(E_C + E_D) \\
&\quad + (E_A + E_B)^*(E_E + E_F) + (E_A + E_B)(E_E + E_F)^* \\
&\quad + (E_C + E_D)^*(E_E + E_F) + (E_C + E_D)(E_E + E_F)^*, \tag{7}
\end{aligned}$$

where the 3 paired fields  $(E_A, E_B)$ ,  $(E_C, E_D)$ , and  $(E_E, E_F)$  correspond to scattering from  $(r \rightarrow r'$  and  $r' \rightarrow r)$ ,  $(r \rightarrow r''$  and  $r'' \rightarrow r)$ , etc. The terms consist of squares of paired amplitudes each resulting in an expressions similar to (6). Also there are terms that are specific to the configuration, these are the interference terms between paired amplitudes such as  $(E_A + E_B)$ . It is these terms that give rise to speckle and are specific to the particular configuration. The phase between any two paired amplitudes will vary rapidly from one configuration to the other as there is no *a priori* reason that the scattering paths of the pairs be correlated. In averaging over configurations, the speckle reduces to some mean intensity because a maximum intensity at some  $\theta'$  due to a particular configuration is more likely to be smaller for

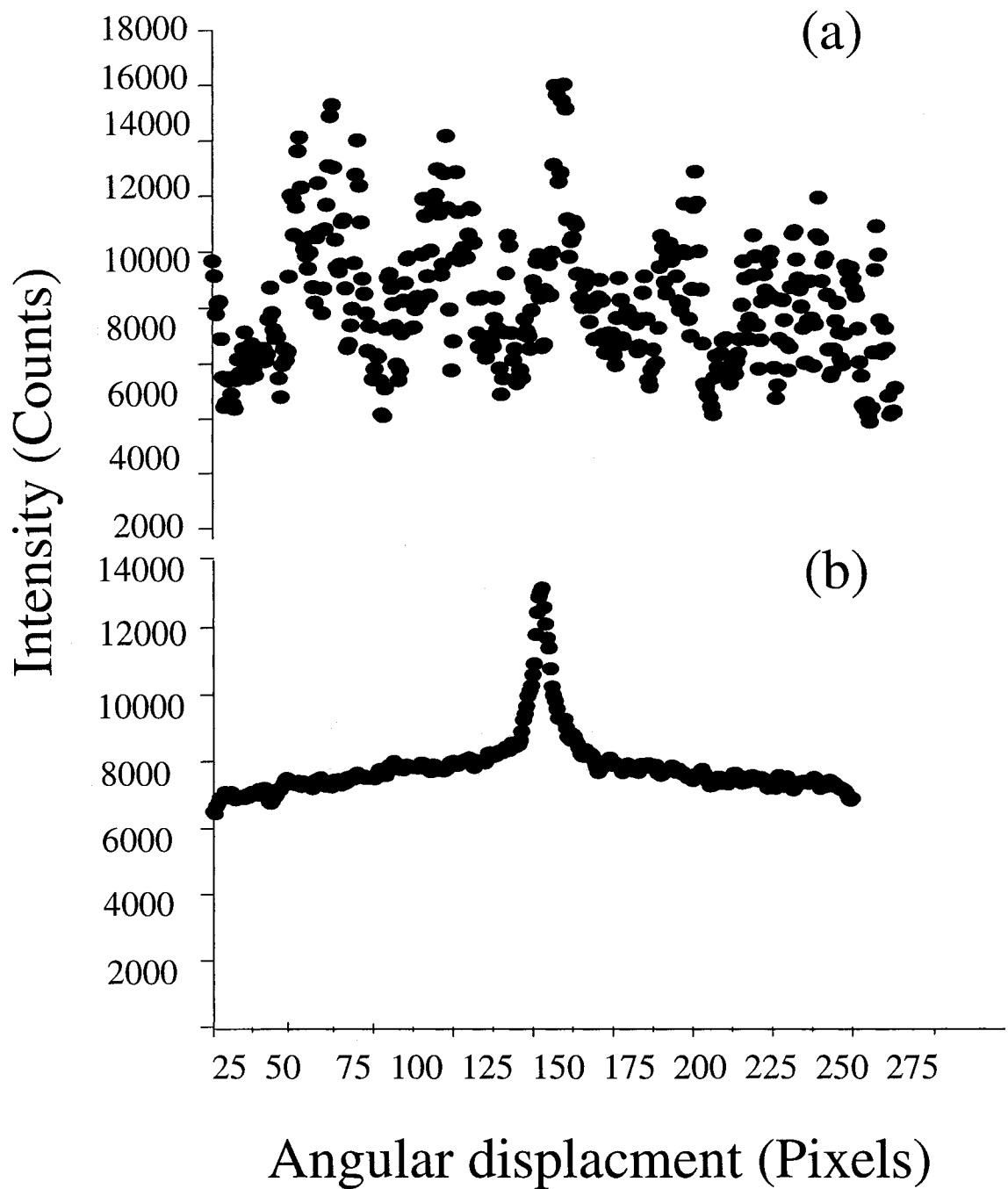


FIG. 2. Horizontal cross section through an intensity profile observed from 780 nm, collimated laser beam incident on a sample of fine grain sand. (a) the rapidly varying speckle pattern (b) the same cross section but with configuration averaging

all others. As opposed to interference between two paired amplitudes (at any  $\theta$ ) two reverse or conjugate paths always contribute to a maximum in the exact backscattering direction, that is at  $\theta = 0$ . This survives the averaging process, due to multiple scattering giving rise to an enhancement above the configuration averaged mean in the exact backscattering direction. Figure 2a shows the speckle pattern obtained without the configuration average, and the cone in the backscattering direction is shown in Figure 2b. It is possible to carry out the sum in (7) to incorporate more than three points but the result will still consist of sum of paired amplitudes squared and higher order interference terms specific to configurations. These may include a path that is the reverse of it own and recurrently scattered paths. In general the backscattered intensity  $I$  can be expressed as the sum of squares of three terms. The single scattering term  $I_S(\theta)$ - the squared sum of the single scattering amplitudes; the ladder terms  $I_L(\theta)$ - the squared sum of the multiple-scattering amplitudes with interference neglected; and the crossed terms  $I_C(\theta)$ - the coherent terms representing the interference between direct and reverse paths. Therefore the total backscattered intensity [28],

$$I(\theta) = I_S(\theta) + I_L(\theta) + I_C(\theta) \quad (8)$$

and the enhancement is the ratio of  $I(0)$  to the average background intensity  $I_S + I_L$  at large  $\theta$ ,

$$\alpha = 1 + \frac{I_C(0)}{I_S + I_L}. \quad (9)$$

The maximum of 2 is achieved when  $I_C(0) = I_L(0)$  with  $I_S = 0$ . Single scattering contributions can be nulled in certain polarization channels and the maximal contrast is when all paths and their reverse paths have the same amplitude, that is when the direct and the reverse paths are reciprocal. The equality of two CBS amplitudes, and complete constructive interference is assured if and only if,

$$\begin{aligned} \mathbf{k}' &= -\mathbf{k}, \\ \varepsilon'^* &= \varepsilon, \end{aligned} \quad (10)$$

where  $\mathbf{k}, \mathbf{k}'$  are the incident and backscattered wave vectors; and  $\varepsilon', \varepsilon$  are the field polarization vectors of the two waves respectively. In which case the conditions in equation (10) are satisfied, the enhancement is exactly a factor of two above the mean background.

### 2.1.2 Profile of the Backscattering Cone

When the backscattered intensity is observed from a sample uniformly illuminated by a coherent collimated beam the angular profile shown in Figure 2b is seen upon configuration averaging. Experimentally the configuration averaged result is realized by modifying the position of the scatterers. A solid sample of Teflon or white paint can be rotated around some fixed axis so that different configurations are observed. The configuration average of samples consisting of a colloidal suspensions occurs by virtue of the motion of the constituent particles due to thermal and Brownian motion. The process of configuration averaging replaces the sum of the amplitudes squared by the *sum of the paired amplitudes squared*. Each sum with an enhancement factor related to the phase difference of the two as given by the equation (6).

Since the coherent enhancement depends on the displacement between the first and the last scatterer  $\mathbf{r} - \mathbf{r}'$ , the sum of the intensities needs to account for the fraction of the source intensity  $P(\mathbf{r}, \mathbf{r}')$  of a ray starting at  $\mathbf{r}$  and exiting at  $\mathbf{r}'$ . The fraction  $P(\mathbf{r}, \mathbf{r}')$  can be approximated by the solution to the diffusion equation [32],

$$\frac{\partial p(r_i, r_t, t)}{\partial t} - D\nabla^2 p = f(R_0, t). \quad (11)$$

The solution  $p(r_i, r_t, t)$  of equation (11) is the probability of finding a photon that has traversed a path length  $s$  from  $r_i$  to  $r_t$  in time  $t$ . However  $P(\mathbf{r}, \mathbf{r}')$  is not concerned with a particular path length but represents the sum of all the paths originating at  $r$  and ending at  $r'$ . Therefore  $P(\mathbf{r}, \mathbf{r}')$  is the time independent, static solution to the diffusion equation. Since path length is given by  $s = vt$  where  $v$  is the wave velocity  $P(\mathbf{r}, \mathbf{r}')$  can be found by replacing  $t$  in equation (11) by  $s/v$  where  $v$  is the photon velocity in the medium and integrating over all possible  $s$ . The static solution for a point source in an infinite scattering medium is given by [8],

$$\begin{aligned} P(\mathbf{r}, \mathbf{r}') &= \int_0^\infty \frac{\exp[-(r - r')^2 v_t / 4Ds]}{(4\pi Ds/v_t)^{3/2}} ds \\ &= \frac{v_t}{4\pi D |\mathbf{r} - \mathbf{r}'|}. \end{aligned} \quad (12)$$

Here  $D = vl^*/3$  diffusion constant where  $l^*$  is the transport mean free path.  $P(\mathbf{r}, \mathbf{r}')$  is the Green's function solution to the three dimensional Laplace equation with a point source [8, 36]. In order to find  $P(\mathbf{r}, \mathbf{r}')$  for a random distribution of scatterers in the infinite half plane with the interface at  $z = 0$ , the boundary conditions are modified to account for the behavior and optical properties of light at the interface

[8, 37]. For the diffusion approximation to be valid the photons need to be diffusive—a coherent beam of photons incident at an interface can be considered diffusive when the photon paths are randomized. It is estimated that the photons are sufficiently randomized after travelling a distance of a mean free path given by  $l^*$ . Therefore it is necessary to locate the "source" term at some effective  $z = z_0 = l^*$  in the sample [8, 32]. It is also assumed that all photons incident at the interface are scattered and that attenuation and dispersion are neglected in this model. It can be shown then that the appropriate boundary condition for  $z = 0$  is [32],

$$P - C \frac{\partial P}{\partial z} = 0, \quad (13)$$

where

$$C = \frac{2l^*}{3} \frac{1 + R}{1 - R},$$

where  $R$  is the reflection coefficient at the interface. An approximate solution to the above problem can be found by linearizing the boundary condition given in equation (13). Expanding the linearized boundary condition around  $z = 0$  shows  $P$  to vanish at  $z = -C$ . It is now possible to guarantee that  $P(\mathbf{r}, \mathbf{r}') = 0$  for  $z = -C$  by placing an image source at  $\mathbf{r} = (x, y, -2C - z_0)$ . Therefore the linearized boundary condition allows the method of images to find a solution for  $P(\mathbf{r}, \mathbf{r}')$  for a slab of random scatterers in the half plane. The solution is given by,

$$P(\mathbf{r}, \mathbf{r}') = \frac{3}{4\pi l^*} \left\{ \frac{1}{[(x - x')^2 + (y - y')^2 + (z_0 - z')^2]^{1/2}} - \frac{1}{[(x - x')^2 + (y - y')^2 + (z' + z_0 + 2C)^2]^{1/2}} \right\} \quad (14)$$

The position of the last scatterer can be assumed to be close to the interface, so that  $z' \approx z_0$ . Then

$$P(\mathbf{r}, \mathbf{r}') = \frac{3}{4\pi l^*} \left\{ \frac{1}{r_{\parallel}} - \frac{1}{[r_{\parallel}^2 + 4(z_0 + C)]^{1/2}} \right\}, \quad (15)$$

where  $r_{\parallel} = (\sqrt{(x - x')^2 + (y - y')^2})$ . The total intensity in the direction  $\theta$ , along  $k_f$  is given by the sum of the paired intensities having paths originating at  $r$  and terminating at  $r'$  with each pair of paths having an interference factor given by  $\{1 + \cos[(\mathbf{k}_i + \mathbf{k}_f) \cdot (\mathbf{r} - \mathbf{r}')] \}$ . Therefore the total intensity can be written as,

$$\frac{I(\mathbf{k}_i, \mathbf{k}_f)}{I_0} = \frac{3}{(4\pi)^2 l^*} \int dr_{\parallel} \left\{ \frac{1}{r_{\parallel}} - \frac{1}{[r_{\parallel}^2 + 4(z_0 + C)]^{1/2}} \right\} \times \{1 + \cos[(\mathbf{k}_i + \mathbf{k}_f) \cdot (\mathbf{r} - \mathbf{r}')] \}, \quad (16)$$

where the extra factor of  $1/4\pi$  accounts for the fraction of intensity scattered into the direction  $\mathbf{k}_f$  at  $r'$ . The integration in equation (16) can be carried out analytically to obtain the following expression for the angular profile of the enhancement in backscattering;

$$\frac{I(\mathbf{q})}{I_0} = \frac{3a}{2\pi l^*} \left[ 1 + \frac{1 - \exp[-aq]}{aq} \right], \quad (17)$$

where  $a = 2(z_0 + C)$ , ( $\approx 4l^*$  when  $R \approx 0$ ) and  $q = |\mathbf{k}_f + \mathbf{k}_i| \approx \frac{2\pi\theta}{\lambda}$  when  $\theta$  is small. In the exact backscattering direction  $\theta$  is identically zero and the enhancement is a factor of two of the configuration averaged mean background. Also the width of the angular profile, the cone width and its dependence on the scattering mean free path can be estimated from equation (17). If the width of the cone is taken at  $1/e^{-1}$  above the background, its width is defined by the condition

$$aq = 1, \quad (18)$$

giving an approximate width,

$$\Delta\theta \approx \frac{\lambda}{4\pi l^*}. \quad (19)$$

In light scattering from classical samples the measured average width of the backscattering peak,  $\delta\theta$  is only a fraction of a degree. The above derivation is strictly for scattering of scalar waves and ignores the polarization of such waves. Also ignored as mentioned previously is dispersion and attenuation. Experimentally it is seen that the enhanced backscattering of light is strongly dependent on the polarization. Maximum enhancement is observed for circularly polarized incident light with detection of the same polarization. In this particular channel the single scattering contribution is removed by the cross polarized analyzer. The complete vector treatment of multiple scattering from classical particles or atoms is beyond the scope of this experimental study [33, 34, 35]. In this thesis only the qualitative and experimental results of polarization and spectral effects will be discussed.

## 2.2 WAVE SCATTERING IN DILUTE ATOMIC GASES

References to light scattering date back to the literary work of da Vinci and the first quantitative treatment of scattering was that Lord Rayleigh's explanation of the blue sky [36]. The first to study multiple scattering of resonant radiation in atomic vapors was Compton in 1922 [38]. Compton assumed a *mean free path* in which the resonant photons will be quickly reabsorbed and re-emitted resulting in the photons



performing a random walk, satisfying a diffusion equation similar to particle diffusion [38]. Such a photon will exit the medium with a time dependence given by (assuming a pulsed excitation at time  $t = 0$ )  $\exp(-A_{21} \cdot t/g_0)$ , where  $A_{21}$  is the Einstein coefficient for spontaneous emission and the trapping factor  $g_0$  is proportional to the average number of absorption and re-emission processes. Due to the extra time delay resulting from  $g_0$  the process is better known as "radiation trapping". This picture of photon diffusion holds if the photons can maintain the same frequency after each absorption and reemission process. Due to various line broadening mechanisms the photon can change frequency at each absorption/emission process, an effect known as 'frequency redistribution,' making it impossible to define an *average mean free path* [39]. The average mean free path can be shown to diverge in the presence of line broadening mechanisms and the radiation trapping problem cannot be described by a diffusion equation. The particle like diffusion model was extended to accommodate frequency redistribution by Holstein in 1947 [38, 39]. Holstein derived an integro-differential equation to describe intensity transport in vapors in the presence of frequency redistribution, but it too ignores phase correlations that can be present in multiple scattering and does not account for interference effects.

Since Holstein, multiple light scattering has been studied extensively by the atomic physics, astrophysics, and biological physics communities. Most studies of multiple scattering of radiation in vapors until recently have exclusively dealt with incoherent transport of intensities, ignoring the possibility of interference. The phase correlations that could arise in multiple scattering were not expected to survive in the presence of rapid dephasing due to the thermal motion of the atoms in a hot vapor. Therefore the effects due to multiple scattering in atomic gases were not investigated until recently. With the developments in laser cooling techniques for atoms, however a completely new regime of ultra low temperature samples has been made available for scattering studies. It is important to recognize that it might still be possible to observe coherent scattering from even hot vapors, and such studies have been proposed by this group and are currently underway.

Near-resonance multiple scattering from atoms is fundamentally different from scattering from point like dipole scatterers. For weak fields these differences are almost exclusively due to the internal quantum mechanical structure of the atom. In the absence of line broadening mechanisms the scattering cross section of the atoms

is highly resonant with a  $Q$  of approximately  $10^8$  and the principal resonance frequency is the same for all the atoms [24]. Unlike classical scatterers, the scattering cross section of atoms can be easily manipulated by changing the frequency only a fraction of a line width from resonance. For coherent backscattering to be observed, the configuration of the scatterers should be maintained during the direct and reverse scattering events. In non-resonant scattering the time scale of interest is the propagation time between two scatterers which is extremely short and the motion of the scatterers is small enough to maintain the phase correlation between the direct and the reverse paths. The time scale of interest for resonant atoms is the considerably longer on-resonant time delay which is dependent on the width of the transition  $\Gamma$  as  $\tau_{res} = 2/\Gamma$  [24, 33]. For dephasing to be negligible the displacement of the scatterers during this time scale must be less than or equal to the wavelength of the light,

$$\Delta x = v\tau_{res} \geq \lambda, \quad (20)$$

and the corresponding critical velocity  $v_{crit} = \Delta x/\tau_{res}$  to observe coherent backscattering is,

$$v_{crit} \sim \frac{\lambda}{\tau_{res}} = \frac{\lambda\tau}{2}, \quad (21)$$

and the line broadening due to this velocity is  $kv_{crit} \approx \Gamma$ . For observation of coherent backscattering from a collection of  $^{85}\text{Rb}$  which has a natural width of  $\Gamma = 5.98$  MHz, the atoms need to be cooled to a temperature  $T_{crit} = 0.25$  K, for light at resonance frequency. This is a temperature that is easily achieved by laser cooling techniques. This condition is more severe for multiple scattering and the temperature needs to be even lower, but this too is easily achieved by a combination of laser cooling and magnetic trapping.

### 2.2.1 Single Scattering from a Two Level Atom

In order to develop a qualitative picture of multiple scattering it is necessary to derive the single scattering cross section for atoms in a dilute vapor. It is this that determines the conditions necessary for multiple scattering to take place in a vapor and determines what fraction of the incident beam interacts with the atoms of interest. The result for the single scattering cross section will be derived in the weak field regime for a two level atom in the absence of velocity or collisional induced line broadening effects. The atomic Hamiltonian in the presence of a monochromatic

light field (perturbation) can be written as,

$$H(t) = H_0 + H'(t) \quad (22)$$

where the eigen functions  $\phi_n(\vec{r})$  of the zero order Hamiltonian  $H_0$  are known. The corresponding eigen values are  $E_n = \hbar\omega_n$ . The time dependent Schrödinger equation describing the atom and the field interaction is,

$$H\psi(\vec{r}, t) = i\hbar \frac{\partial \psi(\vec{r}, t)}{\partial t}. \quad (23)$$

The eigen functions  $\phi_n(\vec{r})$  form a complete set. Then the solution  $\psi(\vec{r}, t)$  of the equation (23) can be expanded in terms of the eigen functions  $\phi_n(\vec{r})$  as,

$$\psi(\vec{r}, t) = \sum_k C_k(t) \phi_k(\vec{r}) e^{-i\omega_k t}, \quad (24)$$

where the coefficient  $C_k(t)$  are time dependent [40, 41]. The probabilities  $|C_k(t)|^2$  are the transition probabilities to an excited state  $k$  and equivalently the rate of loss of energy from the field [41]. If the initial values of the probability amplitudes are known the time evolution of the amplitudes can be found from (23). Substitution of (24) into (23) gives,

$$i\hbar \sum_k (\dot{C}_k - i\omega_k C_k) e^{-i\omega_k t} \phi_k = \sum_k (\hbar\omega_k + H') e^{-i\omega_k t} \phi_k C_k. \quad (25)$$

Multiplying both sides of (25) by the  $\phi_j^*(\vec{r})$  and integrating over the spatial coordinate  $\vec{r}$  gives the time derivative of the probability amplitudes as,

$$\dot{C}_k = -\frac{i}{\hbar} \sum_k C_k H'_{jk} e^{-i(\omega_k - \omega_j)}, \quad (26)$$

where the orthogonality condition  $\int d^3r \phi_k(\vec{r}) \phi_j^*(\vec{r}) = \delta_{jk}$  has been used. Here the matrix elements of the perturbing Hamiltonian are given by

$$H'_{jk} = \langle \phi_j | H' | \phi_k \rangle = \int d^3r \phi_j^* H'(\vec{r}) \phi_k(\vec{r}), \quad (27)$$

where,

$$H' = -e\vec{E}(\vec{R}, t) \cdot \vec{r}. \quad (28)$$

For an atom in the field of a plane wave travelling in the positive  $z$  direction the electric field operator is,

$$\vec{E}(\vec{r}, t) = E_0 \hat{e} \cos(kz - \omega t),$$

where  $E_0$  is the electric field amplitude and  $\hat{\varepsilon}$  is the unit vector in the direction of the field polarization. Using the electric-dipole approximation, in which the wave length of the incident electric field is assumed much longer than the extent of the atom (field does not depend on the atomic coordinates), the matrix elements of the interaction Hamiltonian  $H'(t)$  can be written as [41, 42],

$$H'_{jk} = -eE_0 \langle j | r | k \rangle. \quad (29)$$

Substituting into (25) gives,

$$\begin{aligned} \dot{C}_2 &= \frac{1}{2}\Omega[e^{i(\omega_{12}-\nu)t} + e^{i(\omega_{12}+\nu)t}]C_1 \\ \dot{C}_1 &= \frac{1}{2}\Omega[e^{-i(\omega_{12}-\nu)t} + e^{-i(\omega_{12}+\nu)t}]C_2, \end{aligned} \quad (30)$$

where  $\Omega$  is the Rabi frequency defined by

$$\Omega = \frac{eE_0}{\hbar} \langle 1 | r | 2 \rangle,$$

and

$$\omega_{12} = \omega_1 - \omega_2$$

is the resonance frequency. The coupled differential equations (30) can be decoupled in the weak field regime where the Rabi frequency is small. For the initial conditions  $C_1(0) = 1$  and  $C_2(0) = 0$  the equations of motion (30) reduces to,

$$\begin{aligned} \dot{C}_1 &\approx 0 \\ \dot{C}_2 &= i\frac{1}{2}\Omega[e^{i(\omega_{12}-\nu)t} + e^{i(\omega_{12}+\nu)t}] \end{aligned} \quad (31)$$

This gives for the coefficients

$$\begin{aligned} C_1(t) &\approx C_1^{(0)}(t) = 1, \quad C_1^{(1)} = 0 \\ C_2(t) &\approx C_2^{(1)}(t) = i\frac{1}{2}\Omega \left\{ \frac{e^{i(\omega_{12}-\nu)t} - 1}{(\omega_{12} - \nu)} + \frac{e^{i(\omega_{12}+\nu)t} - 1}{(\omega_{12} + \nu)} \right\} \end{aligned} \quad (32)$$

where the superscript  $(n)$  indicates the number of times the perturbing field has acted ( $n = 0$  or  $n = 1$ ) [41]. Using the rotating wave approximation (RWA) to drop terms of the order  $(\omega + \nu)$  as  $(\omega + \nu \gg 1)$  and  $(\omega - \nu \approx 0)$  the equations (30) reduce to [41, 40],

$$\begin{aligned} \dot{C}_2 &= i\frac{1}{2}\Omega \left[ \frac{e^{i(\omega_{12}-\nu)t} - 1}{(\omega_{12} - \nu)} \right] C_1 \\ \dot{C}_1 &= i\frac{1}{2}\Omega \left[ \frac{e^{-i(\omega_{12}-\nu)t} - 1}{(\omega_{12} - \nu)} \right] C_2, \end{aligned} \quad (33)$$

The solution to the excited state probability amplitude to first order is given by,

$$C_2(t) = i\frac{1}{2}\Omega \frac{\sin[(\omega_{12} - \nu)t/2]}{(\omega_{12} - \nu)/2} e^{i\frac{(\omega - \nu)t}{2}}. \quad (34)$$

The finite life time of the excited levels due to spontaneous emission can be included by adding a phenomenological exponential decay with a decay constant  $\gamma_i, i = 1, 2$  to the equations of (30) [41]. The probability per unit time that the atom decays from level 2 is given by  $\gamma_2|C_2|^2$ . Then  $\gamma_p$  for spontaneous emission is given by the time integral of this distribution,

$$\gamma_p \approx \gamma_2 \int_0^\infty |C_2|^2 dt. \quad (35)$$

Therefore the spectral response of the atom is given by the following Lorentzian

$$\gamma_p \approx \frac{1}{2} \frac{\Omega^2}{(\omega_{12} - \nu)^2 + \gamma_2^2}, \quad (36)$$

with its full width half maximum,  $\gamma_2$  defined by the natural width of the transition. This expression for the scattering rate is only an approximate solution for the two level atom in a weak field. The exact solution is found by the full quantum mechanical treatment of the atom and the field (see for example, Weissbluth [42], Loudon [43]). The exact solution for the scattering rate for in a weak field is,

$$\gamma_p = \frac{s_0\gamma/2}{1 + (2\delta/\gamma)^2}, \quad (37)$$

where  $s_0$  is the saturation parameter defined as the ratio of incident laser power density  $I_{inc}$  to the saturation power density  $I_s = \pi\hbar c/3\lambda^3\tau$ . The equation (37) is valid in the limit  $s_0 \ll 1$ . The scattering rate is still a Lorentzian with its width being the natural width of the transition. The amount of scattered power per unit volume is given by  $\hbar\omega\gamma_p n$ , where  $n$  is the density of the interacting atoms. The attenuation of a laser beam in transmission through some distance  $x$  through an infinite slab of an atomic vapor sample is given by

$$\begin{aligned} \frac{dI(x)}{dx} &= -\sigma_{12}(\omega)nI \\ I(x) &= I_0 \exp[-\sigma_{eg}(\omega)nx]. \end{aligned} \quad (38)$$

The equation (38) defines the optical depth,  $b = \sigma_{eg}(\omega)nx$ , or the opacity of the sample. The above equation is generally referred to as the Lambert-Beer's law. The probability for multiple scattering which is required for observation of enhanced

backscattering depends on the optical depth. At low opacity a smaller number of photons are singly scattered out of the beam, and fewer single contributions translate to correspondingly fewer double and higher order events. Analogous to a classical sample where the number of single scattering events are proportional to the number of scatterers  $N$ , and the probability of double scattering is proportional to  $N(N-1)$  [1, 31]. In case of a spherically symmetric sample of vapor with a Gaussian density distribution, as considered here in this study, the above equation (38) needs to be modified. If the density distribution is expressed as

$$n(r) = n_0 \exp(-r^2/2r_0^2), \quad (39)$$

where  $n_0$  is the cloud density at the center of the sample and  $r_0$  is the *rms* radius. Then the total transmitted intensity is given by

$$I(x) = I_0 e^{-\int n(r)\sigma(\omega)dx} \quad (40)$$

The optical depth,  $b = -\int n(r)\sigma(\omega)dx$  of this sample can be shown to be  $b = \sqrt{2\pi}\sigma_0 n_0 r_0$ , where  $\sigma_0$  is the on-resonance scattering cross section. The number of atoms in the cloud is given by

$$N = \int n(r)dr = \left(\frac{\pi}{2}\right)^{3/2} n_0 r_0^3. \quad (41)$$

The optical depth  $b$  determines the probability of subsequent scattering, with large optical depths translating to a high multiple scattering probability. In general for multiple scattering to take place, and for observation of coherent backscattering the optical depth of the sample is required to be larger than 1. The enhancement in coherent backscattering is relative to the incoherent background as described previously.

### 2.2.2 Single scattering intensity and its angular dependence on polarization

The intensity distribution of light from an atom that decays from levels of angular momenta  $F' \rightarrow F$  depends on the detection geometry, the detected polarization and on the coupling of angular momentum of the atom to that of the excitation photon. The geometry of the collision and detection is shown in Figure 3. The two coordinate frames are related using the rotation matrices whose arguments  $(\phi, \theta, \chi)$  are the Euler

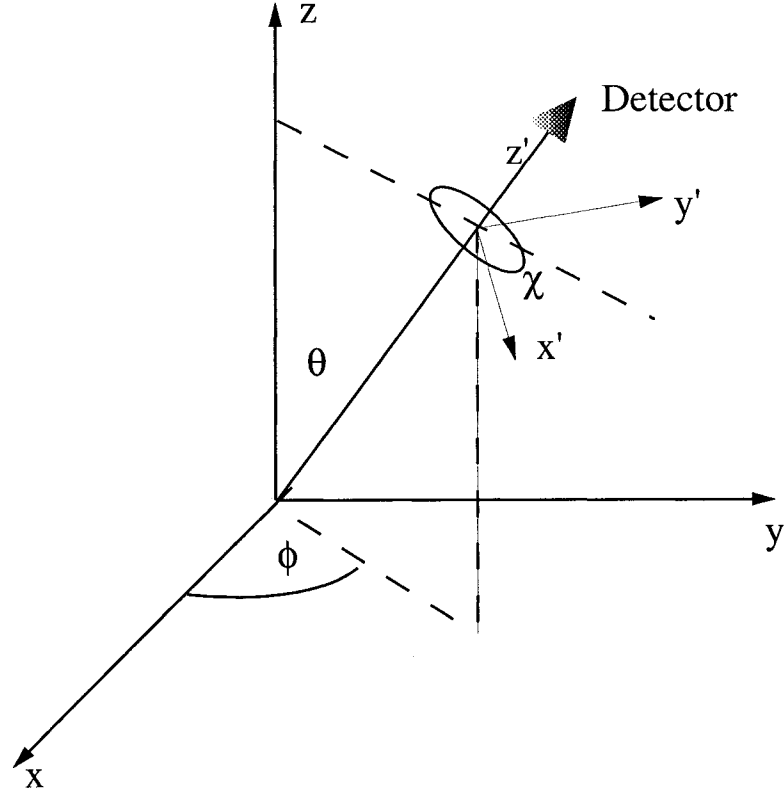


FIG. 3. The excitation frame with the quantization axis defined by  $z$  and the detection frame with the  $z'$  axis along the direction of detection.

angles required to rotate the  $(x, y, z)$  collision frame to the primed  $(x', y', z')$  detection frame [45]. The detected intensity in the primed coordinate system is given by,

$$I(\theta, \chi, \beta) = \frac{I_0}{4\pi} \left[ 1 + \frac{3}{2} h^{(1)}(F, F') \cos \theta \sin 2\beta \langle O_0 \rangle - \frac{1}{2} h^{(2)}(F, F') \langle A_0 \rangle P_2(\cos \theta) \right. \\ \left. + \frac{3}{2} h^{(2)}(F, F') \langle A_0 \rangle \sin^2 \theta \cos 2\chi \cos 2\beta \right] \quad (42)$$

where the polar angle  $\theta$ , and the orientation of the linear polarization analyzer in front of detector  $\chi$ , is as defined in Figure 3. The polarization of the detected light is defined by the angle  $\beta$ ,  $\beta = 0, \pi/2$ , and  $\beta = \pm\pi/4$  respectively defines the two linear polarizations and the two helicity channels. In the geometry of this experiment,  $\phi = 0$  and  $\chi = 0, \pi/2$ .

The terms  $h^{1,2}(F, F')$  are solely dependent on the final and initial angular momentum states of the excited atoms [45]. The terms  $\langle O_0 \rangle$ , and  $\langle A_0 \rangle$  are the orientation

and the alignment, the expectation values of certain combination of angular momentum operators in the collision frame. Explicitly the orientation or the vector polarization is given by,

$$\langle O_0 \rangle \equiv \sum_{M'} \frac{|a(M')|^2 M'}{\sqrt{F'(F'+1)}}; \quad (43)$$

and the alignment is given by

$$\langle A_0 \rangle \equiv \sum_{M'} \frac{|a(M')|^2 (3M'^2 - F'(F'+1))}{F'(F'+1)}. \quad (44)$$

The transition of interest in this study is the  $F = 3 \rightarrow F' = 4$  cycling transition of  $^{85}\text{Rb}$ . For linearly polarized detection,  $\beta = 0$ , the equation (42) reduces to,

$$I(\theta, \chi, 0) = \frac{I_0}{4\pi} \left[ 1 + \frac{1}{2} h^{(2)}(3, 4) \langle A_0 \rangle P_2(\cos \theta) \pm \frac{3}{4} h^{(2)}(3, 4) \langle A_0 \rangle \sin^2 \theta \right]. \quad (45)$$

Likewise the single scattering intensities in circular channels are given by,

$$I(\theta, \chi, \pm\pi/4) = \frac{I_0}{4\pi} \left[ 1 \pm \frac{3}{2} h^{(1)}(3, 4) \langle O_0 \rangle \cos \theta - \frac{1}{2} h^{(2)}(3, 4) \langle A_0 \rangle P_2(\cos \theta) \right], \quad (46)$$

where  $h^{(1)}(3, 4) = 5/\sqrt{20}$  and  $h^{(2)}(3, 4) = -5/7$ . Figures (4) and (5) show the calculated angular intensity distributions for linear and circular polarization channels for the transition  $F = 3 \rightarrow F' = 4$ . These single scattering amplitudes determine the probability of subsequent multiple scattering and the relative size of the incoherent background in each polarization channel. The theoretical dependence in multiple scattering on polarization is an area of current research activity. It is emphasized that the results of single scattering analysis show that polarization effects are quite important, and it is a goal of this study to quantify these effects.

### 2.3 MULTIPLE SCATTERING AND POLARIZATION

The two level atom in the light field is described by a single Rabi frequency. For scattering from an atom with many levels that can be coupled by the light field, the polarization of the field needs to be accounted for. Previously multiple scattering and interference were considered assuming scalar waves neglecting polarization. The polarization vectors of the incident and the scattered fields,  $\varepsilon$  and  $\varepsilon'$ , each respectively define two orthogonal polarization channels. Therefore the CBS signal can be observed in four independent polarizations channels. Coherent backscattering



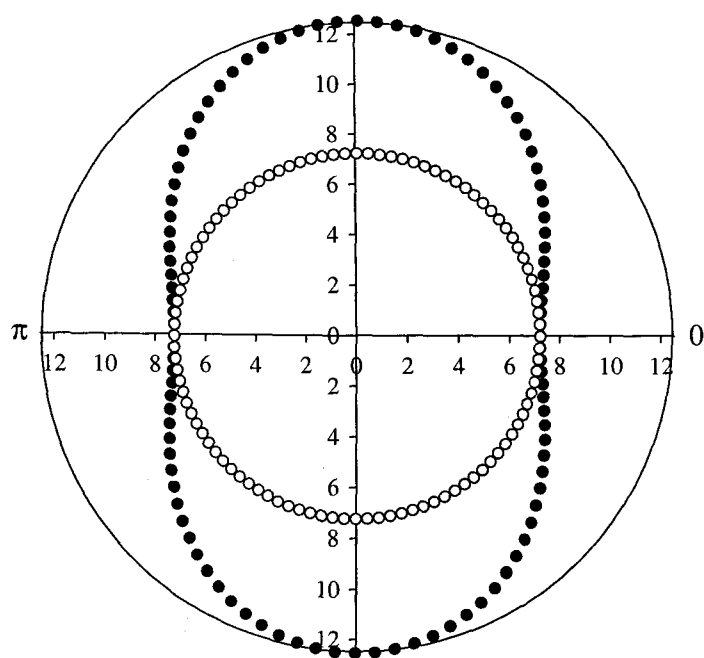


FIG. 4. Angular distribution of linearly polarized light due to single scattering.

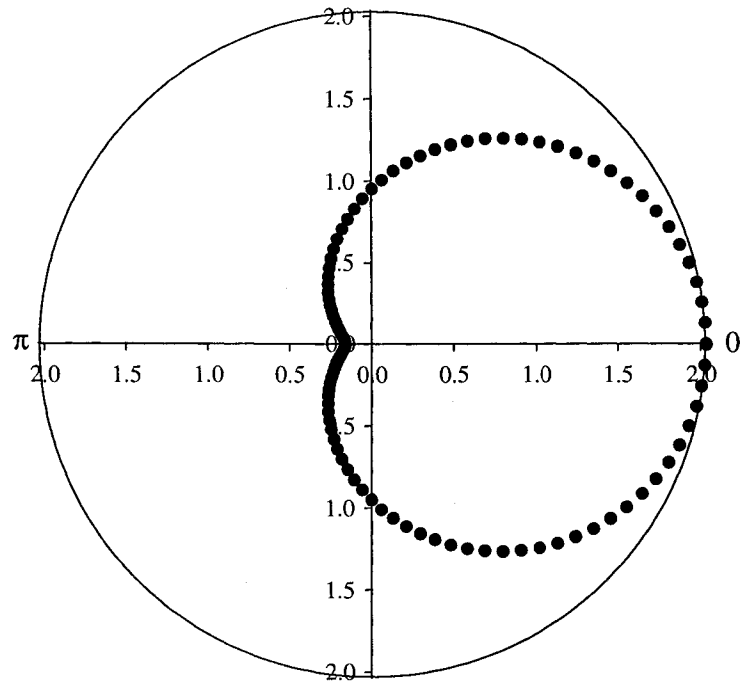


FIG. 5. Angular distribution of circularly polarized light, intensity in the backwards direction is minimum in the helicity preserving channel.

from classical scatterers and cold atoms show a distinct dependence on the incident and the observed polarization channel [6, 24]. For linear incident polarization the scattered light may be analyzed parallel or perpendicular to the incident polarization. In the linear case the parallel channel will be denoted by  $l||l$  and the perpendicular channel will be denoted by  $l\perp l$ . For circularly polarized incident light the two orthogonal channels are those of same and opposite helicity. In the helicity preserving(non-preserving) channel the detected light is of the same(opposite) helicity as the incident light. The helicity preserving channel will be denoted  $h||h$  and the helicity non-preserving channel will be denoted  $h\perp h$ . It should be noted that the single scattering contribution  $I_S$  (see (9)) is absent in the backscattering direction for scatters of spherical symmetry in the channels  $l\perp l$  and  $h||h$  [46]. And in the absence of any Faraday effects  $I_C(0) = I_L$ . Then the enhancement in the  $h||h$  can be expected to be a factor of 2 for classical scatterers [28, 47, 48]. Therefore, in the case of scattering from classical particles, reciprocity can be assured by careful selection of experimental parameters, such that the reciprocity conditions (10) are met. This is not the case for scattering from an atom with more than two levels that can be coupled by the light field. The only atomic transitions that preserve reciprocity relations are the dipole transitions of the type  $F = 0 \rightarrow F_e = 1$  in the  $l||l$  channel.

In general the atom is not a two level system and the multiple levels of the atom can be coupled by the light field. Figure 6 shows the possible Rayleigh and Raman transitions for the degenerate atomic dipole transition between the levels  $F_g = 1$  and  $F_e = 2$ . In the absence of an external magnetic field the levels are  $2F + 1$ - fold degenerate and all transitions are nearly elastic, neglecting recoil. The atom has a high probability to make a spontaneous Raman transition to degenerate Zeeman levels, where the final state will differ from the initial state. This scenario implies that the polarization of the scattered light will be different from that of the incident polarization [24]. Therefore it is not always possible to reject the singles scattering contribution,  $I_S$ , even in the helicity preserving channel. Also it is not always possible to satisfy the maximal enhancement condition  $I_C(0) = I_L$  due to the statistical nature of the Zeeman transitions in a multiple scattering chain. To illustrate this, Figure 7 shows a direct and reverse path through double Rayleigh transition in the  $h||h$  channel that can give a zero interference contribution [24]. In this example an atom makes a transition between Zeeman sublevels corresponding to  $m \rightarrow m' = m + 1$ , with  $\Delta m = -1$  by absorbing a  $\sigma^+$  photon. In the helicity preserving channel  $\sigma^-$

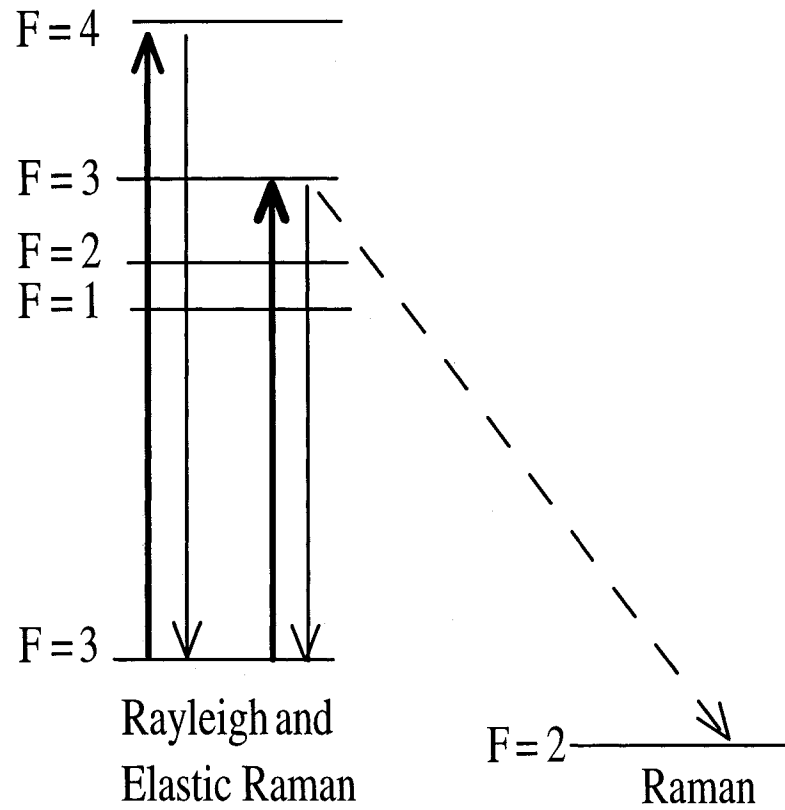


FIG. 6. A degenerate atomic dipole transition which allows Rayleigh and elastic (degenerate) Raman transitions. The Rayleigh and elastic Raman transitions are indicated by the solid lines; the dashed line indicates a Raman transition.

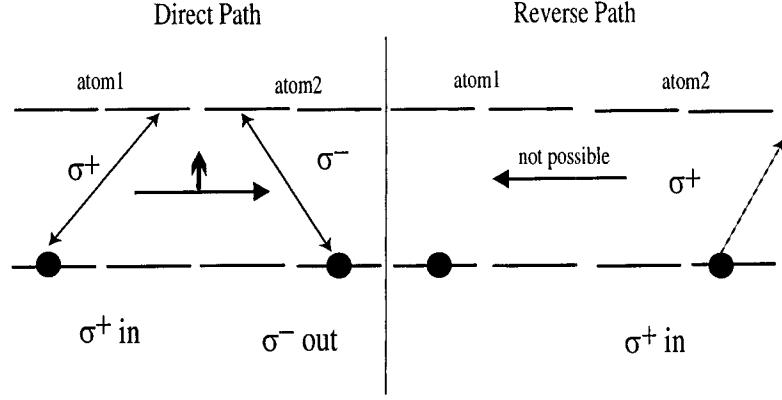


FIG. 7. Violation of maximal contrast criterion due to the atom's internal structure. The two atoms are located in the plane of the paper and the light is incident into the paper. The atoms are in two different Zeeman sublevels. The incident polarization is  $\sigma^+$ . In the  $h||h$  channel, the  $\sigma^-$  polarization will be detected. The direct scattering path, and the reverse path are shown in the left and the right sequence respectively [24].

polarization is detected. The excited atom radiates linearly polarized light towards another atom as shown in Figure 7. The second atom sees the Rayleigh scattered, linearly polarized photon as a superposition of the  $\sigma^+$ ,  $\sigma^-$  polarizations. This allows it to scatter a  $\sigma^-$  photon through a transition satisfying the selection rule  $\Delta m = 1$ . Reciprocity is lost if this atom is not able to again scatter a  $\sigma^+$  photon as is the case for a two fold degenerate atom shown in this example. Here the reverse path for interfering is not available leading to reduced enhancement in the interfering signal due to the internal quantum mechanical structure of the scatterers [24].

It is possible to think that Raman transitions would not contribute to interference in the backscattering direction and that this incoherence contributes to loss of contrast in backscattering [28]. The elastic Rayleigh and the degenerate Raman transitions both can interfere and contribute to the backscattering interference signal. The direct and the reciprocal paths that can interfere for Raman-type backscattering for the specific situation of two atoms located linearly along the propagation direction of the incident light is shown in Figure 8 [1]. The interference between Raman channels can be understood from the transition diagrams shown in Figure 9 in the basis,

$$|x\rangle = \frac{1}{\sqrt{2}} [|1, +1\rangle - |1, -1\rangle]$$

$$\begin{aligned}
|y\rangle &= \frac{i}{\sqrt{2}} [|1, +1\rangle + |1, -1\rangle] \\
|z\rangle &= |1, 0\rangle.
\end{aligned}
\tag{47}$$

The solid and dashed-dotted arrows in Figure 9 indicate the transitions open for direct and reverse paths leading to the polarization transformation shown in Figure 8.

The first observations of coherent backscattering of light in ultra cold gases, specifically  $^{85}\text{Rb}$  was observed by Labeyrie *et al* [24]. The discrepancies between scattering from classical dipole-like objects and the gas was soon attributed to the internal structure of the atom. This experimental work looks further, specifically at the polarization and spectral dependence of coherent backscattering, from the gas at conditions not studied previously.

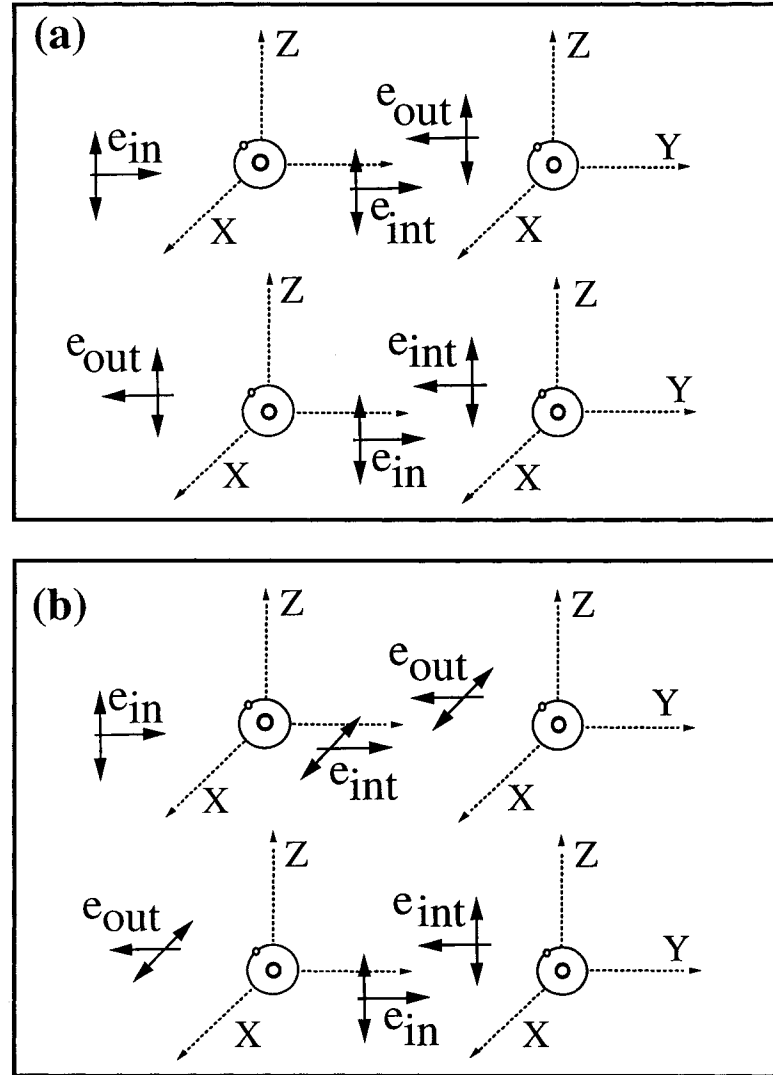


FIG. 8. Diagrams showing direct and reciprocal paths for (a) Rayleigh-type, and for (b) Raman-type coherent backscattering for two atoms located along the propagation direction of the incident light [1].

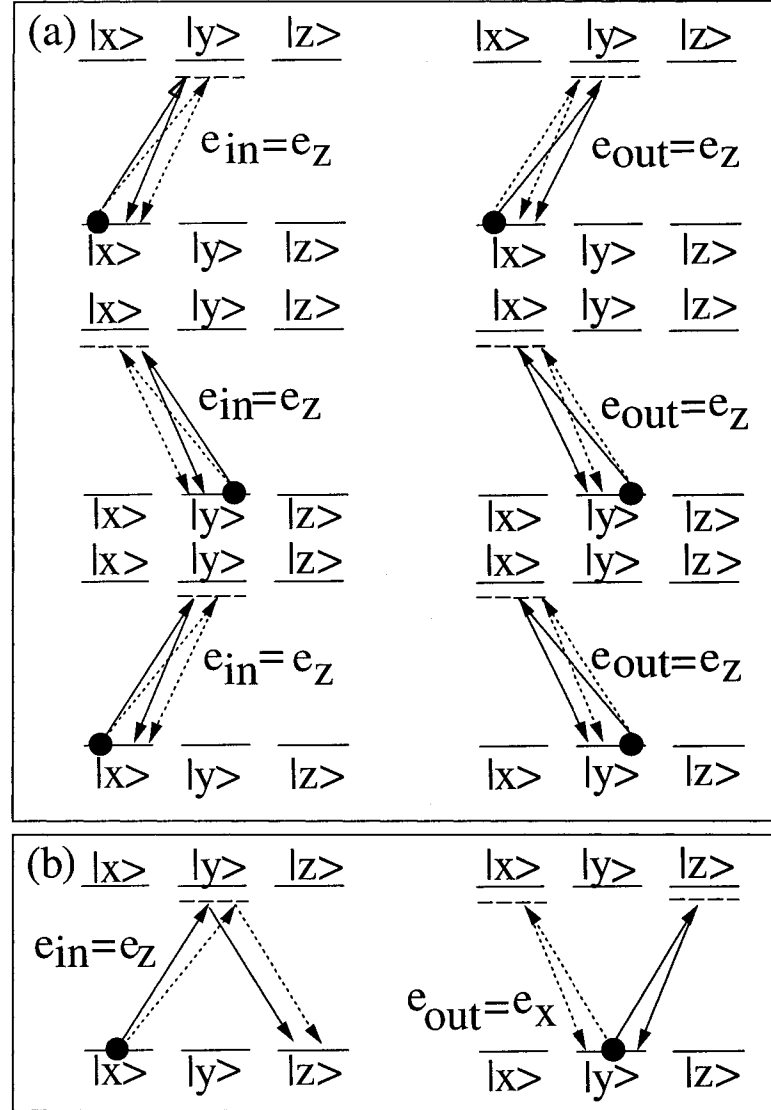


FIG. 9. Diagrams showing the transitions open for Rayleigh-type and Raman-type, (a) and (b) respectively for coherent backscattering in the geometry of Figure 8. The solid circles show the state-designation of atoms and the solid and dashed-dotted arrows indicate the transitions open for direct and for reciprocal scattering paths respectively [1].



## CHAPTER 3

### EXPERIMENT

As described in the previous chapter, the observation of an enhanced backscattering signal is indicative of coherent transport of incident radiation in the sample. In this experiment the spatial, spectral, and polarization dependence of the CBS signal from a well characterized sample of ultracold  $^{85}\text{Rb}$  is measured. In this chapter the experimental setup and the basic scheme of the experiment is discussed in detail.

#### 3.1 EXPERIMENT OVERVIEW

An energy level diagram of the hyperfine levels of the  $^{85}\text{Rb}$  atom relevant to the experiment is shown in Figure 10. The probe laser is tuned close to the  $5s^2S_{1/2} F=3 \rightarrow 5p^2P_{3/2} F'=4$  transition. Here  $F(F')$  denotes the ground(excited) hyperfine levels. The intrinsic nuclear spin of  $^{85}\text{Rb}$  is  $I=5/2$ . The total angular momentum  $F$  is given by  $F = I + J$ , where  $J = 3/2$ . The excited state hyperfine manifold consists of  $(2J+1)=4$  (for  $J < I$ ) levels as shown in Figure 10. The probe laser is actively stabilized [49], and locked to a saturated absorption crossover resonance of the excited hyperfine manifold [50, 51]. The locked laser can be offset in frequency to be at resonance or close to resonance with any one of the excited levels of the hyperfine manifold by an acousto-optic modulator. In this experiment the probe laser is tuned a few line-widths to either side of the  $F = 3 \rightarrow F' = 4$  transition. The laser line-width by itself is a few hundred KHz, which is much smaller than the 5.98 MHz natural width of the  $F = 3 \rightarrow F' = 4$  transition. The frequency stabilized probe laser is spatially filtered, expanded, and transmitted through a beam splitter to the sample. The backscattered photons are reflected by the beam splitter to the detection polarimeter consisting of the polarization analyzer and the detection optics as shown in Figure 11.

The probe beam incident on the beam splitter is polarized vertically. The reflected portion of the beam is directed into a beam dump far from the sample to eliminate scattering back into the detection system. The backscattered light is observed in each of the four polarization channels listed in Table I. The vertically polarized probe is circularized by the  $1/4$  wave retarder plate (QWP) inserted between the sample and the beam splitter for the measurements in the helicity channels as shown in Figure

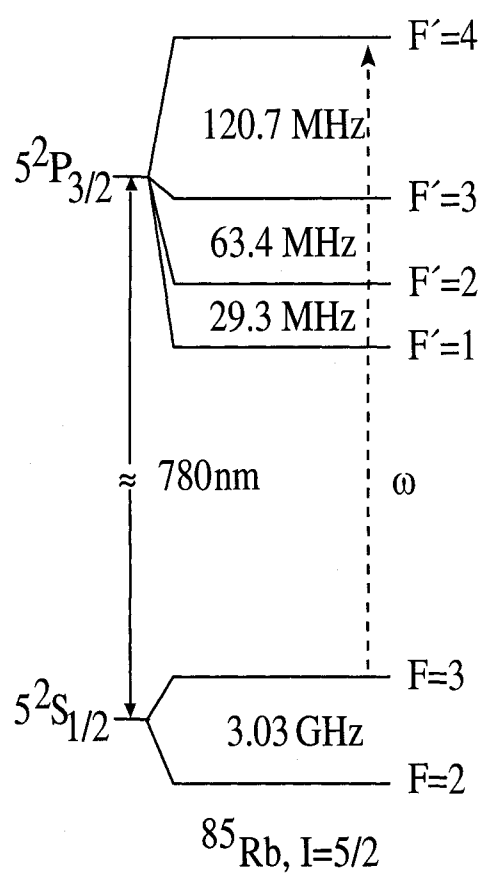


FIG. 10. The level diagram of the  $^{85}\text{Rb}$  hyperfine manifold.

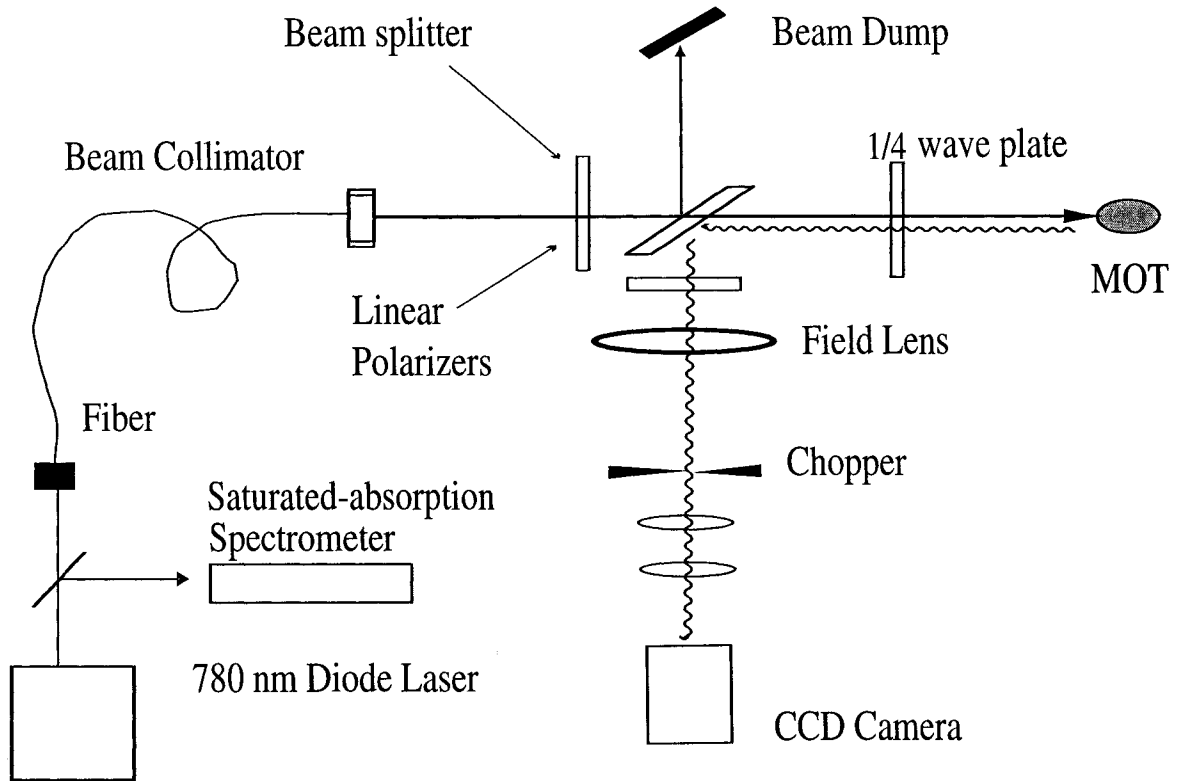


FIG. 11. Schematic of the experimental setup

11.

The detector itself is a liquid nitrogen cooled low noise charge couple device (CCD) camera, with a high dynamic range. The camera is able to detect extremely small signals and is able to accumulate signals for an extended period of time with negligible addition of electronic noise. The instrument consisting of the probe, the polarimeter and the beam dumps is able to measure the backscattering signal from almost any sample with configuration averaging. A sample of fine grain  $\text{TiO}_2$  powder suspended in water at various concentrations is used to determine the instrument resolution. The detected signals are stored in a computer for analysis.

During data acquisition, extreme care is needed in suppressing background and light scattered from various elements along the detection path. Generally the signal to noise ratio is superior in the two channels in which the single scattering contribution can be nulled. These are the  $l \perp l$ , and the helicity preserving  $h \parallel h$  channels. Much of the noise is due to scattering from various optics even though the optics used are anti-reflection coated specifically for the wavelength and the angle of incidence. The

TABLE I. The detection polarization channels defined relative to the incident polarization.

Channel	Incident	Detected	Detection Channel
$l  l$	$\uparrow$	$\uparrow$	linear parallel
$l\perp l$	$\uparrow$	$\rightarrow$	linear perpendicular
$h  h$	$\sigma_{\pm}$	$\sigma_{\mp}$	helicity preserving
$h\perp h$	$\sigma_{\pm}$	$\sigma_{\pm}$	helicity non-preserving

data are saved as collected without any preprocessing, the background corrections are carried out at the time of analysis. At the start of each data run the beam alignment and position is checked by looking at the robust, and reproducible degenerate four-wave mixing signal resulting from the two of the trapping beams and the probe.

### 3.2 DESCRIPTION OF THE EXPERIMENTAL SETUP

The experimental setup consists of three main components; the probe laser, the polarimeter, and the sample. The experimental setup is shown in Figure 11. The sample is illuminated by a well characterized probe laser. The backscattered light from the sample is polarization analyzed and detected by the polarimeter which consists of the analyzing polarizer, the transport optics and the CCD. In the following sections each stage will be discussed in detail.

#### 3.2.1 Probe Laser

The probe laser is an external cavity diode laser (ECDL) in the Littman-Metcalf configuration [52]. A schematic of the ECDL is shown in Figure 12. The source laser is an index guided GaAlAs high power (maximum power 50 mW) laser diode manufactured by Hitachi (Model DL7851G) The laser diode is mounted in an actively temperature stabilized aluminum casing with an antireflection coated molded glass aspheric lens of focal length 8 mm (Thor Labs, Inc. Model C240TM-B) to collimate the elliptical output of the laser. The collimated beam is incident on a gold coated blazed, ruled grating with 1200 lines/mm (Edmund Scientific, Model L43-848)) that diffracts the first order to the feedback mirror. Approximately 15% of the output

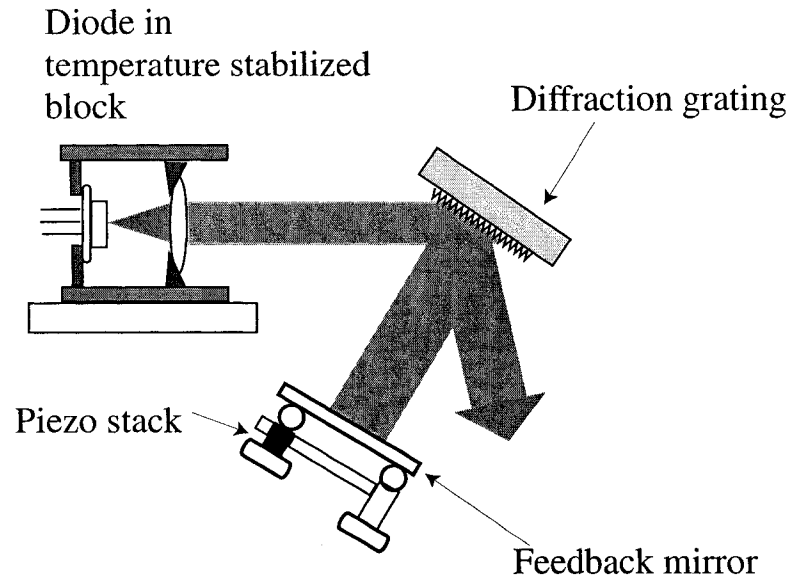


FIG. 12. Schematic of the external cavity diode laser

power is used for active feedback of the laser. The external cavity length is approximately 6 cm. The laser is tuned initially by adjusting its injection current and further tuned by temperature. The Hitachi DL7851G lases at approximately 785 nm at room temperature when injected at 70mA. The diode is cooled  $\approx 5$  degrees Celsius below room temperature using a Peltier thermoelectric heater/cooler. The diode temperature is maintained to within 1 part in  $10^5$  by a feedback loop. The diode temperature, the injection current and the feed back mirror allow for coarse tuning of the laser. The emission wavelength of the laser diode changes with temperature typically by 0.3 nm/K. The change of injection current also changes the emission wavelength of the laser by virtue of change in carrier density [53]. The free running frequency can change as much as 3 MHz/ $\mu$ A and with the external feedback is reduced to  $\sim 0.3$  MHz/ $\mu$ A [54]. The laser is brought close to the wavelength of the required atomic transition by temperature and current tuning. The Piezo-electric transducer (PZT) stack (NEC AE0203D04) attached to the back of the feedback mirror is used to fine tune the laser frequency by adjusting the cavity length. A cavity length (optical path length) variation of  $\Delta L$  yields a relative frequency change inversely proportional to the cavity length,  $\Delta\nu/\nu = -\Delta L/L$ . For a typical drive range of 0-100 V of the PZT, the laser scans  $\approx 2$  GHz. Mode-hop free scans as long as few hundred MHz are easily

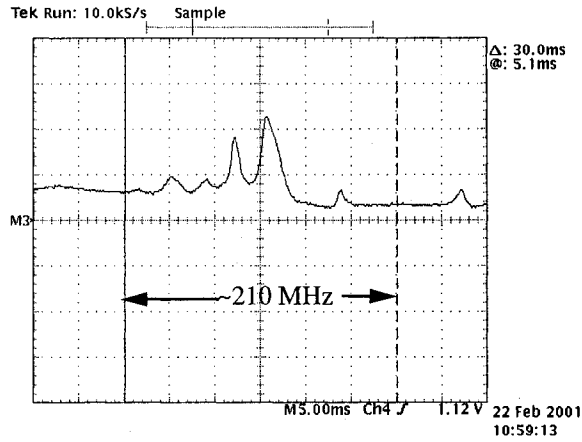


FIG. 13. The oscilloscope scan of the saturated absorption spectrum of the hyperfine components of the  $5s^2S_{1/2} \rightarrow 5p^2P_{3/2}$  transition of  $^{85}\text{Rb}$ , used to lock the trapping laser and for offsetting the probe

achieved.

The free running diode is characterized by a linewidth of several MHz. The fast frequency noise spectrum due to fundamental spontaneous emission events is reduced dramatically by the external feedback. With feedback the noise spectrum is reduced to low frequency noise due to mechanical fluctuations of the external cavity [49]. The linewidth of the laser with the external cavity is estimated to be in the 100 to 1000 KHz range, much smaller than the line width of the atomic transition. The ECDL also offers improved tuning characteristics, in the range of hundreds of MHz free of mode-hops [55]. Longer mode-hop free scanning is possible by appropriate choice of pivot point of the grating or the feedback mirror.

The probe laser frequency is stabilized by locking the ECDL to one of the well defined cross over peaks of the Doppler free saturated absorption spectrum of the  $^{85}\text{Rb}$   $5s^2S_{1/2} \rightarrow 5p^2P_{3/2}$  transition [50, 55]. A scan over the saturated absorption lines of interest is shown in Figure 13. The frequency dependent discrimination signal needed to drive the locking servo loop is derived from a lock-in technique. The laser drive current is modulated at 10 KHz to encode the resonance information to the high frequency region where the noise amplitude that affects the laser stability is less severe. Demodulation provides a derivative-like signal at resonance that is integrated and amplified to drive the PZT. A block diagram showing the stabilization scheme is shown in Figure 14. The stabilized laser output is sent to an acousto-optic

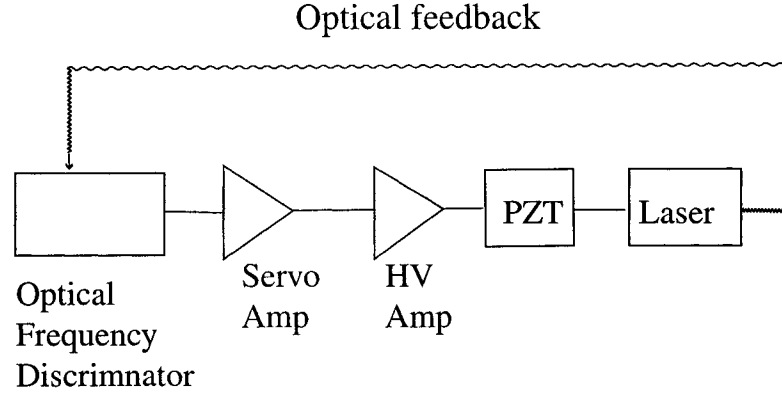


FIG. 14. Block diagram showing the laser stabilization scheme used to lock the probe and trapping lasers

modulator (AOM) (NEC, Model C28217A) to offset the frequency as required. The laser is usually locked to the  $F = 3 \rightarrow F' = 2$ ,  $F = 3 \rightarrow F' = 4$  crossover resonance peak at 92.05 MHz below the  $F = 3 \rightarrow F' = 4$  cycling transition. The AOM can be driven between 75 MHz and 100 MHz, allowing the laser to be tuned several natural widths to the high or low frequency side of resonance as required.

The amount of power available for the experiment is approximately 5 mW and is distributed in several spatial modes. The probe laser is launched into a single mode, polarization preserving fiber. At the expense of losing approximately 25% of the power due to mode mismatch, the fiber provides the flexibility in beam transport and a single, clean Gaussian mode at the output. The fiber output is collimated with a high quality, multi-element, diffraction limited lens of focal length 8.18 mm having a numerical aperture of 0.55 (Newport Model F-L20B). The collimated beam is expanded to  $1/e^2$  diameter of about 8 mm by a Spindler-Hoyer 4X laser beam expander. The collimation of the beam is tested using shear-plate interferometry [56]. The divergence of the expanded beam is close to the diffraction limit of 0.02 mrad. The wave front uniformity estimated from the shear-plate interferometer is less than  $\lambda/4$ . The collimated, expanded beam is directed to the sample through a 12.5 mm thick, 50 mm diameter wedged beam-splitter from CVI Laser, Inc. The 1<sup>0</sup>, wedged beam-splitter is used to eliminate interference between any residual reflections from the surfaces. The beam splitter is anti-reflection coated to minimize reflection at the diode laser wavelength. The residual reflection is less than 0.5%. The beam splitter

TABLE II. The analyzing power of the polarimeter is defined by the extinction ratio,  $I_{\uparrow}/I_{\rightarrow}$  measured by retro-reflecting the probe from a mirror at sample position

Channel	Incident	QW plate	Analyzer	retro-reflected
$l  l$	$\uparrow$	None	$\uparrow$	$I_{\uparrow}$
$l\perp l$	$\uparrow$	None	$\rightarrow$	$I_{\rightarrow} = I_{\uparrow} 6.6 \times 10^{-5}$
$h  h$	$\uparrow$	helicity preserving	$\uparrow$	$I_{\uparrow}$
$h\perp h$	$\uparrow$	helicity non-preserving	$\rightarrow$	$I_{\rightarrow} = I_{\uparrow} 3000$

reflects 35% of the horizontally polarized and 65% of the vertically light incident on its surface. In data analysis this is accounted for in comparison of different polarization channels.

### 3.2.2 Polarization

The polarization of the incident beam is carefully adjusted and measured. The polarimeter is tested in all four polarization channels to determine the fidelity of the polarization measurements. The incident probe beam is initially vertically polarized immediately before the beam splitter by a high quality linear polarizer (Newport Corp, Polarcor<sup>TM</sup>). The combination of the polarization maintaining fiber and the Polarcor<sup>TM</sup> linear polarizer gives an extinction ratio of well over 17,000 for the probe beam before the beamsplitter.

The analyzing power of the polarimeter is measured by retro-reflecting the probe beam by a mirror placed at approximately the position of the sample (just outside the vacuum). The reflected power is measured after the analyzer in the detection arm of the apparatus. The extinction ratio, the ratio of the measured power in the linear and circular channels. The Table II shows the four measurements and the relative intensities in each channel. The retro-reflection is minimum in the two crossed polarization configurations, and maximum in the two parallel configurations. The polarimeter gives an extinction ratio of 15,000 in the linear channel and approximately 3000 in the circular channels.



### 3.2.3 Signal Detection

The angular distribution of the backscattered light reflected by the beamsplitter is recorded on the charge couple device (CCD) camera placed at the focal plane of the field lens (analysis lens) as shown in Figure 11. The CCD camera is a Princeton Instruments (Roper Scientific) LN/CCD, with a Tektronix 512x512 pixel array. Each pixel is square, 24x24 micron in size. The detector can be cooled below  $-100^{\circ}$  Celsius to achieve very low thermal noise, enabling long integration times. Under normal data runs the detector is cooled to a temperature of  $-90 \pm 0.05^{\circ}$  Celsius. The CCD camera is able to accumulate the signal from periods ranging from a few milli-seconds to hundreds of seconds depending on the time scale of motion of the scatterers, and the signal size. The angular response of the detection system is ultimately restricted by the pixel size of the detector, and the focal length of the analysis lens. The focal length of the analysis lens is 450 mm. Thus the diffraction limited minimum instrument resolution is 0.06 mrad ignoring any other effects such as the beam divergence and aberrations due to optics in the collection arm. The lens is placed directly in front of the beam splitter with an aperture stop to remove secondary reflections of the specular beams incident on the beamsplitter. The lens is a high quality 50 mm diameter, corrected, V-coated achromatic doublet. It is possible to place the CCD directly in the focal plane of the analysis lens to record the CBS cone from self averaging samples such as suspensions in liquids or from solids with an appropriate mechanism to achieve configuration averaging.

The collection optics and the experimental protocols are somewhat more complicated in case of atomic samples as the sample in this case is a few million atoms contained (trapped) in a magneto-optical-trap (MOT). The MOT consists of 6 laser beams intersecting at the center of an evacuated chamber where the magnetic field is zero, with a field gradient in the radial direction produced by two coils in anti-Helmholtz configuration. The atoms in the trap laser field absorb and re-emit the trap laser light- the process through which they are Doppler and Syphissus cooled to be trapped in the center. This fluorescence is much brighter than the fluorescence due to the very weak probe, and can easily saturate the CCD in a very short time. The CCD and the trapping lasers need to be synchronized to separate the fluorescence of the atoms excited by trap lasers and those excited by the probe. Therefore the trap lasers are switched off when the atoms are probed for CBS to be observed. The added advantage in doing so is that the probed atoms are not perturbed by

the trapping beams during the CBS cycle. The period of time that the atoms can be released from the trap is limited by the initial trap temperature, the number of probe photons scattered by the atoms and the amount of time that will be required to reconstitute the trap. For a 5 ms trap off time the MOT is allowed to reconstitute over a 20 ms period. For the atoms to move out of resonance or to acquire a Doppler width, comparable to the natural width the atom needs to scatter roughly 1000 photons. At a saturation parameter of 0.08 the on-resonance scattering rate is approximately  $1.6 \times 10^6 \text{ s}^{-1}$ . Thus an atom is forced out of resonance in approximately 1 ms. Therefore the atoms are exposed to the probe for a shorter duration of time, during which the trap lasers are turned off. However the CCD is not capable of being triggered at these time scales and a technique initially used by G. Labeyrie *et. al.* [24] is used with some modifications to synchronize the timing of the data acquisition process. The probe light scattered from the trap is brought to focus at the focal plane of the analysis lens where an optical chopper is placed as shown in Figure 15. With the chopper in place the CCD can be exposed for few minutes at a time with it collecting fluorescence from the atoms during the trap OFF/probe ON phase and blocking the trap fluorescence during the trap ON/probe OFF phase of the cycle. The trap on time is approximately 20 ms and it is off for 5 ms, trap duty cycle is 80%. During the off time the probe is turned on for 0.25 ms, giving a data collection duty cycle of 1%. The timing diagram is shown as shown in Figure 16. The phase of the chopper can be adjusted to eliminate any trap light that might leak through to the detector at the beginning and the end of the exposure period. The Transistor-Transistor-Level (TTL) signals are generated by an analog pulse generator (QuantumComposers, Model 9014) triggered by the phase locked synchronization output, the trigger signal shown in Figure 16, of the chopper controller (New Focus Model 3501). The Trap and the probe control pulses can be delayed relative to the rising edge of the trigger signal as required. Two 50% duty cycle blades are used together to obtain the  $\sim 10\%$  duty cycle for the exposure. With this timing scheme many hundreds of exposures can be made during the time that the CCD mechanical shutter is open for the CCD while it is cooled and temperature stabilized to minimize the readout noise. In a typical data collection run the CCD is kept open for 300 seconds allowing for a full 3 seconds of signal acquisition.

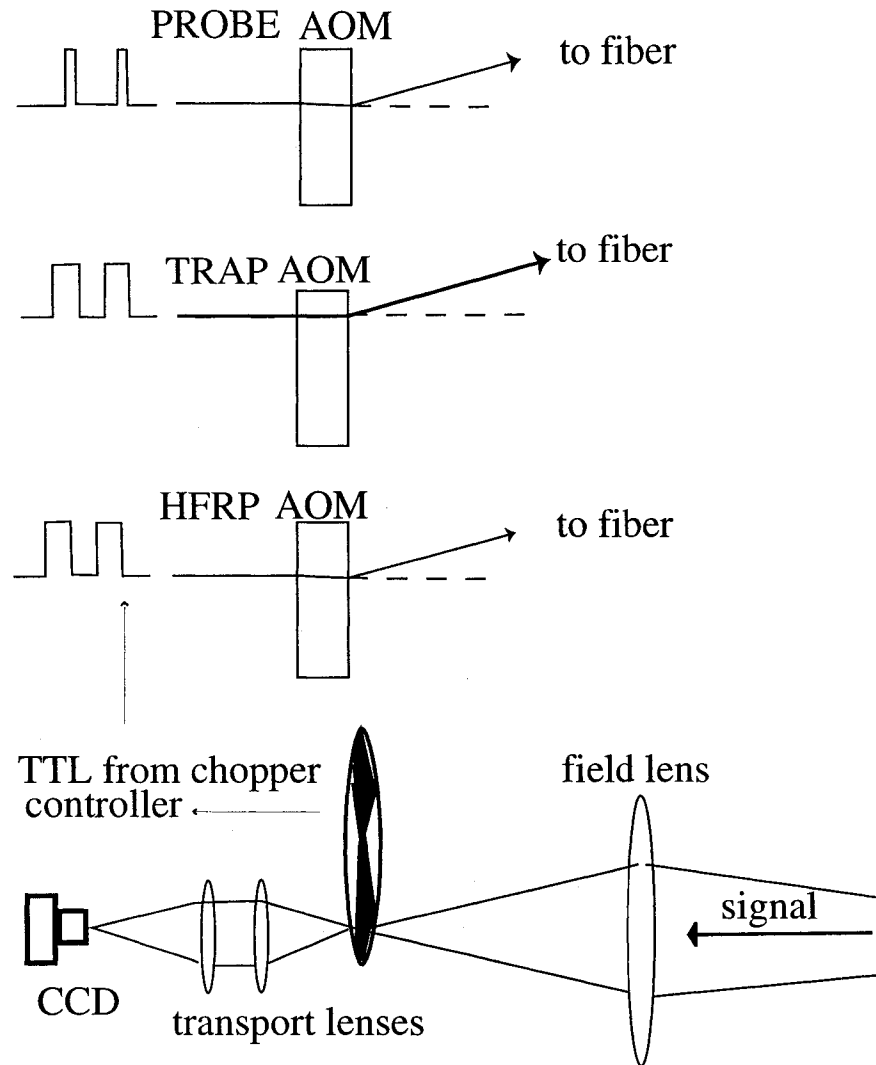


FIG. 15. Block diagram showing the synchronization of the detection phase with the on, off cycle of the trapping, hyperfine re-pumper (HFRP) lasers, and the coherent backscattering probe laser. When the chopper blade is closed the trap laser is ON, probe OFF, and when the blades are open the trap laser is turned OFF, the coherent backscattering laser is turned ON in the middle of the exposure.

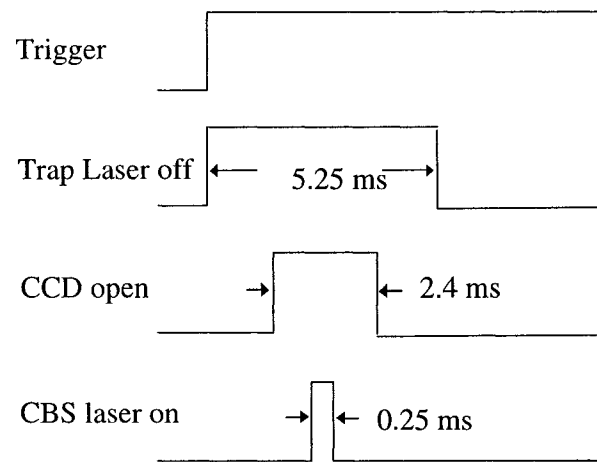


FIG. 16. The timing diagram showing the trap, probe and exposure (CCD open/closed). The trigger signal is derived from the phased locked synchronization signal generated by the chopper.

### 3.2.4 Background Noise

The data collection protocol consists of alternating between a signal acquisition run and a background run. Both these exposures are of equal duration acquired under identical conditions with the exception that the magnetic field of the MOT is turned off for the background acquisition. Unlike for solid samples or suspensions, the background measurement is critical for the observation of CBS from an atomic samples. The background contribution even when the MOT B-field is turned off can arise from the collection of cold atoms due to the increase in density of atoms in velocity space due to the presence of the optical molasses formed by the red detuned trapping beams [40, 24]. Given that timing sequence is identical during the signal and background acquisition, it is assumed that the cold atoms have dispersed between the trap off and probe on time. Thus the true background is assumed to arise from the hot atomic vapor present in the probed volume. The probe beam is highly attenuated by the trap during the signal cycle. This implies that the hot vapor directly behind the cloud is not excited and will not contribute to the background even though this fluorescence is acquired and subtracted during as the background. The error due to this over estimation of the background can be significant, and if not properly accounted for contributes to the systematic error in the experiment. In order to account for over estimating the background the absorption of the entire probe beam is measured during the trap off cycle as a function of the probe detuning, with the probe linearly and circularly polarized. With this absorption curve the background acquired as described earlier, is corrected by accounting for the attenuation of the probe intensity due to the trap. In Figure 17 the total probe attenuation is shown as a function of detuning in each channel.

The unwanted background in the signal is mostly due to stray light scattered from various optical elements and the speckle noise that arises from coherent backscattering from the same. The scattered stray reflections are eliminated by directing the specular reflections away from the collection field lens when possible. The residual speckle depends on the particular polarization channel in which data is acquired. The residual scattering is minimized in the linear perpendicular,  $l \perp l$  and the helicity preserving,  $h \parallel h$  channels as the light reflected (singly scattered light) from various components are nulled by the analyzing linear polarizer in these two detection channels. However in the  $h \parallel h$  channel the 1/4 wave plate (QWP) used to circularized the

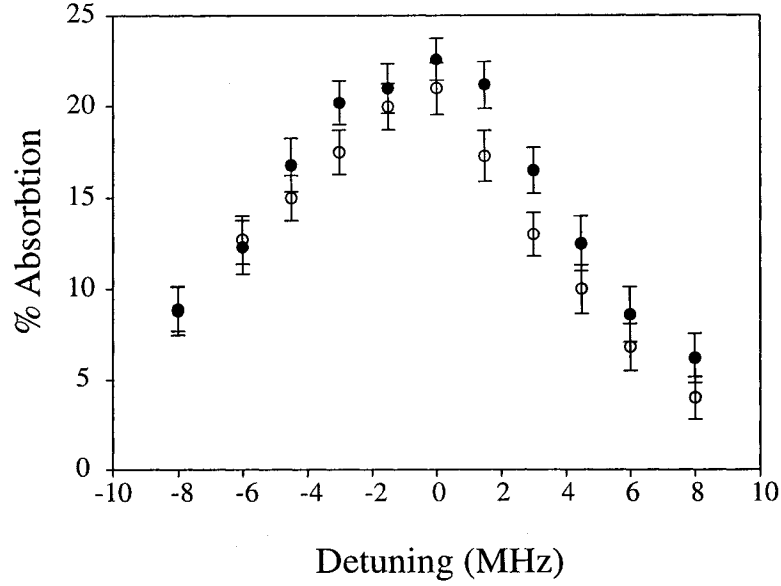


FIG. 17. The attenuation of the probe beam as a function of detuning. The filled circles shows attenuation of linearly polarized light and the open circles the circularly polarized light. The measurement is taken sufficiently far from the trap to avoid collecting trap fluorescence.

linearly polarized probe itself scatters some light and this is not nulled by the analyzer. The analyzer is set to transmit light of the same polarization as the incident light. Therefore the minimum background in other polarization channels is higher than that is obtainable for the  $l \perp l$  channel. Table III shows the relative orientation of the linear polarizers in each channel and the intensity of light retro-reflected by a mirror at the sample position as measured at the detector position. The relative speckle contribution in each polarization channel is also maximum where the retro-reflection is maximum.

It is critical in this experiment to eliminate any stray reflections, to minimize residual beam scattering, and to isolate the detection system from room light in order to detect the very small signals expected from the ultracold  $^{85}\text{Rb}$  atoms. The counting rate for the signal is typically in the region of 100 photons/sec/pixel to 300 photons/sec/pixel depending on the polarization channel and the probe intensity used. A significant background contribution arises from the probe beam reflected from the beam-splitter and the residual of the probe transmitted through the sample, when these are not properly terminated. These beams are terminated at beam

TABLE III. The intensity of speckle formed by light scattered from optical elements in the four polarization channels, shown with the relative orientations of the analyzer with respect to the incident polarization direction.

Channel	Incident	QW plate	Analyzer wrt Incident	Speckle
$l  l$	$\uparrow$	None	$\uparrow$	max
$l\perp l$	$\uparrow$	None	$\rightarrow$	min
$h  h$	$\uparrow$	helicity preserving	$\uparrow$	min
$h\perp h$	$\uparrow$	helicity non-preserving	$\rightarrow$	max

dumps shown in the Figure 11. The beam dumps are 50x50 mm, RG1000, dielectric attenuators (manufactured by Schott Glass), with an attenuation constant of  $10^{-5}$  at 780 nm inserted at Brewster's angle to the beam. In doing so the reflection of the vertically polarized components of the beam (transmitted and reflected at beam-splitter) are minimized (the transmitted beam is circularly polarized when required). Residual reflection from the attenuator is directed to an absorptive material. The fraction of the beam transmitted through the attenuator is directed in to a beam dump made of a 0.5" diameter copper tube with its interior surface painted in flat-black. With this set up, the backscattering of the residual beams is virtually eliminated even at high probe intensities that are not used in this experiment. The entire detection path and associated optics are enclosed in an aluminum casing running from the sample chamber window to the CCD detector. The path between the beam splitter to the CCD with the collection optics is covered by 40 mm diameter aluminum tubing to further isolate the detector from background light. With the detection apparatus isolated the room-light contribution to the noise from the detection solid angle amounts to approximately 10 counts/sec/pixel which is smoothly distributed and consistent and is easily subtracted from the signal. This background is consistent in all four channels showing little or no dependence on the polarization.

A further consideration to background contribution is the interference effects due to internal reflections within various optical components. Most critical in this regard are the sample windows, the beam-splitter, and the vacuum window of the CCD. The point like source from which the backscattered light originates forms uniform narrow fringes at the focal plane-the CCD when it was imaged through the standard uncoated vacuum window of the sample chamber. The fringe contrast in this case was in the

region of 10%, approximately equal to the CBS enhancement of 10-15%. Therefore it was necessary to replace the vacuum chamber window used for CBS imaging with a V-coated wedged window. The 38 mm diameter, 10 mm thick, entrance window with a  $1^\circ$  wedge angle, and the 25.4 mm diameter, 10 mm thick exit window with a  $0.5^\circ$  wedge angle were custom coated for 780 nm at zero incidence (CVI Laser Corporation). The entrance windows were adhered on to and vacuum sealed with an ultra-high vacuum epoxy (Torr Seal, Varian Vacuum Products) on to a 70 mm vacuum flange mounted on a 10 cm bellows. The bellows enables the window to be moved slightly to direct the specular reflection from the front and the back surface away from the backscattering direction. Even with the coating the 0.5% reflection of the probe at the window is large enough to saturate the detector in a short time, and needs to be directed away from the CCD.

### 3.2.5 Instrument Resolution

The absolute resolution limit of the instrument in principle is determined by the focal length of the analysis lens and the pixel size of the CCD detector. Hence the 450 mm focal length of the analysis lens in conjunction with the  $24 \times 24 \mu\text{m}$  pixel dimension gives an angular resolution of 0.06 mrad. However the actual experimentally realizable resolution is limited by such factors as the beam divergence, the aberrations induced by the optics, and the effects due to the the image transport system used. The  $1/e^2$  beam waist,  $w_0$  of the beam is approximately 8 mm. and it is collimated to or near its diffraction limit. The far field angular diameter of a Gaussian,  $\text{TEM}_{00}$  beam is given by  $\lambda/\pi w_0$ , where the the wavelength  $\lambda = 780.2 \text{ nm}$ . The probe beam waist  $w_0 = 8 \text{ mm}$  gives a full diffraction limited divergence of approximately 0.03 mrad which is smaller than the 0.06 mrad resolution of the instrument. The beam collimation is tested by shear plate interferometry to verify that the beam divergence is not in excess of the diffraction limit for a beam of this size as noted in the previous section.

The instrument resolution is also measured by direct observation of the coherent backscattering cone of a sample of  $\text{TiO}_2$  suspended in water at increasingly dilute concentrations. As the volume fraction of the  $\text{TiO}_2$  goes down, the width of the CBS profile is expected to decrease as the width is inversely proportional to the scattering mean free path as given by equation (19). At the limit at which the cone due to a given volume fraction becomes close to or narrower than the angular



response function of the instrument, the measured enhancement will become strongly attenuated (due to the convolution with the instrument response function). At this point the observed cone width can be assumed the smallest possible measurable angular profile or the instrument transfer function. The typical signal obtained from two different concentrations of  $\text{TiO}_2$  is shown in Figure 18. The width of the  $\text{TiO}_2$  cones are plotted as a function of the concentration as shown in Figure 19, and the instrument resolution is obtained by extrapolating this curve to zero volume fraction. The curve is non-linear due to the reduction procedure used. The concentration of  $\text{TiO}_2$  was done by removing a constant volume of the suspension and replacing this volume by water. The measured value for the instrument resolution is  $4 \pm 1$  pixels corresponding to an angular resolution of  $\sim 0.2$  mrad. The actual instrument resolution is a factor of 3 less than what is expected ideally but is sufficiently small to observe a profile as large as 3 to 4 times the demonstrated resolution limit.

### 3.3 SAMPLES

The purpose of this work is primarily concerned with observing coherent backscattering from a dilute gas of atoms. It is however necessary to look at coherent backscattering from classical samples, samples that behave like ideal dipole scatterers to determine the fidelity of the instrument and to ascertain its response prior to investigating either cold or hot atomic gasses. The suspensions and the solid samples are categorized as classical samples, and the atomic samples as non-classical due to the observable effects of the internal structure of these samples on the coherent backscattering signal. In this section the sample preparation is described in detail.

#### 3.3.1 Suspensions and Solids

Coherent backscattering signals are observed from solid samples and suspensions in liquid in all four polarization channels. In the case of suspensions the configuration averaging occurs automatically by virtue of the motion of the scattering particles in the liquid. The time scale of motion of the particles is much longer than the dwell time of the probe photons in the sample which allows the speckle to be completely homogenized into an average diffusive background. The typical exposure time for observation of CBS from a suspension is from 2 s to 10 s depending on the probe

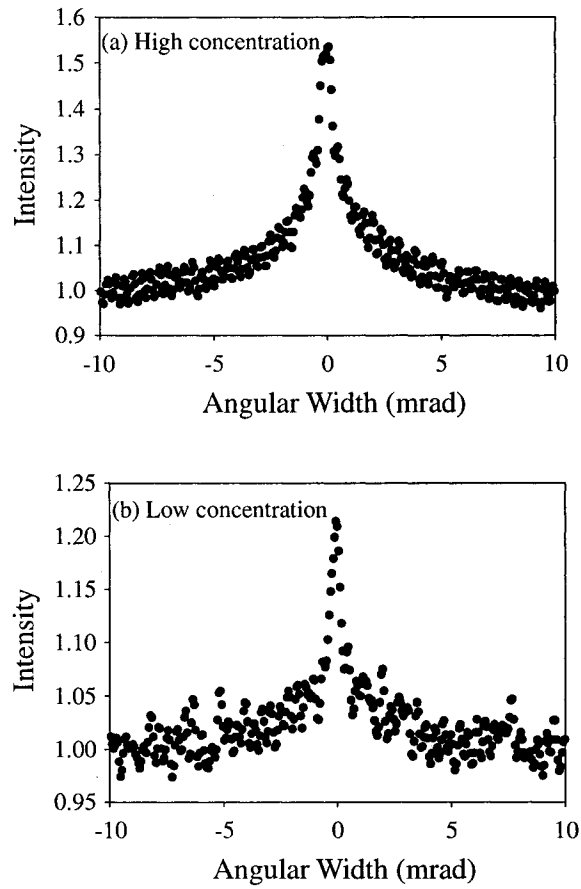


FIG. 18. The horizontal cross section through the center of the coherent backscattering signal from a sample of rutile  $\text{TiO}_2$  consisting of particles on the average of  $\sim 1.2\text{--}1.5\ \mu\text{m}$  suspended in water. (a) Volume fraction-High. (b) Volume fraction-Low.

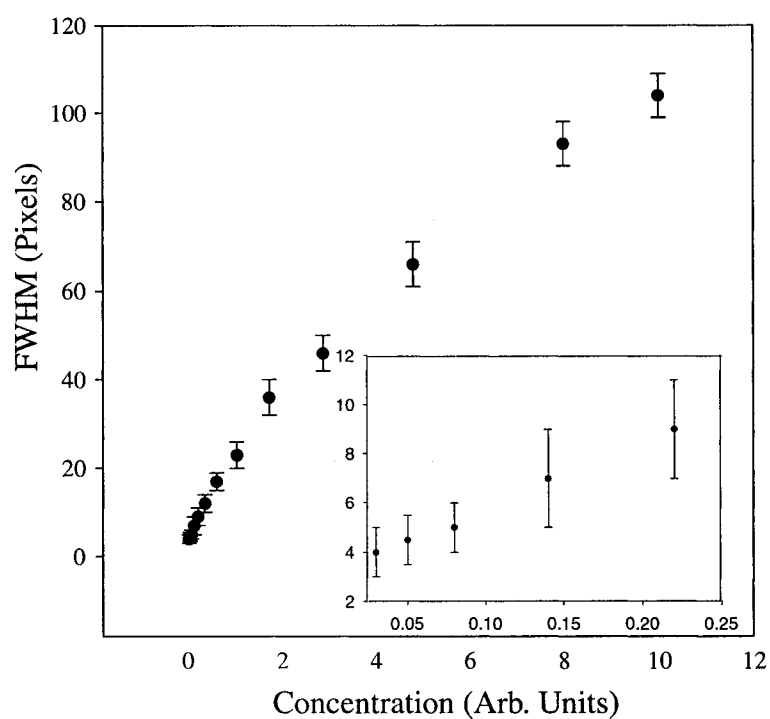


FIG. 19. Plot of full width half maximum (FWHM) of coherent backscattering signal cone profile of rutile  $\text{TiO}_2$  suspended in water as a function of volume fraction. For clarity the curve is expanded to show the behavior at low concentrations in the inset.

power. The maximum enhancement is achieved in the helicity preserving,  $h||h$  channel. A typical coherent backscattering signal from a suspension of  $1.0\ \mu\text{m}$  diameter polymer spheres is shown in Figure 20. The full angular width accessible with the detection system is approximately 27 mrad. The typical cone width at full width half-maximum (FWHM) is in the region of 0.5 mrad to a few milli-radians. The FWHM of the coherent backscattering profile in Figure 20 is approximately 0.5 mrad. The expected enhancement in the  $h||h$  channel is a factor of 2 above the incoherent background. The measured enhancement in this channel is approximately 1.75 times the incoherent background. This discrepancy can be attributed to loss of reciprocity due to the inability to collect all the light scattered from the sample. The suspension is contained in a 15x50x7 mm spectroscopic grade quartz cuvette. The probe beam illuminates a 8 mm diameter region of the cuvette. Due to refraction inside the medium some of the light escapes from outside the region of illumination. In this case it is not possible to satisfy the condition  $I_C = I_L$  given in equation (9) that is required to obtain an enhancement of 2 above the incoherent background. Also it should be noted that the intensity of the beam is not uniform over the region of illumination - it is Gaussian. To realize a factor of two enhancement it is necessary have a beam of uniform intensity relative to the mean free path in the material. An addition requirement is that the multiply scattered photons should be confined to the illuminated region. Those photons that escape from the region outside of the beam waist suspended on the sample, merely contribute to diminish the coherent signal by increasing the incoherent background. The largest enhancement observed was of a small,  $\approx 2\ \text{mm}$  diameter, styrofoam ball. The sample was fixed to a rotor of a small motor by a fine pin to average the speckle. The motor was rotated at approximately 10 revolutions per minute during which the coherent backscattering signal was recorded. An enhancement by a factor of 1.85 above the background was measured. The horizontal cross section of the profile is shown in Figure 21. The measured cone width for styrofoam is about 1 mrad, and is in agreement with previous measurements made in similar material at this wavelength [24]. As the expected width of the coherent backscattering cone of rubidium is in the region of 1 mrad this measurement gives a clear indication of the resolution of the coherent backscattering apparatus. Also measured were coherent backscattering profile of Teflon, milk, sand, white paper, and several samples of  $\text{TiO}_2$  suspended in water at various concentrations and particles sizes to characterize the response of the instrument. The results

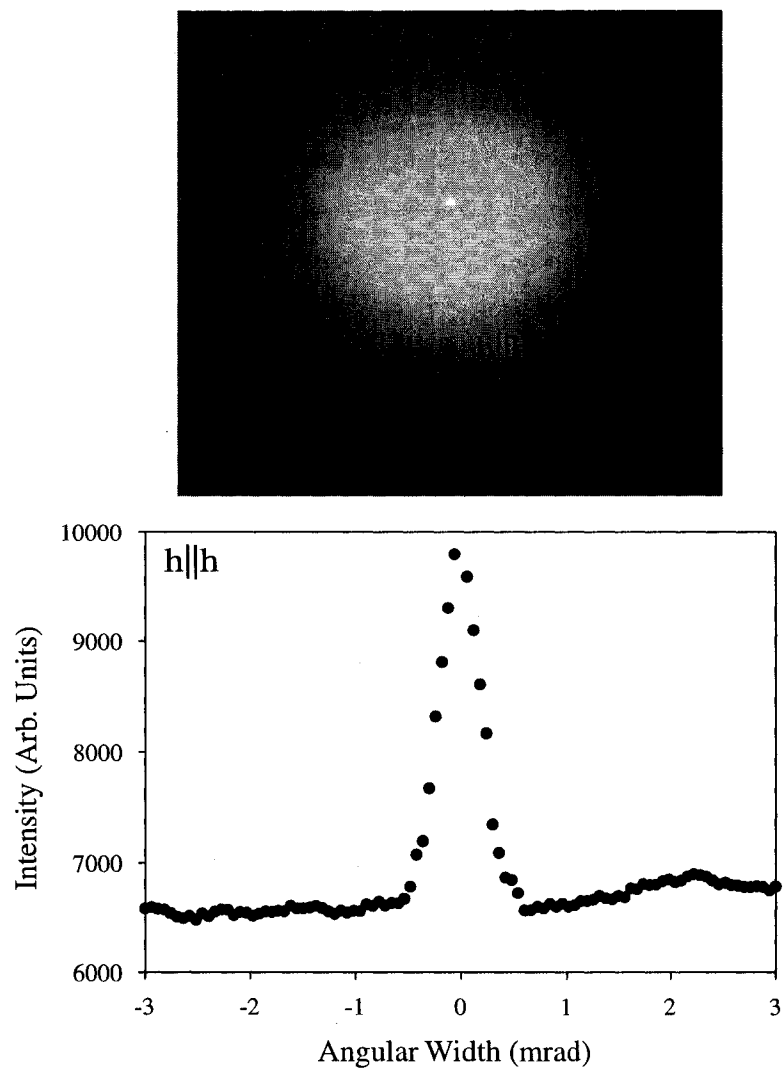


FIG. 20. coherent backscattering signal image of  $1.0 \mu\text{m}$  diameter polymer spheres suspended in water and the horizontal line scan through the intensity maxima, corresponding to  $\theta = 0$ . The full width half maximum of this cone is approximately  $0.5 \text{ mrad}$ .

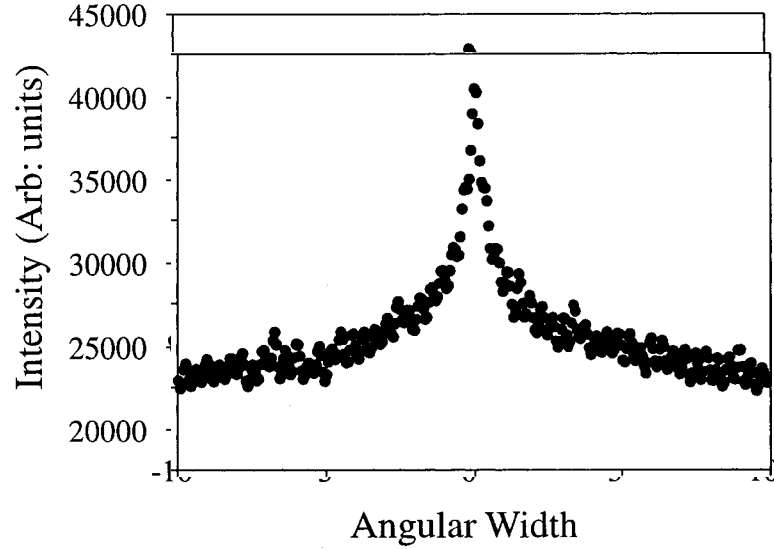


FIG. 21. The horizontal cross section through the center of the coherent backscattering profile of  $\sim 2$  mm diameter styrofoam ball. The cone width is  $1.3 \pm 0.2$  mrad. The speckle was averaged by slowly rotating the sample in the probe beam.

of these measurements are summarized in Table IV.

### 3.3.2 Ultracold $^{85}\text{Rb}$

The sample of ultracold  $^{85}\text{Rb}$  is formed in a standard room temperature vapor loaded magneto-optic trap. The technique of cooling and trapping of neutral atoms is a relatively new area that has seen dramatic developments since the first MOT was demonstrated at AT&T Bell Labs in 1987. For details of practical and theoretical aspects of laser cooling and trapping the reader is referred to the work by S. Chu [17, 18, 19], Cohen-Tannoudji [20], W. Phillips [21], C. Wieman [57], and H. J. Metcalf [40]. The practical and experimental aspects that are important to this work will be discussed here in detail. Critical to the experiment is the temperature of the atoms that are probed and the density of the sample. The condition of reciprocity required for CBS to be observed is dependent on the motion of the scatterers. If the motion of the atoms is fast compared to the time that the wave takes to traverse the sample, the reciprocity will be destroyed. As derived in equation (21) the required temperature for coherent backscattering of resonant light is approximately 0.25 K. Also the sample has to be dense enough, with an optical depth greater than 1, so

TABLE IV. The full width at half maximum (FWHM) and the enhancement values measured for some solids and suspensions.

Sample	Enhancement	FWHM (mrad)
TiO <sub>0</sub> , 10% solution	$1.49 \pm 0.02$	$6.24 \pm 0.3$
styrofoam	$1.85 \pm 0.03$	$1.02 \pm 0.3$
fine grain Sand	$1.69 \pm 0.02$	$1.00 \pm 0.08$
white paper card	$1.59 \pm 0.02$	$7.8 \pm 0.10$

that the probe is multiply scattered.

A schematic of the trap set up is shown in Figure 22. The trap lasers are arranged in the standard configuration of three, retro-reflected beams such that they intersect at the center of a vacuum chamber. A 11 l/s ion pump maintains the pressure in the chamber at or below  $10^{-9}$  Torr. The chamber is equipped with a Ti sublimation pump that is used at times to maintain the low pressure required for a robust trap. The rubidium is contained in a closed nipple attached to an extension 'T' on one of the entrance ports of the chamber. The nipple is isolated from the chamber with a Nupro valve. The rubidium is heated by a heating coil wrapped around the nipple. The temperature of this oven is adjusted by varying the current to the coil. The trap lasers enter the chamber along the x, y, z direction as shown in the Figure 22. The magnetic field lies along the z axis.

Unlike the probe laser, the trapping lasers need to be of high power in order to load as many atoms in the trap as possible. To obtain the high power needed for the trap the diode lasers are used in a master-slave configuration as the power from the master itself is insufficient to achieve the high number density of atoms. The stabilization and locking of the master is similar to that of the probe. The master diode laser is an index guided GaAlAs, Hitachi DL7851G, which is frequency stabilized by locking to a crossover peak of the  $^{85}\text{Rb}$  saturated absorption spectrum as described previously. The locked laser output is sent to a polarizing beam-splitter (PBS) through a half wave plate allowing good control of the reflected and transmitted power. The reflected master beam is sent to the slave diode through a Faraday rotator and a half wave plate as shown in Figure 23. The slave diode is a high power Sanyo DL7140-201 rated at 70 mW (at room temperature, and an operating current of 140 mA). The slave itself does not employ an external cavity, it is injection locked

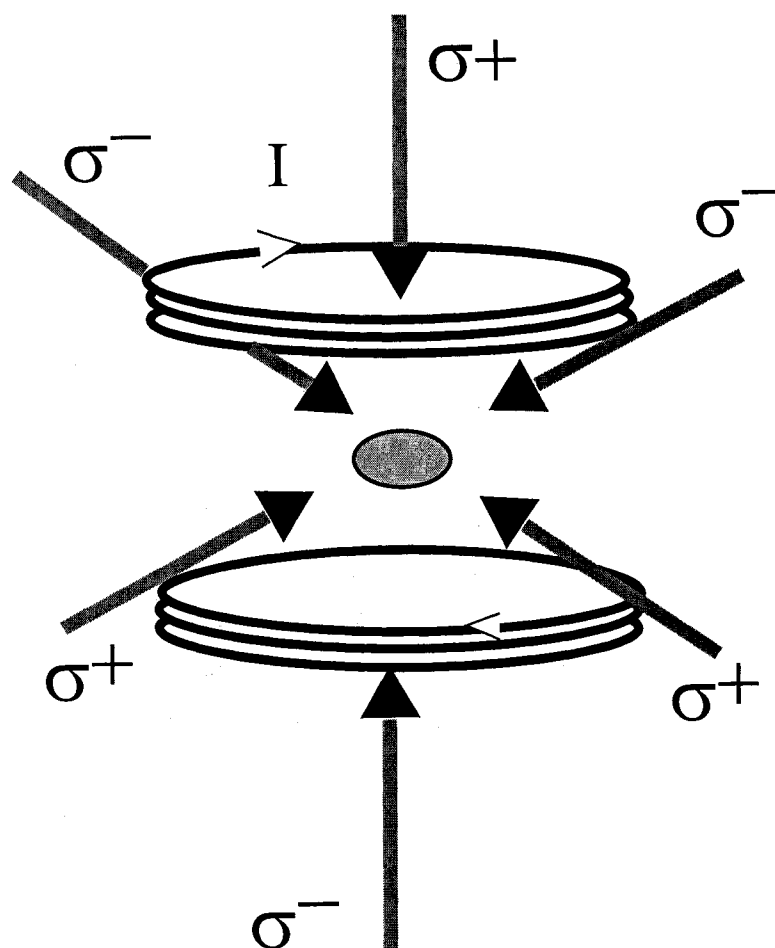


FIG. 22. Schematic of the magneto-optical-trap. Six laser beams intersect at the center of the chamber where the sum of the magnetic fields produced by the two electromagnetic coils is zero.



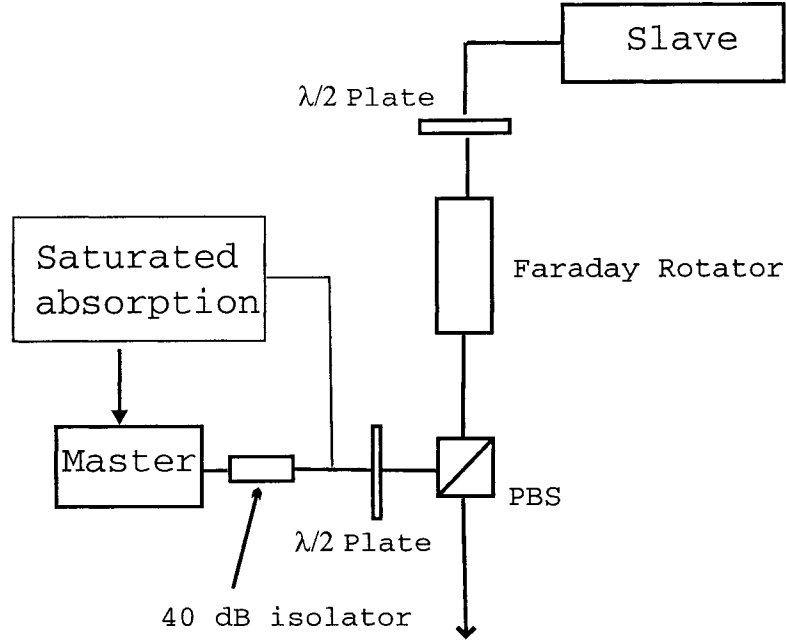


FIG. 23. Schematic of the master-slave configuration used for the trap laser

to the frequency stabilized master laser [58]. This allows the entire power of the slave to be diverted to trapping. If only the master output is used only a small fraction of its power is available for trapping, and some other amplification scheme is needed to obtain a trap with relatively high number density (such as a semiconductor tapered amplifier [59]). The slave is typically run at 65 mA, yielding an output power of 29 mW, with almost all of it being available for trapping. The slave itself is temperature and current stabilized and well collimated. It is well isolated from the outside environment in an aluminium box. The slave is cooled to approximately  $-5$  to  $-7^{\circ}$  Celsius, a lower temperature than the master allowing it to free run close to the required wavelength at a drive current of  $\approx 65$  mA. The slave box is not hermitically sealed, but it is isolated from the surrounding with the beam exit closed with a coated window. To avoid vapor condensation on the diode the box contains desiccant that is regularly refreshed. The atoms excited by the trapping laser has a finite probability of decaying to the lower,  $F = 2$  hyperfine state, about 1 in every 700 excited to the upper  $F = 4$  and become unavailable for trapping. It is necessary to force these atoms back on to the cycling transition,  $F = 3 \rightarrow F' = 4$ . This can be achieved by either a separate laser tuned to  $F = 2 \rightarrow F' = 3$  resonance or by imposing side bands

on the trapping laser, the carrier itself at the energy separation between the two ground hyperfine levels [60]. This is achieved by modulating the drive current of the slave laser at a frequency of 3.04 GHz. These sidebands were obtained by modulating the slave current, leaving the master undisturbed [61]. The microwave modulation of the current was coupled to the diode via a Bias "T" manufactured by Mini-Circuits (Model ZFBT-50). A voltage controlled oscillator (Agilent Model VTO-8240) is used to produce the modulation frequency which is tuned by observing the trap fluorescence. The sideband power realized with this modulation scheme was approximately 2-3% of the carrier power, without any amplification of the microwave. Best modulation depth is realized with careful matching of impedance and taking care of lead lengths, and connectors.

The half wave plate in conjunction with the Faraday rotator and the PBS allows most of the slave power to be utilized for the experiment. This also minimizes the slave feedback to the master. The master is isolated from the slave and any other spurious feedback by an optical isolator having an extinction of approximately 38-40 dB. This allows the master to run smoothly, free of unwanted feedback that may disturb its long term stability.

The slave output frequency strictly follows the master which in turn is locked to the  $F = 3 \rightarrow F' = 2,4$  crossover peak in the saturated absorption spectrum. The slave follows the master oscillating at 92.05 MHz to the red of the cycling transition. This laser is sent through an AOM that is used to shift the wavelength to, or close to resonance as required. Using the AOM the trap was optimized at a detuning of  $-2.7\gamma$ , where  $\gamma = 5.88 \text{ MHz}$  is the natural width of the cycling transition. About 75% of the power of the slave is coupled to the first order of the AOM which is used for trapping. The AOM also allows for efficient switching of the trap laser by controlling the radio frequency (RF) signal to the AOM. The amplified output (RF amplifier-Motorola Model CA2832C) of a voltage controlled oscillator (Mini-Circuits Model ZOS-100) (VCO) is used to drive the AOM. The AOM operating range spans about  $80 \text{ MHz} \pm 20 \text{ MHz}$ . The first order of the AOM output is coupled into a polarization maintaining fiber (Newport, Model F-SPF) with a coupling efficiency of approximately 66%. The total power available for actual trapping is  $11 \pm 0.5 \text{ mW}$ . The trap laser is switched by controlling the RF to the AOM via an RF switch between the VCO and the amplifier. The switch accepts the TTL pulses generated by the pulse generator synchronized to the experiment through the chopper as described before.

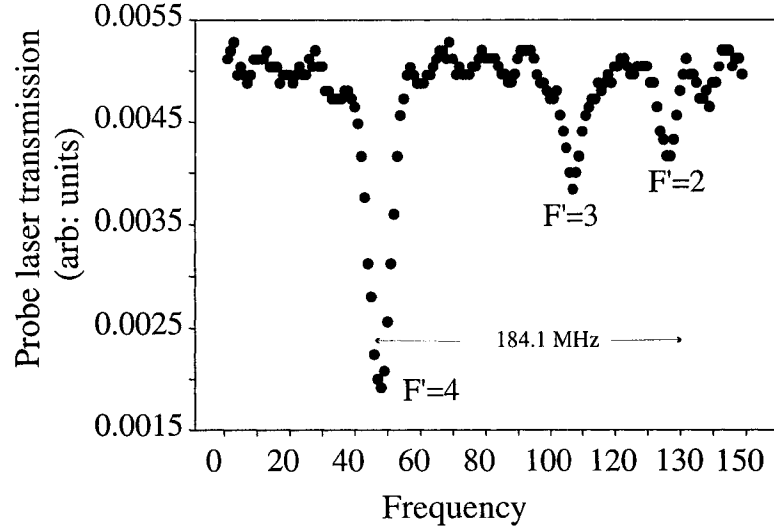


FIG. 24. Absorption profile with the probe scanned over the hyperfine manifold

The trap parameters are optimized by monitoring the trap fluorescence and by measuring the absorption of a weak probe beam transmitted through the center. The absorption measurement is critical to the experiment as it allows us to calculate the true optical depth of the cold atomic cloud. A typical absorption profile is shown in Figure 24 for the probe frequency scanned over the hyperfine manifold. The true absorption is determined at the duty cycle used in the experiment with the probe laser fixed at resonance. However it is difficult to get a true measure of the absorption by measuring at one frequency. Therefore it is measured at several frequencies around resonance and fitted to a Lorentzian (assuming that the laser line width is much smaller than the natural width) to obtain a more realistic number for the optical depth. A time of flight method is used to obtain the temperature of the trapped atoms. The absorption of a weak probe beam is measured at time  $t_0 = 0$  where the trap lasers are turned off. As the absorption is dependent on the propagation length, it is possible to obtain an approximate volume increase of the trap size at  $t_0 + \Delta t$ . The trap temperature calculated from these measurements is  $30 \mu\text{K}$  with an uncertainty of 10% due to the noise in the absorption measurements.

The shape and size of the trap is measured by imaging the trap on to the CCD. The known magnification of the imaging system permits calculation of the vertical and horizontal size of the trap. The trap size was measured at several different

magnetic field values as the magnetic field is a convenient means of changing the trap size and density. The size and shape parameters are important in investigating the dependence of CBS on these values.

In order to avoid systematic errors in the experiment there are several things that need to be considered. These systematics arise from the nature of the sample and how the probe interacts with it. First of all the probe beam needs to be nearly centered on the sample. Any variations in the wave front amplitude across the sample can adversely effect the backscattering enhancement [24]. For this purpose two shim coils are used to move the relatively small sample to the center of the beam. The beam itself is not moved once it is centered on the chamber windows and its angle of attack is optimized to reduce the background due to scattering from various components in its path. When the probe is centered and optimized it is more or less centered on the sample, the cloud of atoms need not be moved more than its diameter to be exactly centered on the beam. The trap can be moved in the vertical  $z$  direction by slightly unbalancing the current in the trapping coils, and horizontally, perpendicular to the probe by a shim coil with its field lying in the  $xy$  plane at 45 degrees to the trapping beams. The centering is easily accomplished by looking at the shadow of the cloud in the probe and moving the shadow by adjusting the field currents. It is critical that the coherent backscattering laser does not disturb the cloud of atoms significantly during the data acquisition cycle. The coherent backscattering line shape for small samples depend on the optical depth [24], the size of the sample [1], and on the motion of the atom in the sample [24]. The probe laser if allowed can induce a large acceleration on the trapped atoms. The high saturation acceleration of  $\sim 10^5 \text{m/s}^2$ , imposes constraints on the power of the probe, and the length of time that it can be allowed to interact with the sample. During a typical data cycle the probe is switched on for 0.25 ms, at a saturation parameter of 0.08 limiting the maximum displacement and velocity of the atoms while maintaining reasonable counting rate.

## CHAPTER 4

### RESULTS AND ANALYSIS

#### 4.1 COHERENT BACKSCATTERING ENHANCEMENT

Images of the spatial distribution of backscattered light in the four standard polarization channels and for resonant excitation on the  $F = 3 \rightarrow F' = 4$  hyperfine transition are shown in Figure 25. With reference to the figure, and as discussed earlier, these channels are customarily labelled as (a)  $l||l$ , (b)  $l\perp l$ , (c)  $h||h$ , and (d)  $h\perp h$ . The images are color coded to indicate by the lightest colors the regions of peak intensity, which are evident in the figure. The region of peak intensity is customarily called the cone, even though line scans through the angular distribution are more nearly Lorentzian than conical, and do not show the cusp-shaped peak characteristic of coherent backscattering from a semi-infinite medium. This is not due to the finite spatial resolution of the instrumentation, but instead due to very long multiple scattering paths necessary to generate the sharp conical spatial feature [33]. Each of the CBS images in Figure 25 corresponds to an average intensity of several thousand counts per pixel accumulated as described previously. The false color intensity scale in Figure 25 has been enhanced to bring out features associated with the cone region. However this also brings out residual speckle noise present in three of the four polarization channels due to stray light scattered from instrumental elements, including the quarter wave plate used in the helicity channels. Slight variations in the configuration of the experimental apparatus during the course of data taking and background subtraction leads to residual speckle that is not completely eliminated by background subtraction. The speckle is almost entirely absent in the  $l\perp l$  channel due to suppression of speckle through cross polarization (see Table III), and due to the absence of the  $1/4 \lambda$  wave plate in the detection path. In spite of the noise, the spatial asymmetries present in the linear polarization channels are clearly evident in the images in Figure 25. These include the greater cone width in the vertical direction for the  $l||l$  channel, and the lines of symmetry along the bisectors of the incident and detected linear polarization directions in the  $l\perp l$  channel. Each of these is discussed further below.

To illustrate the cone profile, we present in Figure 26 line scans of the spatial intensity distribution through the center of the cone for the  $l||l$ , and  $l\perp l$  channels.

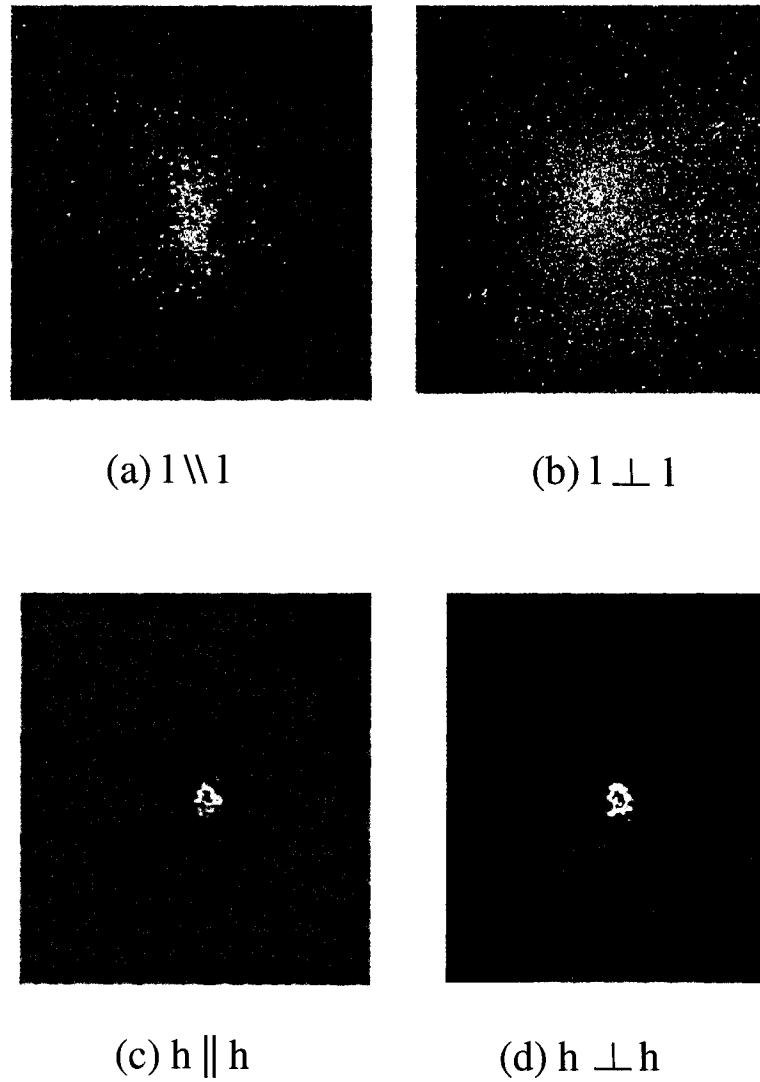


FIG. 25. The charge couple device (CCD) camera images of the coherent backscattering cone in all four channels. Images are color enhanced for clarity

TABLE V. The measured full width at half maximum and the enhancement on resonance in the four polarization channels

Channel	Enhancement	FWHM (mrad)
$l  l$	$1.15 \pm 0.08$	$0.96 \pm 0.18$
$l\perp l$	$1.10 \pm 0.02$	$1.42 \pm 0.06$
$h  h$	$1.08 \pm 0.02$	$1.18 \pm 0.08$
$h\perp h$	$1.11 \pm 0.02$	$1.86 \pm 0.10$

The on resonance coherent backscattering profiles in the helicity channels are shown in Figure 27. In the final quantitative data analysis the enhancements and the cone widths are extracted by angular integration of the intensity profile about the incident wave vector, of the corresponding data in Figure 25. The integrated profile is scanned and fitted to a linear sum of Lorentzians to extract the enhancement and the full width half maximum (FWHM) of the profiles. This angular integration significantly improves the signal to noise ratio for the wings of the cone, but does little to improve the determination of the peak intensity at the center of the cone. The integrated profiles of the on-resonance cones are shown in Figure 28. For excitation and detection of light of definite helicity, the intensity is not expected to depend on the angular displacement around the direction of the incident wave vector. For the line scans shown in Figures 27, the data was not integrated; as seen from the line scans the cones have an angular width of about 1 mrad, and enhancements that are typically less than 15%. The estimated cone width and the enhancement at resonance is summarized in Table V.

The data shows good agreement with the quantum Monte-Carlo simulations; in Figure 29(a) and 29(b), the experimental results are shown with the results of the simulation of the helicity channels [1]. Figure 30(a), 30(b) shows the same for the linear channels. The simulations are done for conditions closely resembling those in the experiments. In particular, an asymmetric Gaussian atom distribution with Gaussian dispersions of 0.55 mm and 0.69 mm and with a maximum optical depth of 5 are selected for the simulation. The multiple scattering simulations are done for weak incident fields, where saturation and correlation are negligible. Scattering orders of more than 10 are necessary to obtain convergence of the width and the enhancement. Figure 31 shows the convergence of the enhancement as a function

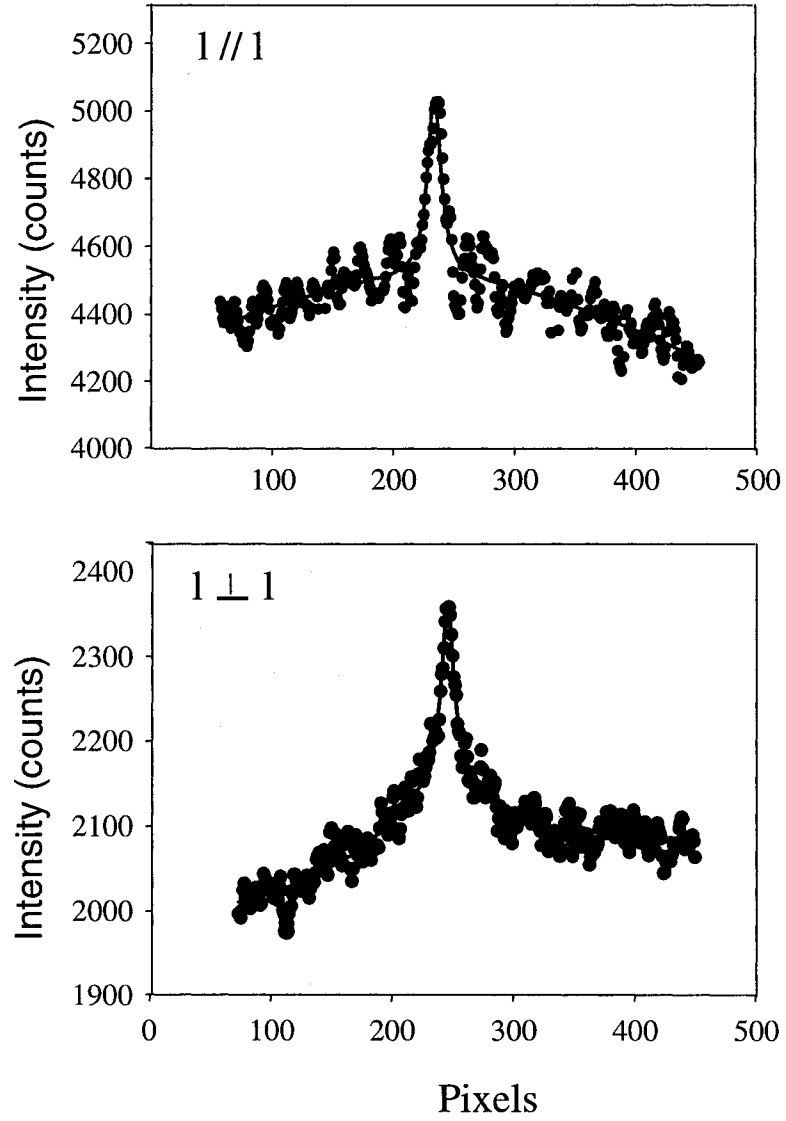


FIG. 26. The coherent backscattering profile at resonance in the  $l // l$ , and  $l \perp l$  channels, the solid line is a Lorentzian fit to the data.



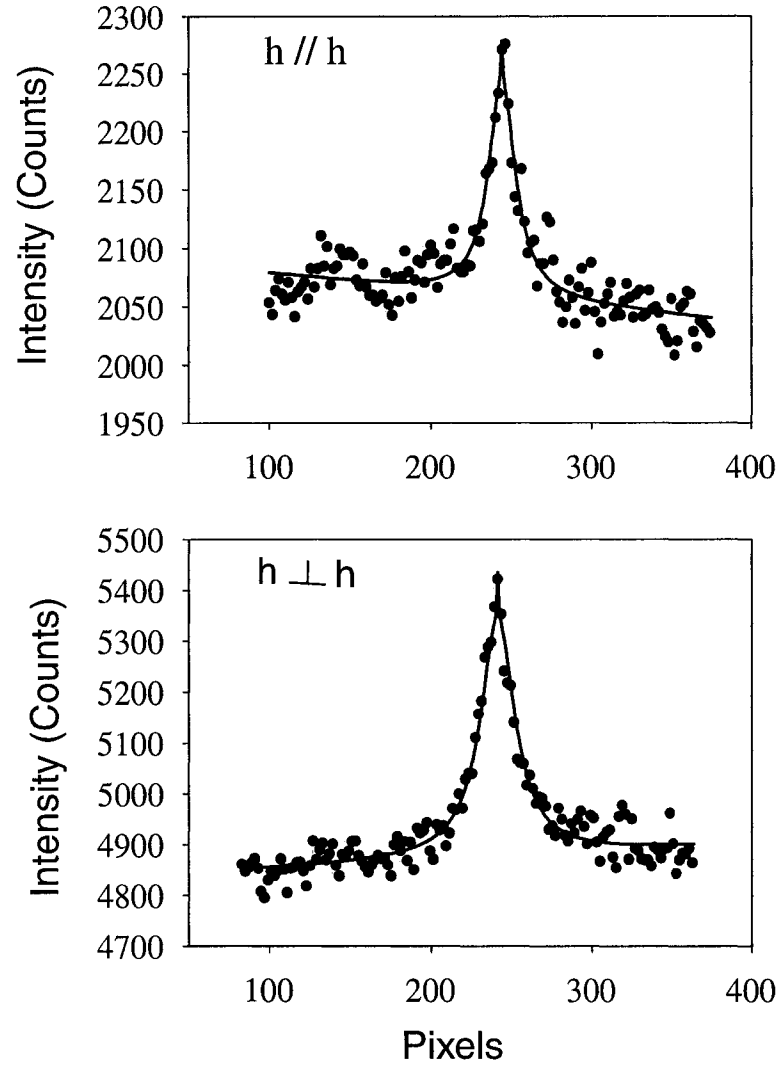


FIG. 27. The coherent backscattering profile at resonance in the  $h \parallel h$ , and  $h \perp h$  channels, the solid line is a Lorentzian fit.

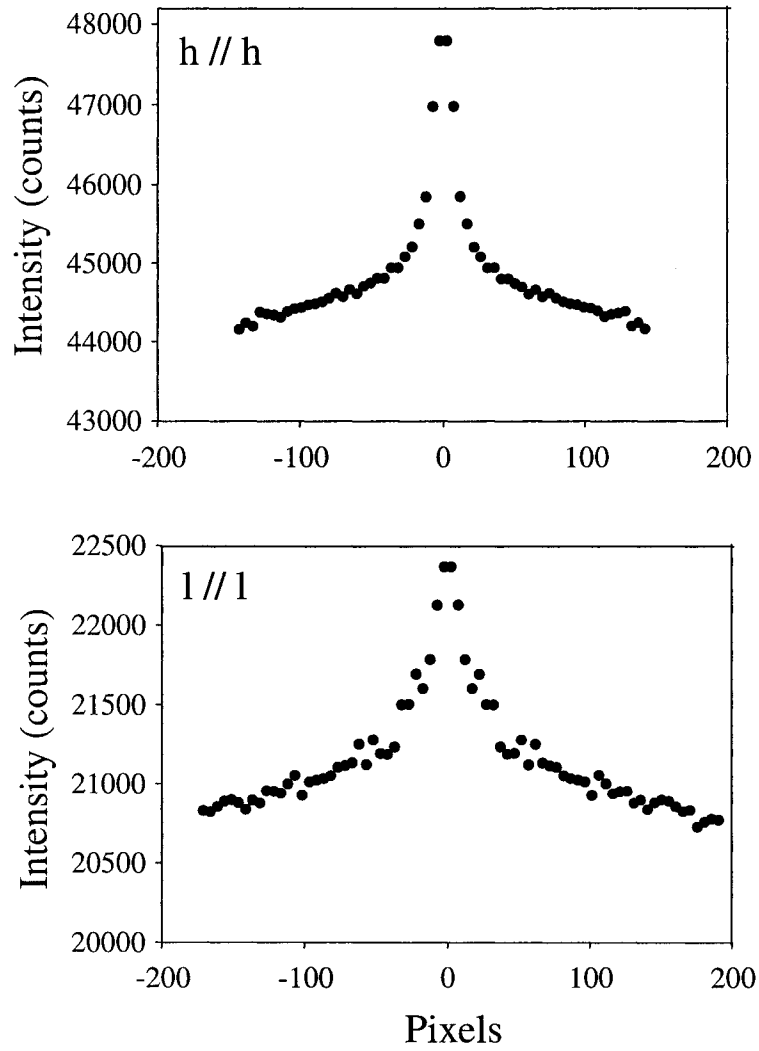


FIG. 28. The on resonance, angular integrated coherent back scattering profile of the  $h//h$  channel, and the  $l//l$  channel.

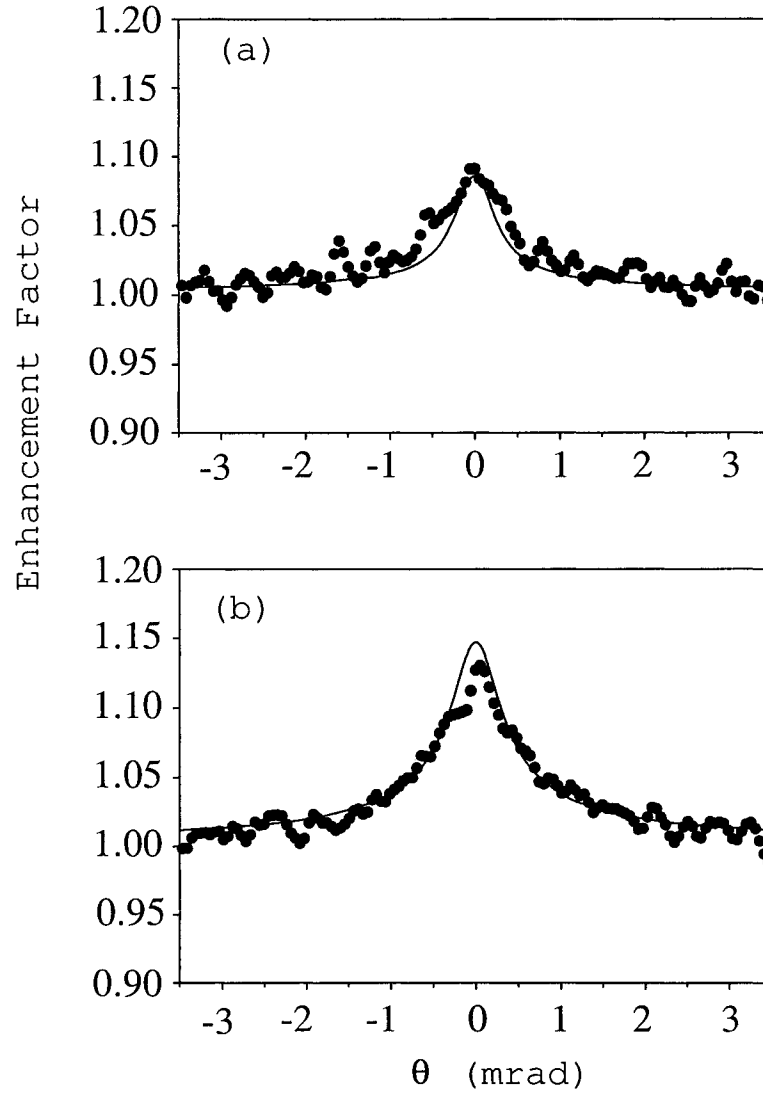


FIG. 29. The experimental coherent backscattering profiles in the helicity channels shown with the quantum Monte-Carlo simulation results. Graph (a) is the horizontal scan of the  $h_{\parallel}h$  profile, and graph (b) is the horizontal scan of the  $h_{\perp}h$  profile [1].

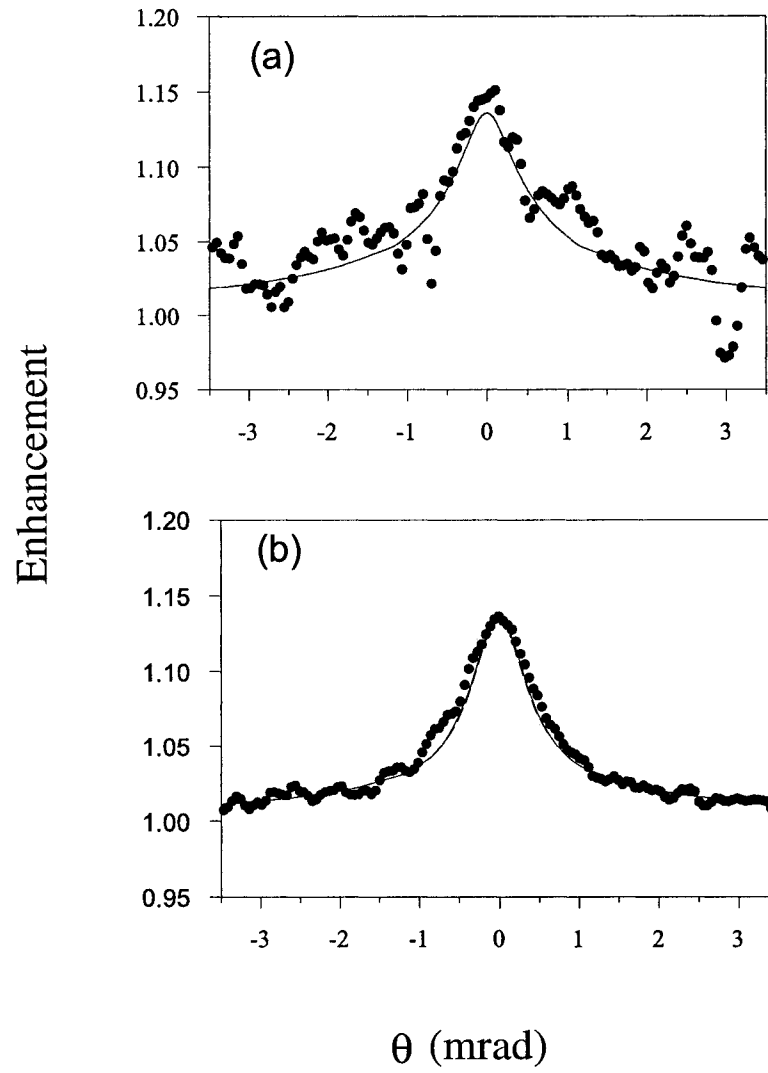


FIG. 30. The experimental coherent backscattering profiles in the linear channels shown with the quantum Monte-Carlo simulation results. Graph (a) is the horizontal scan of the  $l||l$  profile, and graph (b) is the horizontal scan of the  $l\perp l$  profile [1].

of scattering order [1]. In comparing the experimental results with the simulations, there are two general elements to consider. The first of these is the enhancement, which is quite sensitive to the polarization channel, and increases weakly with density at fixed sample dimensions. The width of the cone, on the other hand, is strongly dependent on the size of the sample, with the width increasing nearly linearly with the inverse size of the sample as shown in Figure 32 [1]. Qualitatively, this is because the cone width is sensitive to the average location of the first and last scatterers associated with reciprocal paths, in the same way that the fringe frequency in a double slit is sensitive to the slit separation. To obtain the very good agreement with the theory as seen in Figure 33, and in comparisons to follow, it was necessary to have careful measurements of the MOT size and approximate measures of its shape. The MOT size measurements were made as described in the experimental section by imaging the MOT with a well characterized optical system. The quantitative agreement between the experiment and the simulations shows that such measurements can lead to inference of the average sample size from the coherent backscattering measurements.

Presented in Figure 34 are scans in both the vertical and horizontal directions for the two linear polarization channels. For the  $l||l$  polarization channel, the cone spatial line shape does not generally possess axial symmetry about the direction of the incident wave vector. Shown in the figure are both the horizontal and the vertical scans across the cone, where a horizontal scan corresponds to a direction perpendicular to both the incident wave vector and the direction of the incident electric field vector. In spite of the speckle noise in the data, the spatial asymmetry is clearly seen in the  $l||l$  channel, with the cone width is approximately two times wider for a vertical scan than for a horizontal scan. A physical reason for this is that the scattering of linearly polarized light on the  $F = 3 \rightarrow F' = 4$  transition is strongly directed perpendicular to the direction of the incident polarization (see Figure 4), as expected for electric dipole radiation from an aligned system. Multiple scattering magnifies this propensity, and makes the multiple scattering strongly localized in a horizontal plane. Thus the first and last scatterers in a multiple scattering sequence lie to a good approximation along lines perpendicular to the incident polarization direction, and the phase associated with the detected light will vary relatively rapidly in that direction. However, the phase will vary much more slowly in the vertical direction, in direct analogy to the interference fringes formed from a horizontal double

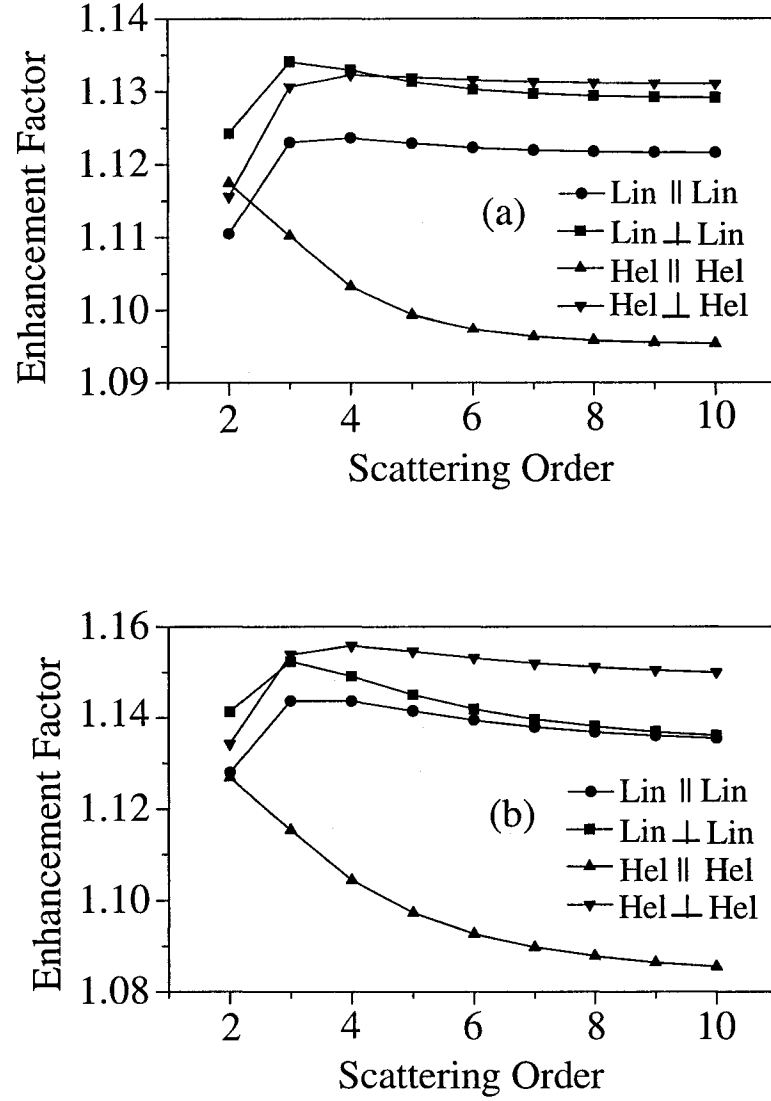


FIG. 31. Dependence of the coherent backscattering enhancement on the scattering order calculated for the  $F = 3 \rightarrow F' = 4$  hyperfine transition in  $^{85}\text{Rb}$  for a Gaussian type atomic cloud of  $r_0 = 1 \text{ mm}$  for tow densities, (a)  $n_0 = 8 \cdot 10^9 \text{ cm}^{-3}$ , and (b)  $n_0 = 16 \cdot 10^9 \text{ cm}^{-3}$ . Individual curves represent different polarizations channels [1].

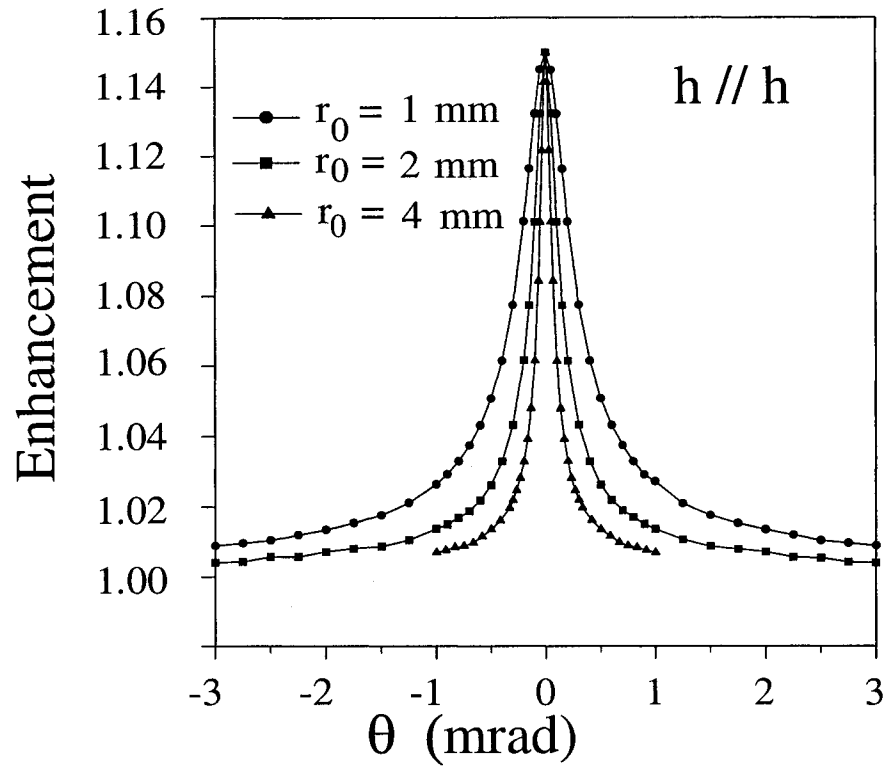


FIG. 32. Dependence of the coherent backscattering enhancement on the sample size - theoretical prediction [1]

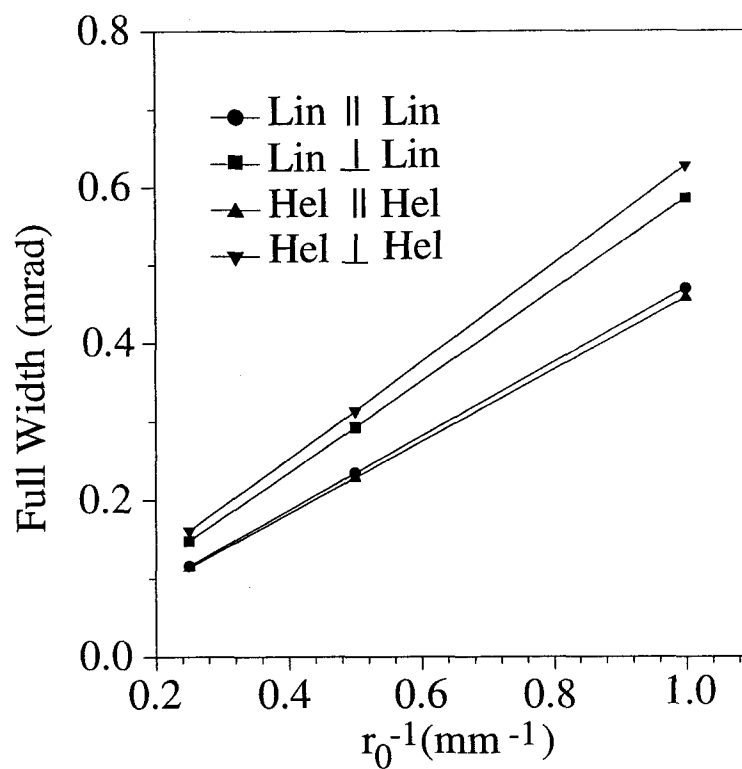


FIG. 33. Dependence of the full width half maximum of the cone profile on the sample size. The optical depth for these calculations were fixed at 5 [1].



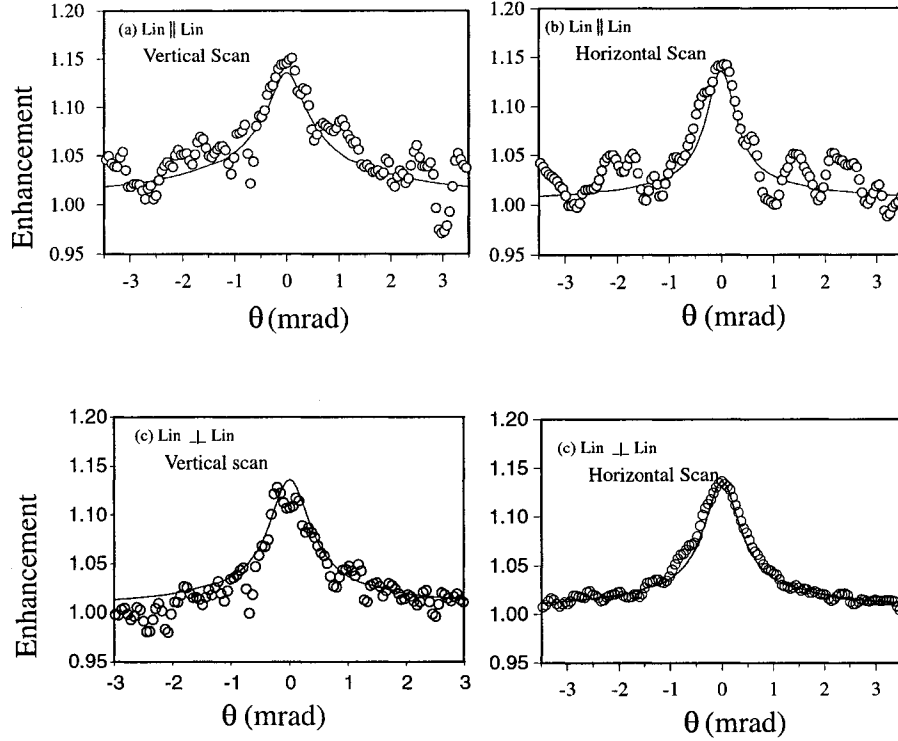


FIG. 34. The experimental coherent backscattering profiles in the linear channels shown with the quantum Monte-Carlo simulation results. Graph (a) is the vertical scan of the  $l||l$  profile, graph (b) is the horizontal scan of the same linear profile, and (c) is the horizontal scan of the  $l\perp l$  profile, and (d) is the vertical scan of the same. The solid line is the theoretically predicted value, the open circles represent the experimental values [1].

slit. Therefore the resulting cone will be significantly wider in the vertical direction. As shown by the solid lines in Figure 34, this behavior is again in very good agreement with theoretical simulations. For the  $l\perp l$  polarization channel, there is a related symmetry, but one that does not arise directly from the angular distribution in single scattering of light linearly polarized perpendicular to the incident light, as this distribution is necessarily isotropic. Instead it comes from the component of light perpendicular to the incident polarization generated by solely multiple scattering. As may be readily seen for linearly polarized light exciting an array of classical oscillators, this contribution to the scattering has a maximum contribution in directions bisecting the horizontal and vertical directions, as recently demonstrated in coherent backscattering experiments in ultracold strontium atoms [62]. The data shows an interferometric enhancement on the order of 1.15 (15%), relative to the incoherent background, for all four polarization channels. This enhancement should be compared with what is expected, and seen for coherent backscattering from classical scatterers, including light scattered from ultracold Sr atoms on the  $^1S_0 \rightarrow ^1P_1$  resonance transition. In the helicity preserving  $h\parallel h$  channel, where single scattering is absent, direct comparison with the above two cases imply an enhancement of 2 above the incoherent background. It was first discovered by Labeyrie, et al. [23] that the enhancement in ultracold Rb is significantly less than this. Generally, the physical origin in the present case lies in the internal atomic hyperfine structure, which permits elastic Raman transitions as well as Rayleigh scattering of monochromatic light from the atoms. As discussed by Müller, et al, it is atomic transitions to a distribution of magnetic sublevels along a multiple scattering path that leads to an imbalance in the direct and reversed scattering amplitudes, and thus to a reduction in the overall enhancement [63].

## 4.2 SPECTRAL DEPENDENCE OF THE ENHANCEMENT

A goal of this research was also to investigate the spectral dependence of the coherent backscattering cone in the four polarization channels. The spectral dependence of the total backscattering cross section centered around  $\theta = 0$  was measured in each one of the polarization channels as a large fraction of this signal corresponds to the incoherent background. Naively one would expect the total backscattered intensity spectra to be approximately equal to the natural width of the transition, considering that the scattering medium to have no temperature dependent (ultra cold sample),

or pressure dependent (low pressure vapor), broadening mechanism. The spectral variation of the relative total intensity of light backscattered into a 20 mrad x 20 mrad cross-section centered on the cone region around  $\theta = 0$  was measured. This quantity depends very weakly on interference effects in radiative transport, for the majority of the signal corresponds to the incoherent (speckle averaged) background. The data, corresponding to the two helicity polarization channels, is shown in Figure 35. There it is seen that the spectral width is several times the natural width associated with single scattering. It is assumed that this is a result of the considerably large optical thickness of the vapor; even when the coherent backscattering laser is spectrally detuned by an amount larger than the natural width, the light penetrates further into the sample but is still scattered and can contribute to the intensity emitted from the sample. It is only when the detuning is so large that the optical depth becomes significantly less than unity, that the scattering line shape will reduce to that of single scattering. This broadening may alternately be related to the increase of the width of the absorption profile in forward scattered light, and may be similarly modelled to obtain the qualitative effect. Also shown in Figure 35 is the result of simulations of the spectral behavior in backscattering from sample of optical depth at 5 and 10 [1, 25]. The overall agreement between experiment and theory is seen to be very good, but suggestive that the true optical depth in the experiments may be somewhat larger than 6 as measured by absorption.

In Figures 36(a), (b), and Figure 37(a), (b) the experimentally obtained enhancement at probe detunings in the range  $-\gamma$  to  $+\gamma$  is shown for the two linear and circular channels respectively. The enhancement is calculated from the Lorentzian fit parameters to the raw data. The error depends on the number of counts and the fit statistics. As the detuning is increased the laser power is increased to compensate for reduced scattering cross section. This increase in probe intensity contributes to larger error bars at high detuning due to the increased background from scattering at windows, and other optical elements along the path of the probe. The error is generally larger in the channels where the speckle is not suppressed, such as in the  $l||l$  and the  $h\perp h$  channel.

In Figure 36(a), it can be clearly seen that the enhancement is suppressed at and around resonance. This behavior is only observed in the  $h||h$  channel and as seen experimentally (Figure 36(a)) and in simulations. This behavior is attributed to a possible interference with the off-resonant levels in the hyperfine manifold. In

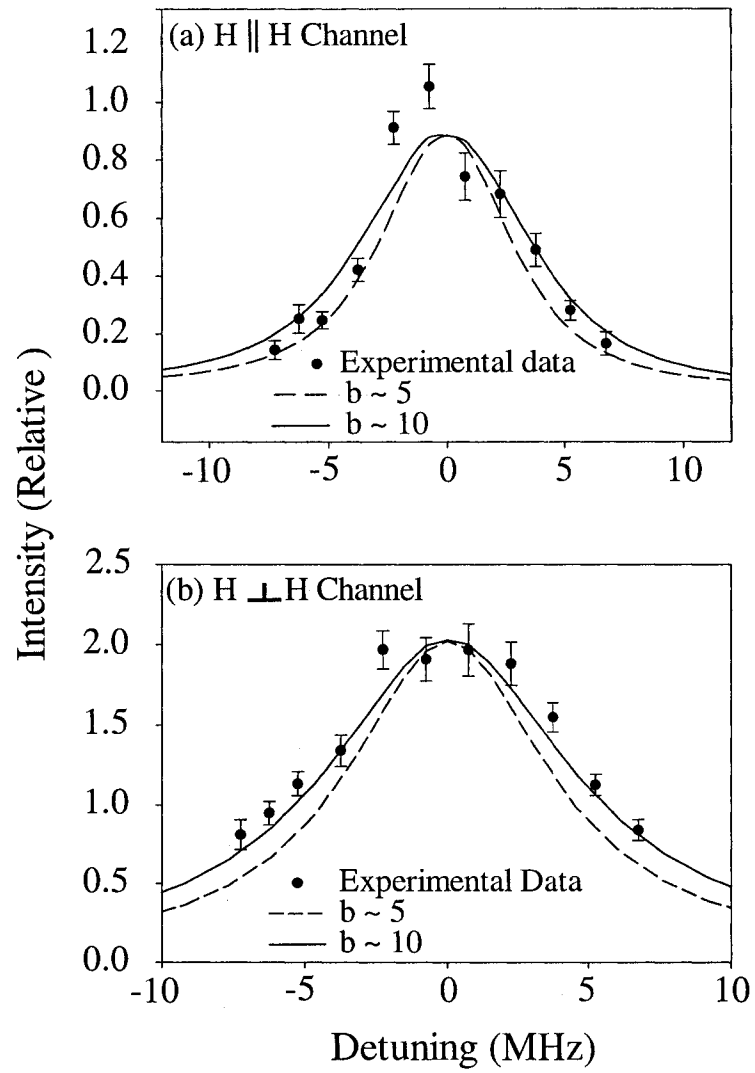


FIG. 35. Detuning dependence of the total backscattered intensity, theory and experiment. Theoretical curves are for two different optical depths,  $b \approx 5$  and  $b \approx 10$  [1].

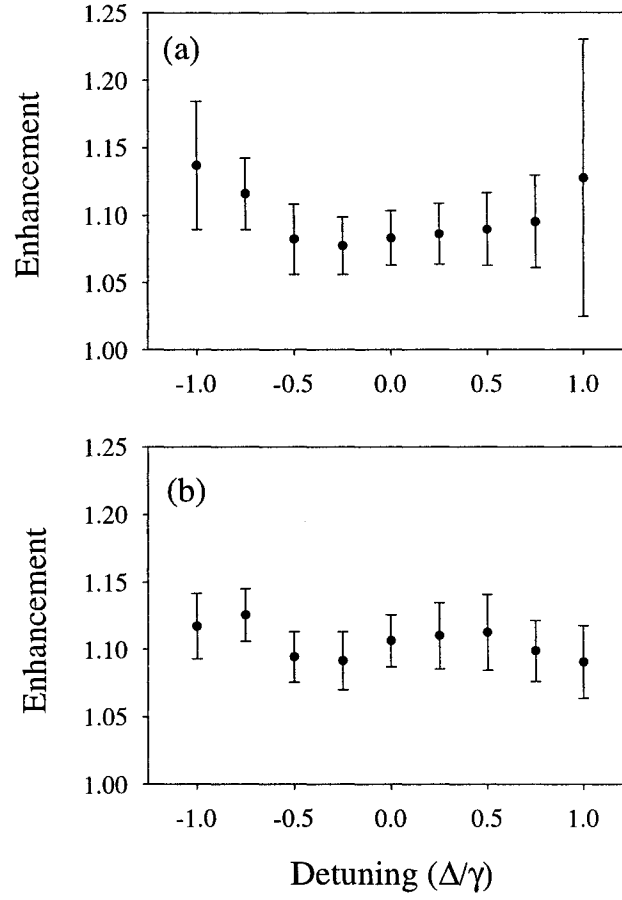


FIG. 36. The spectral dependence of the coherent backscattering profile relative to incident light detuning in (a) the helicity preserving,  $h||h$  channel and (b) the helicity non-preserving,  $h\perp h$  channel.

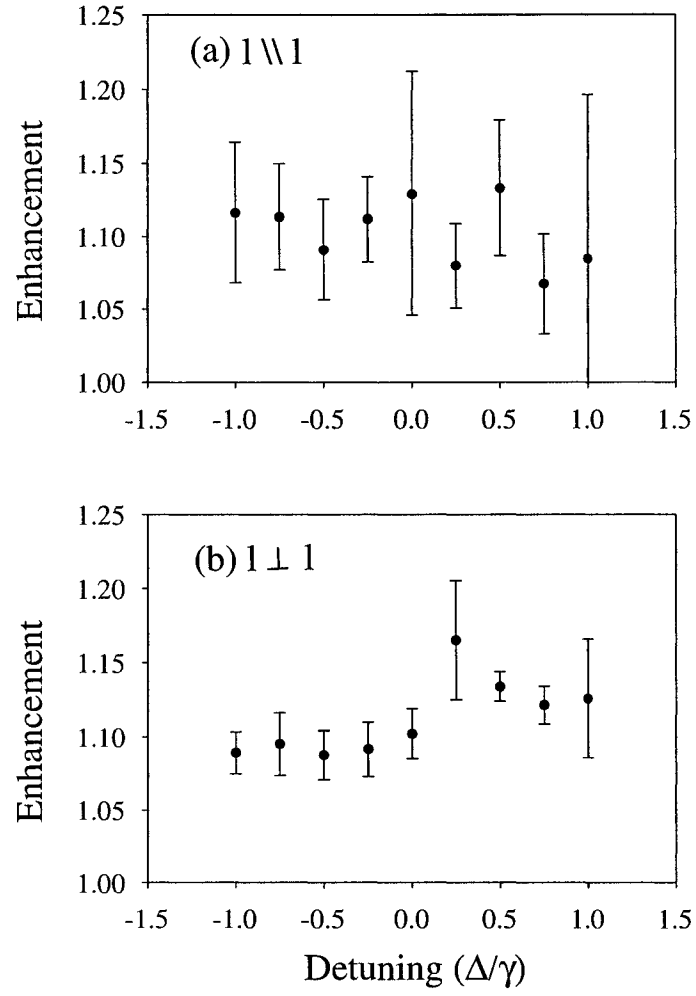


FIG. 37. The spectral dependence of the coherent backscattering profile relative to incident light detuning in (a) the linear parallel,  $l \parallel l$  and in (b) the linear perpendicular,  $l \perp l$  channels.

this case the off-resonant level of interest is the  $F = 3 \rightarrow F' = 3$  transition at 120.7 MHz from the on-resonance cycling transition. The results of the quantum Monte-Carlo calculations too clearly show this behavior in the  $h||h$  channel as shown in Figure 38. The simulations in the absence of the off-resonant levels failed to suppress the enhancement but is clearly present when these were accounted for. At larger atomic density the suppression is further enhanced as shown in Figure 38(b). It is not known as yet why this effect is observed in this particular channel. As shown in Figures 39(a) and (b), the linear channels do not seem to show this effect and as can be verified experimentally with this data as presented in Figure 37(a), 37(b) any obvious suppression of enhancement is not observed.

The interference effect can be explained somewhat heuristically by considering the following expression for the single atom scattering amplitude,

$$A = \frac{C_1}{(\omega - \omega_{34} - i\gamma/2)} + \frac{C_2}{(\omega - \omega_{33} - i\gamma/2)}. \quad (48)$$

Here  $\omega$  is the laser frequency, and  $\omega_{34}$ ,  $\omega_{33}$  are the  $F = 3 \rightarrow F' = 3, 4$  transition frequencies. For single scattering the intensity is proportional to  $|A|^2$ , giving the intensity a direct term and an interference term. For double scattering the scattering amplitude is given by the square of the quantity  $A^*A$ . It can be seen that the the first order correction term is larger in comparison, and the mixing is even stronger for higher order scattering. Therefore the contribution to single scattering intensity from the off-resonant level and the correction terms due to multiple scattering give rise to detuning dependance observed. It should be noted that that there are higher order contribution on-resonance also, but these have a smaller cross term. At small detunings the contributions from higher orders diminish, but has larger cross terms.

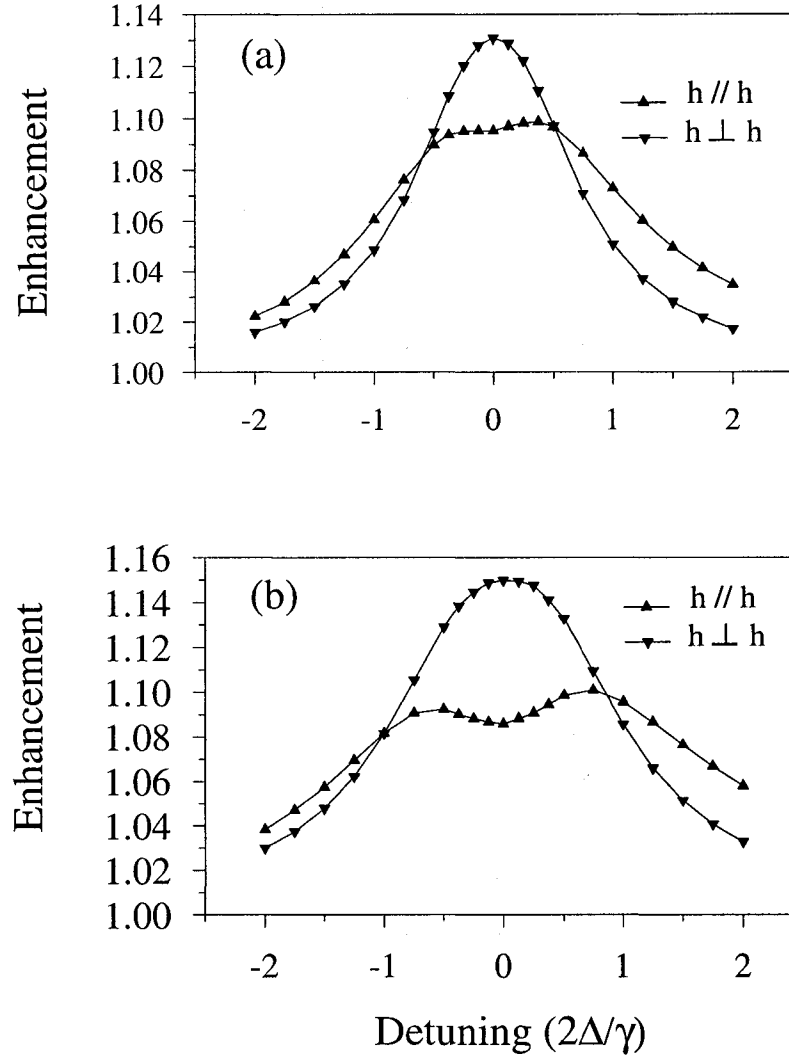


FIG. 38. The calculated spectral dependence of the enhancement factor in the circular channels for the  $F = 3 \rightarrow F' = 4$  hyperfine transition, in  $^{85}\text{Rb}$ . Gaussian type atomic cloud, (a) radius  $r_0 = 1 \text{ mm}$ , density  $n_0 = 8 \cdot 10^9 \text{ cm}^{-3}$  and (b) radius  $r_0 = 1 \text{ mm}$ , density  $n_0 = 16 \cdot 10^9 \text{ cm}^{-3}$  [1].



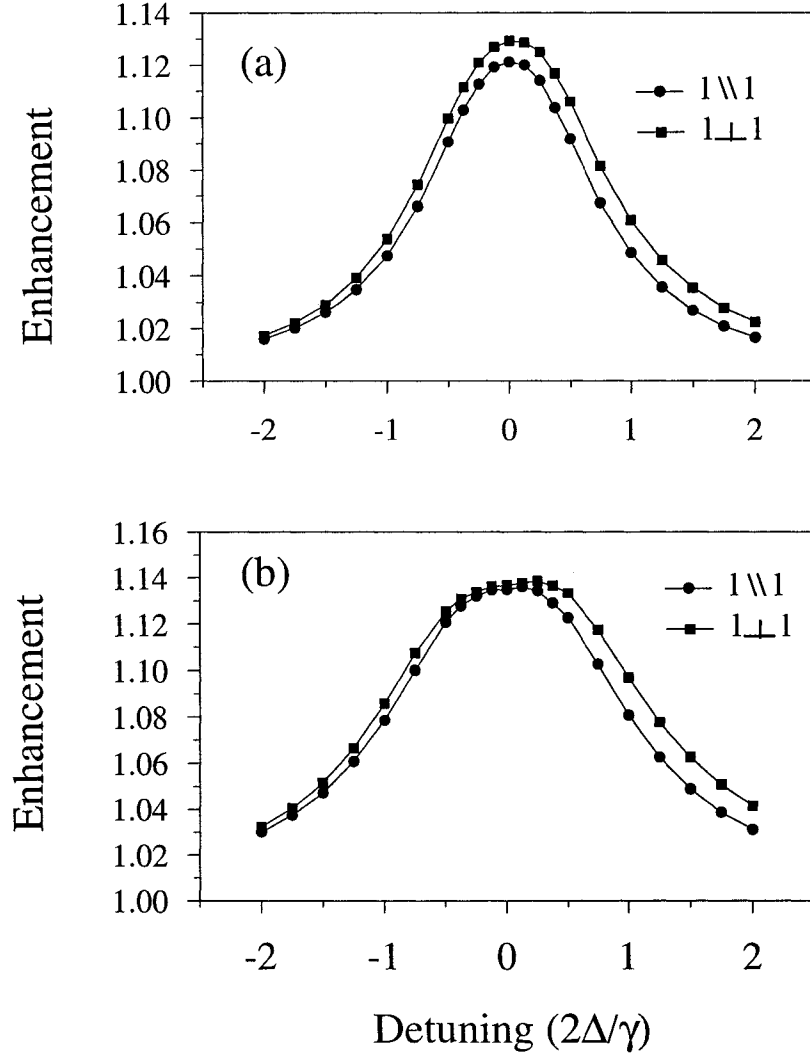


FIG. 39. The calculated spectral dependence of the enhancement factor in the linear channels for the  $F = 3 \rightarrow F' = 4$  hyperfine transition, in  $^{85}\text{Rb}$ . Gaussian type atomic cloud, (a) radius  $r_0 = 1 \text{ mm}$ , density  $n_0 = 8 \cdot 10^9 \text{ cm}^{-3}$  and (b) radius  $r_0 = 1 \text{ mm}$ , density  $n_0 = 16 \cdot 10^9 \text{ cm}^{-3}$  [1].

## CHAPTER 5

### CONCLUSIONS

The measurement of polarization and spectral dependance of the coherent backscattering signal were made for ultracold  $^{85}\text{Rb}$ . These measurements were compared with theoretically calculated values and was found to be in good agreement. It is clearly seen that the internal structure of the atom- its quantum mechanical properties contribute to the observables, and significantly modify the coherent backscattering signal expected from a pure classical stand point.

The experimental data on the enhancement and the width of the backscattering profile of ultra cold  $^{85}\text{Rb}$  is in good qualitative agreement with theoretical results. In addition it was found that while the enhancement does not depend on the sample size, for a given optical depth the width of the profile to be inversely proportional to the sample size. Finally conclusive evidence of a strong sub-natural width spectral dependance is observed in the coherent backscattering signal, for light tuned around the  $F = 3 \rightarrow F' = 4$  transition in the  $h||h$  polarization channel. This effect although clearly evident in the Raman-type helicity preserving channel is also expected to be present in other polarization channels. The effect is attributed to interference with far off-resonant hyperfine transitions. In this case the off-resonant level is the  $F = 3 \rightarrow F' = 3$  transition at 120.7 MHz to the red of the cycling transition  $F = 3 \rightarrow F' = 4$ .

Future work in this area will necessarily have to concentrate on improving the signal/noise in the experiment, to quantify the effect in other polarization channels, and in the above mentioned probe frequencies. This would necessarily involve constructing ultra stable lasers, both in frequency and intensity, and better MOT loading techniques to reduce background fluorescence. The coherent backscattering of light at from other hyperfine levels needs to be investigated. Observation of coherent backscattering of a probe tuned to other available levels in the  $^{85}\text{Rb}$  D2 line possibly show a larger interference effect due to the proximity of these levels. The separation of  $F = 2 \rightarrow F' = 1, 2, 3$  is approximatley 90 MHz as compared to the the splitting between the cycling transition and the  $F = 3 \rightarrow F' = 4, 3, 2$  splitting of 180 MHz. A natural extension of this work is to investigate the coherent backscattering signal from an ultracold sample of  $^{87}\text{Rb}$ . The existing set up can easily be adopted for this experiment with only minor modifications of the lasers. It remains to be examined if

the larger hyperfine separation in the ground level, 6.8 GHz as compared 3.02 GHz in  $^{85}\text{Rb}$  would contribute to a enhancement factors different from that observed for  $^{85}\text{Rb}$ .

The measurements made of the coherent backscattering signal from ultra cold  $^{85}\text{Rb}$  atoms show that the width of the backscattered signal profile is dependent on the size of the sample. The ability to observe a coherent backscattering signal from a small but dense collection of atoms can lead to better understanding of light “localization,” as in this limit the mean free path of the photon converges to its wavelength. It should be noted that in this work the densities were far from this region. At higher densities atom-atom interactions too will become an important factor in determining the nature of the coherent backscattering signal. It is, though, not too difficult to modify this apparatus to achieve higher atomic densities in a smaller trap volume. This can be achieved by means of a spatial or a temporal dark trap, both having higher densities and the former a far smaller volume. Although these techniques will not reach the critical density necessary to reduce the mean free path to a photon wavelength, the trend in cone width to sample size relation can be further explored. It should be noted that atom-atom interactions will become important as the density of the scatterers are increased.

Apart from improving on the above two measurements there are several novel areas to be explored. First the dependence of the coherent backscattering cone on the input laser power. At the moment this experiment is being carried out with the addition of a slave laser on the probe. At saturation it is not obvious how reciprocity will be effected. Also at high power the effects of light intensity, such as changes in elastic, inelastic scattering cross section, Mollow triplets and superposition of atom-field states will become a factor in determining the backscattered profile. Again this will require a bigger, more robust trap.

The backscattering signal by itself can be used as a probe of the collective structure and dynamics of a magneto-optic trap. Here it was shown conclusively that the size parameter of the trap can be easily obtained from the width of the backscattering profile. It is also possible to probe magnetic effects due to external or optical pumping of the trapped atoms by analysis of the CBS profile and its spectral dependence. Changes of in coherent backscattering profile due to induced static magnetic fields has been observed (in experiments by R. Kaiser et al) [64]. Theoretical work is already in progress looking at these effects.

The major effort at realizing localization today is concentrated in photonic band-gap materials, where the scattering is not entirely random. It is however now possible to arrange highly resonant scatterers, namely atoms in either one, two or three dimensional optical lattices in free space. From such lattices Bragg like scattering has been recently observed. While the dynamics of atoms in magneto-optical traps are complex, these lattices might provide a more controlled collection of scatterers to observe coherent backscattering.

The extension of theoretical work in this field along with further advances in these experiments inevitably will lead to better understanding of multiple light scattering in the limits so far not considered, and possibly lead to observation of localization of photons.

## APPENDIX A

### THE ANGULAR INTEGRATION OF THE ARRAY

The angular integration program is implemented and coded in C. This code consist of three sections, *integration.c*, *array.c* and *readfile.c*. The *readfile.c* expects the data format x,y,z where (x, y) is the pixel and z is the intensity at (x,y) an integer from -64556 to +64556 [65]. The code as it was implemented is included below for reference.

#### A.1 INTEGRATION.C

```
#define NDEBUG

#include <stdlib.h> #include <stdio.h> #include <math.h>

#include "array.h" #include "read_file.h"

#define Pi 3.1415926535897932385

#ifndef NDEBUG #define dfprintf(s) fprintf s #else #define
dfprintf(s) #endif

void integrate(struct array *array_p, double x0, double y0, double
r_max, int np, int ni){
    double f;
    double r, th, x, y;
    int i, j;
    for(i=0; i<np; i++){
        r=-r_max+2*r_max*i/(np-1);
        f=0;
        for(j=0; j<ni; j++){
            th=2*Pi*j/ni;
            x=x0+r*cos(th);
```

```

        y=y0+r*sin(th);
        f+=array_val(array_p,x,y);
    }
    f*=2*Pi/ni;
    printf("%f %f\n",r,f);
}
}

#define N_PLOT_POINTS 100 #define N_INTEGRATION_POINTS 360

int main(int argc,char **argv){

    struct array *array_p;
    double x0,y0;
    double x,y;
    double rXmax,rYmax,rmax;

    /* check argument sanity */

    if(argc!=4){
        fprintf(stderr,"usage %s filename x0 y0\n",argv[0]);
        exit(EXIT_FAILURE);
    }

    /* read the data file */

    array_p=read_file(argv[1]);
    if(array_p==NULL){
        fprintf(stderr,"couldn't read file\n");
        exit(EXIT_FAILURE);
    }

    /* get center from command line */

```

```

x0=strtod(argv[2],NULL);
y0=strtod(argv[3],NULL);

/* Print data arround the center */

fprintf(stderr,"Values arround %f %f\n",x0,y0);
for(x=x0-array_p->x_bin_size;x<x0+1.5*array_p->x_bin_size;
    x+=array_p->x_bin_size){
    for(y=y0-array_p->y_bin_size;y<y0+1.5*array_p->y_bin_size;
        y+=array_p->y_bin_size){
        fprintf(stderr,"%f    ",array_val(array_p,x,y));
    }
    fprintf(stderr,"\n");
}

/* calculate the maximum radius so as not to exceed*/
/* the bounds of the array */

rXmax=(array_p->x_max-x0 < x0-array_p->x_min) ?
array_p->x_max-x0 : x0-array_p->x_min;
rYmax=(array_p->y_max-y0 < y0-array_p->y_min) ?
array_p->y_max-y0 : y0-array_p->y_min;
rmax=(rXmax < rYmax) ?
rXmax-array_p->x_bin_size : rYmax-array_p->y_bin_size;

/* make integration */

integrate(array_p,x0,y0,rmax,N_PLOT_POINTS,N_INTEGRATION_POINTS);

return 0;
}

```

## A.2 ARRAY.C

```

#include <stdlib.h> #include <stdio.h> #include <math.h>

#include "array.h"

double rint(double);

struct array *array_create(
    double x_min,
    double x_max,
    double y_min,
    double y_max,
    int n_rows,
    int n_cols
){
    struct array *array_p;

    int row;

    /* allocate memory to hold the information on the array */

    if((array_p=malloc(sizeof *array_p))==NULL){
        /* an error occurred trying to malloc */
        return NULL;
    }

    /* allocate an array of rows */

    if((array_p->data=malloc(n_rows*sizeof *array_p->data))==NULL){
        /* an error occurred trying to malloc */
        free(array_p);
        return NULL;
    }

    /* allocate the rows */

```



```

for(row=0;row<n_rows;row++){
    if((array_p->data[row]
    =malloc(n_cols*sizeof *array_p->data[row]))==NULL){
        /* an error ocured trying to malloc */
        while((--row)!=-1){
            free(array_p->data[row]);
        }
        free(array_p->data);
        free(array_p);
        return NULL;
    }
}

/* store the initial array parameters */

array_p->n_rows=n_rows;
array_p->n_cols=n_cols;

array_p->x_min=x_min;
array_p->x_max=x_max;
array_p->y_min=y_min;
array_p->y_max=y_max;

array_p->x_bin_size=(x_max-x_min)/(n_cols-1);
array_p->y_bin_size=(y_max-y_min)/(n_rows-1);

return array_p;
}

void array_destroy(struct array *array_p){
    int row;
    for(row=0;row<array_p->n_rows;row++){
        free(array_p->data[row]);
    }
}

```

```

    }
    free(array_p->data);
    free(array_p);
}

double array_val(struct array *array_p, double x, double y){

    int row,col;
    double a,b,c;
    double d,e,f;
    double g,h,i;
    double C,Cx,Cy,Cxx,Cyy,Cxy,Cxxy,Cxyy,Cxxyy;

    /* Calculate which row,column this point falls into */

    col=rint((x-array_p->x_min)/array_p->x_bin_size);
    row=rint((y-array_p->y_min)/array_p->y_bin_size);

    /* Make sure the point isn't out of the range */

    if(row<1 || row>array_p->n_rows-2 || col<1 ||
    col>array_p->n_cols-2){
        fprintf(stderr,"Out of range %f,%f\n",x,y);
        exit(0);
    }

    /* Get the cells arround arround row, col */

    a=array_p->data[row-1][col-1]; b=array_p->data[row-1][col];
    c=array_p->data[row-1][col+1];
    d=array_p->data[row ][col-1]; e=array_p->data[row ][col];
    f=array_p->data[row ][col+1];
    g=array_p->data[row+1][col-1]; h=array_p->data[row+1][col];
    i=array_p->data[row+1][col+1];

```

```

/* Shift the coordinates so that 0,*/
/*0 is the center of the row,column */

x-=array_p->x_min+col*array_p->x_bin_size;
y-=array_p->y_min+row*array_p->y_bin_size;

/* Calculate the interpolation coefficients using
code gotten from mathematica using the following input

$$F[x_,y_]=C + Cx*x + Cy*y + Cxx*x*x + Cyy*y*y + Cxy*x*y$$


$$+ Cxxy*x*x*y + Cxyy*x*y*y + Cxxyy*x*x*y*y$$

s=Solve[{
    a==F[-xs,-ys],b==F[ 0,-ys],c==F[+xs,-ys],
    d==F[-xs, 0],e==F[ 0, 0],f==F[+xs, 0],
    g==F[-xs,+ys],h==F[ 0,+ys],i==F[+xs,+ys]
},{C,Cx,Cy,Cxx,Cyy,Cxy,Cxxy,Cxyy,Cxxyy}]
*/

C=e;
Cx=(f-d)/(2*array_p->x_bin_size);
Cy=(h-b)/(2*array_p->y_bin_size);
Cxx=(d+f-2*e)/(2*array_p->x_bin_size*array_p->x_bin_size);
Cyy=(b+h-2*e)/(2*array_p->y_bin_size*array_p->y_bin_size);
Cxy=(a+i-c-g)/(4*array_p->x_bin_size*array_p->y_bin_size);
Cxxy=(2*b-a-c-2*h+g+i)/(4*array_p->x_bin_size*array_p->
x_bin_size*array_p->y_bin_size);
Cxyy=(2*d-a-g-2*f+c+i)/(4*array_p->x_bin_size*array_p->
y_bin_size*array_p->y_bin_size);
Cxxyy=(a+c+g+i-2*b-2*d-2*f-2*h+4*e)/(4*array_p->x_bin_size*array_p->
x_bin_size*array_p->y_bin_size*array_p->y_bin_size);

/* 0-> do interpolate, 1->do NOT interpolate */
#if 0
Cx=Cy=Cxx=Cyy=Cxy=Cxxy=Cxyy=Cxxyy=0;

```

```

#endif

return C + Cx*x + Cy*y + Cxx*x*x + Cyy*y*y + Cxy*x*y +
Cxyy*x*x*y + Cxyy*x*y*y + Cxxyy*x*x*y*y;
}

void array_init(struct array *array_p,double (*f)(double x,double
y)){
    int row,col;
    for(row=0;row<array_p->n_rows;row++){
        for(col=0;col<array_p->n_cols;col++){
            array_p->data[row][col]=f(array_p->x_min+array_p->
x_bin_size*col,array_p->y_min+array_p->y_bin_size*row);
        }
    }
}

```

### A.3 READFILE.C

```

#include <stdio.h> #include <stdlib.h> #include <limits.h>

#include "array.h"

/*
 * Reads one of pasads data
 */

struct array *read_file(char *file_name){

    FILE *file;
    char line[1000];
    int x,y;
    double n;
    int xmin,xmax,ymin,ymax;

```

```

struct array *array_p;

/* Open the file */

file=fopen(file_name,"r");
if(file==NULL){
    fprintf(stderr,"Couldn't open file\n");
    exit(EXIT_FAILURE);
}

/* Read the file to find out the dimension of the array */

xmin=INT_MAX;
xmax=INT_MIN;
ymin=INT_MAX;
ymax=INT_MIN;
while(fgets(line,sizeof line,file)!=NULL){
    if(sscanf(line,"%d%*[ ,\t]%d%*[ ,\t]%lf",&x,&y,&n)!=3){
        fprintf(stderr,"couldn't parse line A: %s\n",line);
        exit(EXIT_FAILURE);
    }
    xmin=(xmin < x) ? xmin : x;
    xmax=(xmax > x) ? xmax : x;
    ymin=(ymin < y) ? ymin : y;
    ymax=(ymax > y) ? ymax : y;
}

/* Allocate the array */

array_p=array_create(xmin,xmax,ymin,ymax,xmax-xmin+1,ymax-ymin+1);

/* Reread the file and init the array */

rewind(file);

```

```
while(fgets(line,sizeof line,file)!=NULL){
    if(sscanf(line,"%d%*[ ,\t]%d%*[ ,\t]%lf",&x,&y,&n)!=3){
        fprintf(stderr,"couldn't parse line B: %s\n",line);
        exit(EXIT_FAILURE);
    }else{
        array_p->data[y-ymin][x-xmin]=n;
    }
}

return array_p;

}
```

## BIBLIOGRAPHY

- [1] D. V. Kupriyanov, I. M. Sokolov, P. Kulatunga, C.I. Sukenik and M. D. Havey, Phys. Rev. A 67, 013814 (2003).
- [2] E. Akkerman, P. E. Wolf, and R. Maynard, Phys. Rev. Lett. 57, 1471 (1986).
- [3] J. L. Lagner and T. Neal Phys. Rev. Lett. 16, 984 (1966).
- [4] D. A. de Wolf, IEEE Trans., Antennas Propag. 19, 254 (1971).
- [5] Y. Kuga, A. Ishuimaru, J. opt. Soc. Am. A 8, 831 (1984).
- [6] M. van Albada, A. Lagendijk, Phys. Rev. Lett. 55, 2692 (1985).
- [7] P. E. Wolf and G. Maret, , Phys. Rev. Lett. 55, 2696 (1985).
- [8] Ping Sheng, *Introduction to Wave Scattering, Localization, and Mesoscopic Phenomena*, (Academic Press, San Diego, 1995).
- [9] P. Sheng (ed.) *Scattering and Localization of Classical waves in Random Media*, (World Scientific, Singapore, 1990).
- [10] D. Wiersma, M. van Albada, B. van Tiggelen, A. Lagendijk, Phys. Rev. Lett. 58, 945 (1987).
- [11] P. W. Anderson, Phys. Rev. 109, 1492 (1958).
- [12] G. Bergmann, Phys. Rev. B 28, 2914 (1983).
- [13] S. John, Phys. Rev. Lett. 53, 2169 (1984).
- [14] S. John, Phys. Rev. Lett. 58, 2486 (1987).
- [15] D. S. Wiersma, P. Bartolini, Ad. Lagendijk, R. Righini, Nature 390, 671 (1997).
- [16] A. A. Chabanov, M. Stoytchev, A. Z. Genack, Nature 404, 850 (2000).
- [17] E. L. Rabb, M. Prentiss, A. Cable, S. Chu, and D. Pritchard, Phys. Rev. Lett. 59, 2631 (1987).
- [18] S. Chu, L. Hollberg, J. Bjorkholm, A. Cable, and A. Ashkin, Phys. Rev. Lett. 55, 48 (1985).

- [19] S. Chu, C. Wieman, J. Opt. Soc. Am. B 2, 1705 (1985).
- [20] C. Cohen-Tannoudji, Phys. Rep. 219, 153 (1992).
- [21] W. D. Phillips, Prog. Quant. Elect. 8, 115 (1984).
- [22] Th. M. Nieuwenhuizen, A. L. Burin, Yu. Kagan, G. V. Shlyapnikov, Phys. Lett. A 184, 360 (1994).
- [23] G. Labeyrie, F. de Thomasi, J.-C. Bernard, C.A. Muller, C. Miniatura, and R. Kaiser, Phys. Rev. Lett. 83, 5266 (1999).
- [24] G. Labeyrie, C. A. Muller, D. S. Wiersma, Ch. Miniatura, R. Kaiser, J. Opt. B: Quantum and Semiclass. Opt. 2, 672 (2000).
- [25] P. Kulatunga, C. I. Sukenik, S. Balik, M. D. Havey, D. V. Kupriyanov, I. M. Sokolove, Submitted for publication (2002).
- [26] G. Labeyrie, C. Miniatura, C. A. Muller, O. Sigwarth, D. Delande, and R. Kaiser, Phys. Rev. Lett. 89, 163901 (2002)
- [27] B. A. van Tiggelen, Ad Lagendijk, *New Aspects of Electromagnetic and Acoustic Wave Diffusion*, POAN Research Group (Ed.), Springer-Verlag (Berlin, 1998).
- [28] Cord A. Muller, Thibaut Jonckheere, Christian Miniatura, Dominique Delande, Phys. Rev. A 64, 053804 (2001).
- [29] Martin B. van der Mark, Meint P. van Albada, and Ad Lagendijk, Phys. Rev. B, 37, 3575, 26 (1988).
- [30] A. A. Glloubentsev, Sov. Phys. JETP 59(1), (1994).
- [31] M. I. Mishchenko, Jean-Marc Luck, T. M. Nieuwenhuizen, J. Opt. Soc. Am. 17, 888 (2000).
- [32] J. H. Xhu, D. J. Pine, D. A. Weitz, Phys. Rev. A 44, 3948 (1990).
- [33] Lagendijk A. and van Tiggelen B. A. Phys. Rep. 270, 167 (1996).
- [34] M. C. W. van Rossum, Th. M. Nieuwenhuizen, Rev. Mod. Phys. 71, 313 (1999).
- [35] M. I. Mishchenko, J. Quant. Spect. Radi. Transf. 56, 673 (1996).



- [36] J. D. Jackson, *Classical Electrodynamics*, 2nd ed. (John Willey & Sons, 1975).
- [37] S. Feng, C. Kane, A. D. Stone, Phys. Rev. Lett. 61, 834(1988).
- [38] R. Kaiser, C. Westbrook, F. David, (Eds.), *Coherent atomic matter waves - Ondes de matiere coherentes*, (Springer-Verlag Heidelberg 1999).
- [39] A. F. Molisch and B. P. Oehry, *Radiation Trapping in Atomic Vapors*, Clarendon Press (Oxford, 1998).
- [40] Harold J. Metcalf, Peter van der Straten, *Laser Cooling and Trapping*, (Springer-Verlag, New York, 1999).
- [41] M. Sargent III, M. O. Scully, A. E. Lamb Jr., *Laser Physics*, (Addison=Wesley Massachusetts, 1974).
- [42] M. Weissbluth, *Photon-Atom Interaction*, (Academic Press, New York, 1989).
- [43] R. Loudon, *The Quantum Theory of light*, 3rd ed., (Oxford University Press, Oxford, 2000).
- [44] Michael I. Mishchenko, Opt. Lett. 21, 623 (1996).
- [45] C. H. Green, R. N. Zaire, Ann. REv. Phys. Chem. 33, 119 (1982).
- [46] Michael I. Mishchenko, J. Opt. Soc. Am. A 9, 978 (1992).
- [47] A.S. Martinez, R. Maynard, Phys. Rev. B 50, 3714 (1994).
- [48] D. S. Wiersma, M. P. van Albada, B. A. van Tiggelen, A. Lagendijk, Phys. Rev. Lett. 74, 4193 (1995).
- [49] J.L. Hall, M. S. Taubman, J. Ye, *OSA Handbook v 12A*, (1999).
- [50] W. Demtroder, *Laser Spectroscopy*, (Springer-Verlag, New York, 1981).
- [51] D. W. Preston, Am. J. Phys. 64, 1432 (1996).
- [52] M. G. Littman, H. J. Metcalf, Appl. Opt. 17, 2224 (1978).
- [53] L. Ricci, M. Weidemüller, T. Esslinger A. Hemmerich, C. Zimmermann, V. Vuletic, W. König, T. W. Hänsch, Opts. Comm. 117, 541 (1995).

- [54] K. G. Libbrecht, J. L. Hall, *Rev. Sci. Instrum.* 64(8) 2133 (1993).
- [55] K. D. MacAdam, A. Steinbach, C. Wieman, *Am. J. Phys.* 60, 1098 (1992).
- [56] M. V. R. K. Murty, *Appl. Opt.* 3, 531 (1964).
- [57] Carl Wiemann, Gwen Flowers, Sara Gilbert, *Am. J. Phys.* 63,317 (1995).
- [58] Soichi Kobayashi, Tatsuya Kimura, *J. Quan. Elect.* 17, 681 (1981).
- [59] G. Ferrari, M. O. Mewes, F. Schreck, C. Salomon, *Opt. Lett.* 24, 151 (1999).
- [60] P. Feng, T. Walker, *Am. J. Phys.* 63, 905 (1995).
- [61] R. Kowalski, S. Root, S. D. Gensemer, P. L. Gould, *Rev. Scien. Instr.* 72, 2532 (2001).
- [62] Y. Bidel, B. Klappauf, J. C. Bernard, D. Delande, G. Labeyrie, C. Miniatura, D. Wilkowski, R. Kaiser, *Phys. Rev. Lett.* 88, 203902-1 (2002).
- [63] C. A. Müller, T. Jonckheere, C. Miniatura, D. Delande, *Phys. Rev. A* 64, 053804 (2001).
- [64] G. Labeyrie, C. Miniatura, R. Kaiser, *Phys. Rev. A* 64, 033402 (2001).
- [65] Tobias Oed, private communication.

## VITA

Pasad B. Kulatunga  
 Department of Physics  
 Old Dominion University  
 Norfolk, VA 23529

Date/Place of Birth: July 04th 1966, Colombo, Sri Lanka Nationality: Sri Lankan

Education: B.Sc. University of Wisconsin at Whitewater May 1992. M.Sc. Central Michigan University, August 1994. M.Sc. Old Dominion University, December 1996.

Work Experience: Post-Doctoral Research Associate, University of Wisconsin - Madison. Graduate Research Assistant, Old Dominion University. Research Internship, New Focus, Inc., Madison Wisconsin. Graduate Teaching Assistant, Old Dominion University. Graduate Research Assistant, Central Michigan University

### Publications:

"Coherent Backscattering of light in atomic systems: Application to weak localization in an ensemble of cold alkali-metal atoms," D. V. Kupriyanov, I. M. Sokolov, P. Kulatunga, C.I. Sukenik and M.D. Havey, Phys. Rev. A 67, 013814 (2003).

"Reflection high-energy electron diffraction study of melting and solidification of Pb on graphite," Z. H. Zhang, P. Kulatunga, and H. E. Elsayed-Ali, Phys: Rev: B, Vol: 56, 4141 (1997).

"Hyperfine Structure Measurements in the  $4p^2P_{3/2}$  State of  $^{41}\text{K}$  Using Polarization Quantum Beat Spectroscopy," A. Sieradzan, P. Kulatunga, and M. Havey, Phys: Rev: A, Vol: 52, 4447-4450 (1995).

### Conference Proceedings and Abstracts:

"Weak localization of light in ultracold atomic Rb," P. Kulatunga, C.I. Sukenik, and M.D. Havey, D.V. Kupriyanov and I. M. Sokolov. 2002 OSA Annual Meeting, Orlando FL, September 2002.

"Multiple Coherent Light Scattering in Ultra-cold Rubidium," M. D. Havey, C. I. Sukenik, P. Kulatunga, D.V. Kupriyanov and I. M. Sokolov. DAMOP02 meeting of the American Physical Society, Williamsburg VA, May 2002.

"Multiple Coherent Light Scattering in Ultracold Rubidium," M. D. Havey, C. I. Sukenik, P. Kulatunga, D.V. Kupriyanov and I. M. Sokolov. DAMOP02 meeting of the American Physical Society, London, ON, 2001.